

THESIS TITLE

**SOFT ROBOTIC GRIPPERS
USING GECKO-INSPIRED FIBRILLAR ADHESIVES
FOR THREE-DIMENSIONAL SURFACE GRASPING**

*Submitted in partial fulfillment of the requirements for
the degree of Doctor of Philosophy in*

Department of Mechanical Engineering

Presented by

Sukho Song

05. 19. 2017

M.S., in Nanomechanics, Tohoku University, Sendai, Miyagi, Japan

B.S., Aeronautics and Space Engineering, Tohoku University, Sendai, Miyagi, Japan

Carnegie Mellon University

Pittsburgh, PA, United States

Abstract

Researches on biological adhesive systems in nature have changed a perspective view on adhesion that it is not only the area of surface chemistry, but also mechanics of interfacial geometry which can significantly effect on fracture strength and load distribution on the contact interface. Various synthetic fibrillar adhesives in previous works have shown enhanced interfacial bond strength with the capacity of adhesion control by exploiting mechanical deformation of the elastomeric fibrillar structures inspired by geckos. However, control of the interfacial load distribution has been focused on the size of micro-contact with single or a few of micro-/nano-fibers on planar surface, and not for a large contact area on complex three-dimensional (3D) surfaces.

This thesis work aims at investigating principles of the interfacial load distribution control in multi-scale, ranging from micro-contact with single micro-fiber to a centimeter-scale contact with a membrane-backed micro-fiber array on non-planar 3D surfaces. The findings are also applied for developing a soft robotic gripper capable of grasping a wide range of complex objects in size, shape, and number, expanding the area of practical applications for bio-inspired adhesives in transfer printing, robotic manipulators, and mobile robots.

This paper comprises three main works. First, we investigate the effect of tip-shapes on the interfacial load sharing of mushroom-shaped micro-fibrillar adhesives with precisely defined tip-geometries using high resolution 3D nano-fabrication technique. For a large area of non-planar contact interface, we fabricate fibrillar adhesives on a membrane (FAM) by integrating micro-fibers with a soft backing, which enables robust and controllable adhesion on 3D surfaces. Picking and releasing mechanism for the maximal controllability in adhesion are discussed. Finally, we propose a soft robotic architecture which can control the interfacial load distribution for the FAM on 3D surfaces, solving an inherit dilemma between conformability and high fracture strength with the equal load sharing on complex non-planar 3D surfaces.

KEYWORDS: gecko-inspired micro-fibrillar adhesives, fracture mechanics, equal load sharing, controllable adhesion, complex 3D surfaces, soft robotics, gripper, pick-and-place manipulation

Acknowledgments

This thesis would have not been possible without the dedicated help and support from my advisor Dr. Metin Sitti, who has given me a chance to jump into this new field of soft robotics, and believed my potential throughout the entire Ph.D. program. I would especially thank Dr. Carmel Majidi who has advised me through our collaborations, as if I am the one of his Ph.D. students. I would also thank all the members of the NanoRobotics Group at Carnegie Mellon University as well as the Physical Intelligence Department at Max Planck Institute for Intelligent Systems in Stuttgart, Germany. They were my friends, collaborators, teachers, and counselors during my Ph.D. program.

To my dear family, I would have not been able to come to this far without your love and sacrifices. For the past five years, what you have dreamed was my dream, and what I have achieved became your achievements. I am always proud of being your son and your brother.

Finally, I thank God who has envisioned my life through His Words to become a researcher who can please Him, saying *"Then God said, "Let us make man in our image, in our likeness, and let them rule over all the creatures that move along the ground. So God created man in his own image, in the image of God he created him. God saw all that he had made, and it was very good. And there was evening, and there was morning—the sixth day. (Genesis 1:26-31)"*.

A part of this thesis work is funded by the National Science Foundation CMMI-1130520 grant, as well as from the Office of Naval Research (Bio-Inspired Autonomous Systems; Dr. Tom McKenna; Award N000141612301).

Contents

Abstract	iii
Acknowledgments	v
List of Tables	viii
List of Figures	xxi
1 Introduction	1
1.1 Motivation	1
1.2 Interfacial load sharing on micro-contact depending on different tip-geometries	3
1.3 A soft robotic gripper with controllable adhesion of micro-fibrillar adhesives on 3D surfaces	5
1.4 Interfacial load distribution control for a soft adhesive membrane on 3D surfaces	10
1.5 Research Objectives	12
1.6 Thesis Outline	13
1.7 Publications	13
2 Shape Optimization of Micro-fibers for Equal Load Sharing	15
2.1 Introduction	15
2.2 Experiments	15
2.3 Results and Discussion	18

2.4	Summary	23
3	Fibrillar Adhesives on a Membrane for Large-scale 3D Surface Grasping	25
3.1	Introduction	25
3.2	Experimental Methods	27
3.3	Picking and releasing mechanisms	28
3.4	Characterization of the FAM	32
3.5	Theoretical Analysis on adhesion of the FAM	40
3.6	Demonstrations of Pick-and-release Manipulation	54
3.7	Summary	56
4	Load Distribution Control of a Soft-backed Micro-fiber Array on Complex 3D Surfaces	61
4.1	Introduction	61
4.2	Structure and Basic Mechanism of the Soft Adhesion System	62
4.3	Fabrication	65
4.4	Modeling the Effect of Pressure Differential on Adhesion	70
4.5	Characterizations	78
4.6	Discussion	86
4.7	Summary	88
5	Conclusions and Outlook	97
5.1	Contributions	98
5.2	Future Works	102
	References	116

List of Tables

3.1	Design Parameters of the FAM	47
4.1	$F_{\text{off} _{\text{sf}}}$, $A_{\text{rc} _{\text{sf}}}$, $\sigma_{\text{ad} _{\text{sf}}}$ and $\sigma_{\text{ad} _{3f}}$ of micro-fiber array	80
4.2	Summary of F_{off} , ω_{ad} and σ_{ad} of the FAM for the rigid adhesion system . . .	81
4.3	Summary of F_{off} , ω_{ad} and σ_{ad} of the FAM for the soft adhesion system . . .	82
4.4	Characterization results of the rigid adhesion system	86
4.5	Characterization results of the soft adhesion system	87

List of Figures

1.1	An overview of geckos' hierarchical fibrillar foot-hairs from macro-scale to nano-scale: (a) A Tokay gecko's foot on a flat glass, (b) a scanning electron microscopy (SEM) image of geckos' setae from side, and (c) the top, (d) a SEM image of tips of geckos' setae, and (e) a SEM image of numerous spatulae. ST: Seta, BR: Branch, and SP: Spatula	2
1.2	Previous works on gecko-inspired synthetic micro-fibrillar adhesives and equal load sharing system, ranging from micro-scale to marco-scale: (a) gecko-inspired slanted micro-wedges for enhanced friction (i-iii), and mushroom-shaped micro-fibers for the maximal adhesion with equal load sharing on micro-contact (iv-vi). (b) Design of synthetic load sharing system for friction on flat surface, capable of distributing the applied load to the load tendon and adhesive tiles evenly (top). Still frames of a 70 kg climber ascending a vertical glass wall using the device (bottom).	4
1.3	State of the art in soft robotics: (a) A pneumatically driven gaiting robot made out of soft deformable elastomer, (b) a peristaltically crawling soft robot driven by SMA actuators, (c) a sphere-shaped rolling robot based on jamming, (d) a soft manipulator wrapping around a human's hand (i) and its cross-section inspired by the muscle structure of octopus arm (ii), (e) a soft-bodied caterpillar robot (i) and its ballistic rolling locomotion (ii), and (f) a wall climbing robot (i) using gecko-inspired elastomeric micro-wedge structures (ii).	6

1.4	Soft robotic manipulators: (a) A starfish-shaped soft gripper catching a paralyzed mouse (i:approaching, ii:gripping), (b) a universal gripper pouring a glass of water, (c) a trunk-shaped soft manipulator wrapping around a cup (i:approaching, ii:wrapping), and (d) a soft gripper having pouches filled with magnetorheological fluids to mold objects' shape.	8
1.5	Schematics of picking up a non-planar 3D part: (a) A fibrillar adhesives on a rigid backing layer and (b) a soft gripper using the fibrillar adhesives on a soft membrane backing.	10
2.1	(a) Schematic of a mushroom-like elastomeric micro-fiber. (b) Scanning electron microscope (SEM) image of a 3D-printed micro-fiber. The inset shows cross-sectional SEM image of the micro-fiber tip edge, which is slightly rounded. (c) Fabrication process steps for the micro-fibers: 3D-printing the master fiber from a UV-curable photoresist using two-photon lithography, developing it, creating its negative silicone rubber mold, and molding the negative mold with polyurethane elastomers to create positive fibers. Copyright © 2015 American Chemical Society.	17
2.2	(a) Schematics of the custom automated adhesion characterization setup. A spherical glass indenter is attached to a load cell for vertical force measurement. The load cell is connected to a motorized XYZ-stage for motion control. An inverted microscope is used to observe the interaction between fiber tips and the spherical indenter. (b) Different steps of the adhesion test shown on a sample force-displacement data plot: A) The indenter approaches the fiber tip; B) The indenter makes contact with fiber tip and remains in contact for 30 seconds; C) The indenter starts the retraction process; D) The maximum reaction force is measured; E) Full tip detachment occurs. Copyright © 2015 American Chemical Society.	18

- 2.3 Reactive force F_{re} as a function of displacement z for ST-1060 polyurethane fibers at (a) $\beta = 1.1$ and $\theta = 30^\circ - 60^\circ$ and (b) $\theta = 45^\circ$ and $\beta = 1.1 - 1.5$. Snapshots of crack propagation in ST-1060 fibers at (c) $\theta = 45^\circ$ and $\beta = 1.3$ (optimal) and (d) $\theta = 60^\circ$ and $\beta = 1.2$ (non-optimal). Scale bars on (c) and (d) correspond to $100 \mu\text{m}$. The first images on both (c) and (d) show the crack initiation and the last images on these parts correspond to full detachment. The entire crack propagation process takes around 400 msec for the optimal set of parameters while it takes around 13.47 sec for the non-optimal case. (e) Experimental pull-off force F_{off} results at different β and θ values. Each data point is an average of six measurements and the error bar indicates the standard deviation. Copyright © 2015 American Chemical Society. 21
- 2.4 Reactive force F_{re} as a function of displacement z for harder ST-1087 polyurethane fibers at (a) $\beta = 1.1$ and $\theta = 30^\circ - 60^\circ$ and (b) $\theta = 45^\circ$ and $\beta = 1.1 - 1.5$. Snapshots of crack propagation in ST-1087 fibers at (c) $\theta = 30^\circ$ and $\beta = 1.2$ (optimal) and (d) $\theta = 45^\circ$ and $\beta = 1.3$ (non-optimal). Scale bars on (c) and (d) correspond to $100 \mu\text{m}$. The first images on both (c) and (d) show the crack initiation and the last images on these parts correspond to full detachment. The entire crack propagation process takes less than 60 msec for the optimal set of parameters while it takes around 2.53 sec for the non-optimal case. (e) Experimental pull-off force F_{off} results at different β and θ values. Each data point is an average of six measurements and the error bar indicates the standard deviation. Copyright © 2015 American Chemical Society. 22
- 2.5 Contour plots of normalized experimental pull-off stress Φ values as a function of β and θ for (a) ST-1060 and (b) ST-1087 mushroom-like polyurethane fibers. (c) Φ versus χ for both ST-1060 and ST-1087 fibers at different wedge angles. Copyright © 2015 American Chemical Society. . 24

3.1	(a) Schematics of fabrication process steps of the FAM: (i) molding micro-fibers, (ii) spin-coating the membrane, (iii) mounting the gripper body, and (iv) curing and releasing the FAM, (b) Fabricated FAM on a gripper, (c) Scanning electron microscope (SEM) image of a cross-section of the FAM. (d) SEM image of micro-fibers with mushroom-shaped tip endings. (Copyright © 2014 IEEE)	28
3.2	Force measurement set-up: (a) schematic figure and (b) photographic image.	29
3.3	Schematics of the pick-and-release manipulation process steps of a soft gripper using the FAM: For picking manipulation, (a) the gripper conforms to the objects 3D shape and applies an additional preload using an internal air force F_a , (b) the internal air force is relaxed, (c) the part is picked from a donor substrate, and (d) the object is carried to a desired position. For releasing, (e) the object is placed onto a receiver substrate, (f) the FAM is inflated by an internal air pressure while the gripper is being moved upward, (g) the micro-fibers are peeled off during the inflation of the membrane and only several fibers stay in contact with the object just before its release, and (h) the object is fully released. (Copyright © 2014 IEEE)	31
3.4	reaction force profile of pick-and-release manipulation of a 19.1 mm diameter steel ball: video snapshots in (a)-(d) correspond to the picking mechanism steps 3.3.1 and video snapshots in (e)-(h) correspond to the releasing mechanism steps 3.3.2 described in Figure 3.3. Below plot shows the reaction force data during each pick-and-release manipulation step.	32

3.5	Picking force measurement on a flat glass surface: (a) schematic images and snapshots of the FAM retracted from a glass surface with no air pressure (i iii), and microscopic images at the edge of the contact showing a recession of the peel zone with increasing the gripper movement (iv vi), (b) reaction force (F_r) of the FAM and the flat membrane without applied air pressure at 0.01 mms^{-1} of retraction speed (i: applying a preload force (F_{pre}), ii: releasing preload, iii: retracting the specimen, iv: reaching to pull-off force, v: pulled off from the surface), and (c) pull-off force of the FAM and the flat membrane on a flat glass surface under the no air pressure in terms of preload. Each data point is the average of three experiments, and the error bar indicates the standard deviation. (Copyright © 2014 John Wiley & Sons, Inc.)	35
3.6	Releasing force measurement on a flat glass surface: (a) Schematic images and snapshots of the inflated FAM retracted from a glass surface with a positive air pressure (i iii), and microscopic images of the contact area showing all fibers are peeled off at once but a single fiber remaining at the center (indicated as a white circle) before the FAM is completely pulled off from the surface (iv vi), (b) reaction force of the FAM under the positive air pressure corresponding to 7.0 mm of vertical displacement at the center. The retraction speed is 0.1 mms^{-1} (corresponding pull-off force is indicated as a red dashed arrow in Figure 3.6(c)), and (c) pull-off force of the FAM on a flat glass surface under positive air pressure in terms of inflation distance at the center z_i The green dashed line indicates the minimum pull-off force of a single fiber. Each data point is the average of three experiments, and the error bar indicates the standard deviation. (Copyright © 2014 John Wiley & Sons, Inc.)	37

3.7	Adhesive forces of the FARP and the FAM on various diameters of steel balls ranging from 1.6 mm to 25.4 mm: (a) pull-off forces of the FARP in terms of the applied preload. The dashed box is a magnification of the force plots within 0 to 0.15 N of preload range, (b) pull-off forces of the FAM in terms of the applied preload, (c) photographic images of the FARP holding a 5.5 mm in diameter steel ball (i), and the FAM holding a 19.1 mm diameter steel ball (ii), (d) The picking force comparison of the FAM, FARP, and the flat membrane in terms of ball diameter. Each data point is the average of three experiments, and the error bar indicates the standard deviation. (Copyright © 2014 John Wiley & Sons, Inc.)	39
3.8	Contact condition of a membrane depending on the thickness profile: (a) photographic image of cross-section of the flat membrane, (b) SEM image of the left edge of the flat membrane, (c) SEM image of the center of the flat membrane, (d) SEM image of the right edge of the flat membrane, (e) optical microscopic images of the edge of the FAM (left: unfiltered, right: filtered) and (f) optical microscopic images of the edge of the flat membrane (left:unfiltered, right: filtered).	42
3.9	Schematic of regime I and regime II during retraction of the gripper: (i) the initial stage of retraction of the gripper whose vertical displacement is dominated by deformation of the regime I, (ii) after the initial stage of the retraction of the gripper whose vertical displacement is dominated by detachment of the regime II.	43
3.10	Analytical modeling of picking force of the FAM at regime I: (a) SEM image of cross-section of regime I of the flat membrane, (b) schematic of undeformed regime I simplified to be a triangular cross-section, (c) schematic of deformed regime I under the reaction force due to adhesion of regime II, and (d) analytic solutions of vertical displacement z_1 depending on the reaction force. Analytical estimations for the fabricated FAM were marked with a red arrow in (d).	46

3.11	Analytical modeling of picking force of the FAM at regime II: (a) Shape of deformation of the FAM while it is retracted from a flat surface under no air pressure, (b) Definition of parameters for the modeling, (c) reaction force F_r depending on vertical displacement z for different work of adhesions ω_{ad} , (d) reaction force F_r depending on vertical displacement z for different membrane thicknesses h_0 . Analytical estimations for the fabricated FAM were marked with red arrows in (c) and (d). (Copyright © 2014 IEEE) . . .	49
3.12	Picking force measurements and verification of the developed analytic model: (a) reaction force profile of three FAMs in terms of time (i:contacting with a surface, ii: applying a preload, iii: retracting, iv: achieving the maximum reaction force, and v: pulled off from the surface) and (b) the reaction force profile of three FAMs F_r depending on vertical displacement z and analytical solution (indicated by solid line). all three FAMs are tested three times per each samples.	51
3.13	Analytical modeling of the releasing force F_{rs} : (a) Schematic figure of the shape of the inflated FAM, (b) Magnified figure of micro-fibers remained in contact at an inflated configuration, (c) Magnified figure of the contact area at an inflated configuration, and (d) Analytic estimation of the releasing force model depending on the inflation distance z_i where k represents the k^{th} fiber and the experimental results with 0.01 mms^{-1} of retraction speed. (Copyright © 2014 IEEE)	55
3.14	Demonstration of pick-and-release manipulations of the inflatable and adhesive Gripper: (a) three different sizes of steel balls (4.76, 5.55 and 6.35 mm diameter) in parallel, (b) a piece of $24 \times 40 \times 0.13 \text{ mm}^3$ fragile cover glass (indicated by the red arrow and the white frame), and (c) 22 array of 1 mm diameter silicon disks (indicated by the white dashed box) ((i): applying a preload; (ii): picking up; (iii): inflating the FAM; (iv): releasing). (d) an electrical resistance, (e) a $5 \times 5 \times 5 \text{ mm}$ right angle prism, (f) a 60 mm long metal wrench, and (g) a paper clip (left: picking up; right: releasing). (Copyright © 2014 IEEE and Copyright © 2014 John Wiley & Sons, Inc.)	60

4.1	Demonstration of the proposed soft adhesion-based gripping system holding various 3D objects such as a (a) rounded glass flask filled with 200 mL of liquid (total weight of 307 grams), (b-d) 118 gram coffee cup, (e) 41 grams pair of cherry tomatoes, and (f) 139 gram plastic bag. The scale bar is 10 cm.	62
4.2	Schematics of structure, mechanism and a representative adhesion test of the soft adhesion system. (a) A cross-section of 3D assembly of the proposed system from side (I) and from bottom (II) of the system. 1: silicone tubing, 2: vinylsiloxane, 3: outer case, 4: rubber ring, 5: soft chamber, 6: spacer between the chamber and the FAM, 7: the FAM, 8: mushroom-shaped PDMS micro-fibers. Larger scale bars (black) indicate 5 mm, while the smaller scale (white) inside of the inset in (II) corresponds to 100 μm . (b) A schematic of the proposed system when pressurized with a negative pressure differential (ΔP) (I) and pulled with a pull-up load (F_{pull}) (II). The inset (III) shows a schematic of pressure distribution between the spacers in the soft chamber and adhesion stress on the contact interface. (c) Adhesion test of the soft system. A schematic of experimental procedure (I), snapshots of the soft system under a negative pressure differential on a 30 mm diameter glass hemi-sphere in accordance with each step (II), and corresponding profiles of reaction force (F_r) and pressure differential inside the chamber with respect to elapsed time (III). The initial pressure (ΔP_o) here is approximately -47 kPa. The numbers indicated in green are correlated with the experimental procedure: (1) approaching, (2) preloading, (3) applying initial pressure, (4) pulled off, and (5) detached.	64
4.3	Experimental procedure for fabricating the FAM. A schematic shows the individual steps of the fabrication process.	66

4.4	3D scanned images of PDMS patterns and dimensions. (a) 3D image (I) and profile (II) of cylindrical PDMS patterns with 52 μm diameter, 48 μm spacing and 38 μm height. (b) 3D image (I) and profile (II) of mushroom shaped PDMS patterns with 69 μm diameter, 31 μm spacing and 42 μm height. Note that the pillar stems of the mushroom shaped patterns cannot be measured since they are covered by the overhanging tips.	67
4.5	SEM images of mushroom-shaped elastomer micro-fiber arrays on the FAM. Top (a) and side-view (b) of mushroom-shaped micro-fiber arrays with 69 μm in diameter, 31 μm in spacing, and 42 μm in height. (c) A side-view of the FAM supported by a thin backing layer with ca. 250 μm in thickness.	68
4.6	Experimental procedure for fabricating the rigid adhesion system. A schematic shows the individual steps of the fabrication process for obtaining a rigid system with the FAM.	69
4.7	Experimental procedure for fabricating the soft adhesion system. A schematic shows the individual steps of the fabrication process for obtaining a soft system with the FAM.	70
4.8	Finite element analysis for modeling vertical stress within the FAM. (a) A schematic of dimensions and boundary conditions of the FAM clamped at the edge and being pulled up by a rigid support under a negative pressure differential (ΔP_o). (b) A colormap of normalized vertical stress (σ_{22}/E_m) within the FAM for selected normalized pressures $\hat{p} = ((1 - \nu^2)\Delta P_o)/E_m$. (c) A ratio in the vertical stress between the edge and the center ($\sigma_{22,e}/\sigma_{22,c}$) depending on the normalized pressure \hat{p} Here, $\sigma_{22,e}$ is the vertical stress on the first fiber from the edge of the FAM and $\sigma_{22,c}$ is on the fiber at the center.	73

4.9 Analysis and force measurements in the rigid adhesion system for different 3D geometries. (a) A schematic of the rigid adhesion system being pulled off from a spherical substrate under a negative pressure differential (ΔP_o). Blue arrows indicate the direction of reaction force (F_r). (b) Calculated reaction force (F_r) profiles on a flat glass surface versus retraction distance (z_r) for various initial pressures (ΔP_o). (c) Calculated pull-off force (F_{off}) as a function of the diameter (d_b) of glass spheres for varying thicknesses (h_0) (I), and Youngs moduli (E_m) (II). (d) Calculated pull-off force (F_{off}) as a function of diameter (d_b) of the glass sphere for varying works of adhesion (ω_{ad}) (I) and initial pressures (ΔP_o) (II). In all of these plots, the default parameter values are $h_0 = 0.2$ mm, $E_m = 2.1$ MPa, $\omega_{ad} = 4.0$ J·m⁻², and $\Delta P_o = 0$ kPa. (e) Measured reaction force profiles on a flat glass surface with respect to retraction, depending on different initial pressures. (f) Measured pull-off forces on glass substrates with different curvatures depending on the initial pressures. Each point indicates an average of 5 measurements, and error bars are 1 SD (standard deviation). 90

4.10	Schematics of the analytical model for the rigid adhesion system with different boundary conditions. (a) A schematic of the rigid adhesion system in contact bigger than a spherical substrate. (b) A schematic of the contacting rigid adhesion system with a diameter that is smaller than that of the spherical substrate. (c) A schematic of the rigid adhesion system being delaminated from a flat glass substrate under a negative pressure differential (ΔP). Green arrows show the forces caused by the pressure differential acting on surface of the adhesion system, which can pull the FAM into the rigid chamber and cause delamination of the membrane. (d) An inverted optical microscope image of the FAM on the rigid adhesion system in contact with a flat glass substrate, visualizing the contact interface. Dark areas indicate micro-fibers on the FAM in contact. The scale bar is 500 μm . (e) A schematic of the total volume (V) as a sum of the initial volume (V_0) and the additional volume created by the truncated-cone shaped deformation of the FAM (V_t), subtracted by the volume of the spherical substrate covered by the FAM (V_c). h_c is the height of the spherical cap (V_c).	91
4.11	(a) Calculated reaction force (F_r) profiles on a flat glass surface with respect to retraction distance (z_r), depending on effective contact radius (r_e). Here, the difference in the effective contact radius represents the difference in the initial contact area. (b) A magnified view for the reaction force profile in the beginning of retraction when $r_e = 8.0$ mm. Small numerical instabilities can be observed in the beginning of retraction when $r_e = R_0$. The first derivatives of the total potential energy (Π) with respect to vertical displacement (z) and contact radius (r) are numerically obtained using the forward ($r_e = R_0$), centered ($0 < r_e < R_0$), and backward ($r_e = 0$) difference approximations. Here, the vertical displacement and contact radius are discretized in 20,001 and 50,001 elements, respectively.	92
4.12	Customized experimental setup for characterization of adhesion systems.	93

4.13	Characterization of adhesion stress (σ_{ad}) of a single micro-fiber on the FAM for the soft adhesion system. (a) Visualization of the contact area of three micro-fibers for each samples using the confocal laser microscope. Scale bar = 100 μm . (b) Reaction force (F_r) profiles of three micro-fibers for each sample.	93
4.14	Characterization of the effective work of adhesion (ω_{ad}) and adhesion stress (σ_{ad}) of the FAM for rigid and soft adhesion systems. (a) A reaction force (F_r) profile of the FAM for the soft system (I), in accordance with microscopic images on the interface (II). (b) A reaction force (F_r) profile of the FAM for the rigid system (I), in accordance with microscopic images on the interface (II). 1: preloading, 2: retracting, 3: exerting pull-off force, 4: detached. Scale bars indicate 1 mm.	94
4.15	Characterization results of the soft adhesion system. (a) Measured reaction force (F_r) profiles on a flat glass surface with respect to retraction, depending on different initial pressures (ΔP_o). (b) Measured pull-off forces (F_{off}) on various substrates depending on the initial pressures. (c) Conversion ratio ($\sigma_{ad}/\Delta P_o$) on various substrates as a function of initial pressure. Each point in (b) and (c) indicates an average of 5 measurements, and error bars are 1 SD. (d) Schematics of the soft system being pulled off from the flat glass without a change in the internal pressure (P_i) (I), and under a high negative pressure differential (II). (e) Side-views of the soft system being pulled off from the flat glass at 1.7 kPa of the initial pressure (I), and corresponding microscopic images of the contact interface (II). The estimated crack propagation speed is 1.5 $\text{m} \cdot \text{s}^{-1}$. (f) Side-views of the soft system being pulled off from the flat glass at -52 kPa of the initial pressure (I), and corresponding microscopic images of the contact interface (II). The estimated crack propagation speed is 179 $\text{m} \cdot \text{s}^{-1}$. (g) Microscopic images of the contact interface of the soft system with a less adhesive FAM being pulled off from the flat glass at -46 kPa of the initial pressure. Scales in (e-II), (f-II) and (g) indicate 1 mm. The moment at which the FAM is detached is set to be zero seconds (0 s).	95

4.16 Scaling of the soft adhesion system compared to a flat micro-fiber array and biological gecko adhesives. The scaling of gecko foot-hair adhesion is for shear stress (σ_{sf}) on a flat substrate, while the other results in the soft system are for normal adhesion stress (σ_{ad}) on both 3D curved (circles) and flat surfaces (rhombuses). Dashed lines are the least-squares trends in the adhesion stress of a single fiber, the micro-fiber array, and the soft system measured on the both flat glass and spheres with 15, 30, and 60 mm diameters with (blue) and without (red) a negative initial pressure. The green line is the scaling from the single fiber to the micro-fiber array. Each data point indicates an average of 5 experimental measurements. 96

Chapter 1

Introduction

1.1 Motivation

Biological adhesive systems in nature possess inherent softness capable of adapting to a wide range of unstructured environments without requiring any sophisticated control mechanism when gripping and releasing the surfaces [2]. Geckos, one of the biggest species in nature using adhesive mechanism in climbing and running on a vertical wall, have hierarchically structured fibrillar adhesive systems ranging multi-scales from a micro-seta down to a nano-spatulae, being able to produce enormous adhesion and friction to support its body weight with just a single toe (Figure 1.1) [3, 4, 5]. Made out of rigid beta-keratin which is also known as the same material with human nails, the multi-level hierarchical structure of gecko's fibrillar foot-hairs allow the gecko to distribute an applied interfacial load over the contact interface more effectively and evenly without compromising its ability to adapt to arbitrary shapes and roughnesses of three-dimensional (3D) surfaces.

Researches related to the gecko's fibrillar foot-hairs have dramatically changed people's perspective view on adhesion [6, 7, 8, 9, 10, 11, 12, 13, 14, 15, 16]; strong but reversible adhesion is not only the area of surface chemistry, but can also be stem from the mechanics of geometry at the interface which can dramatically affect on the fracture strength by changing the status of load distribution. In the past decade, various synthetic micro- and nano-fibrillar adhesives inspired by the gecko's foot hairs have been developed, exhibiting

enhanced adhesion on a flat surface (Figure 1.2(a), iv-vi [17, 18, 19]), as well as controlling it by exploiting a difference in effective stiffness of slanted micro-/nano-fibrillar structures upon shearing direction, allowing the fibers easily peeled off from the contact surface as the geckos do (Figure 1.2(a), i-iii [12, 20, 21]).

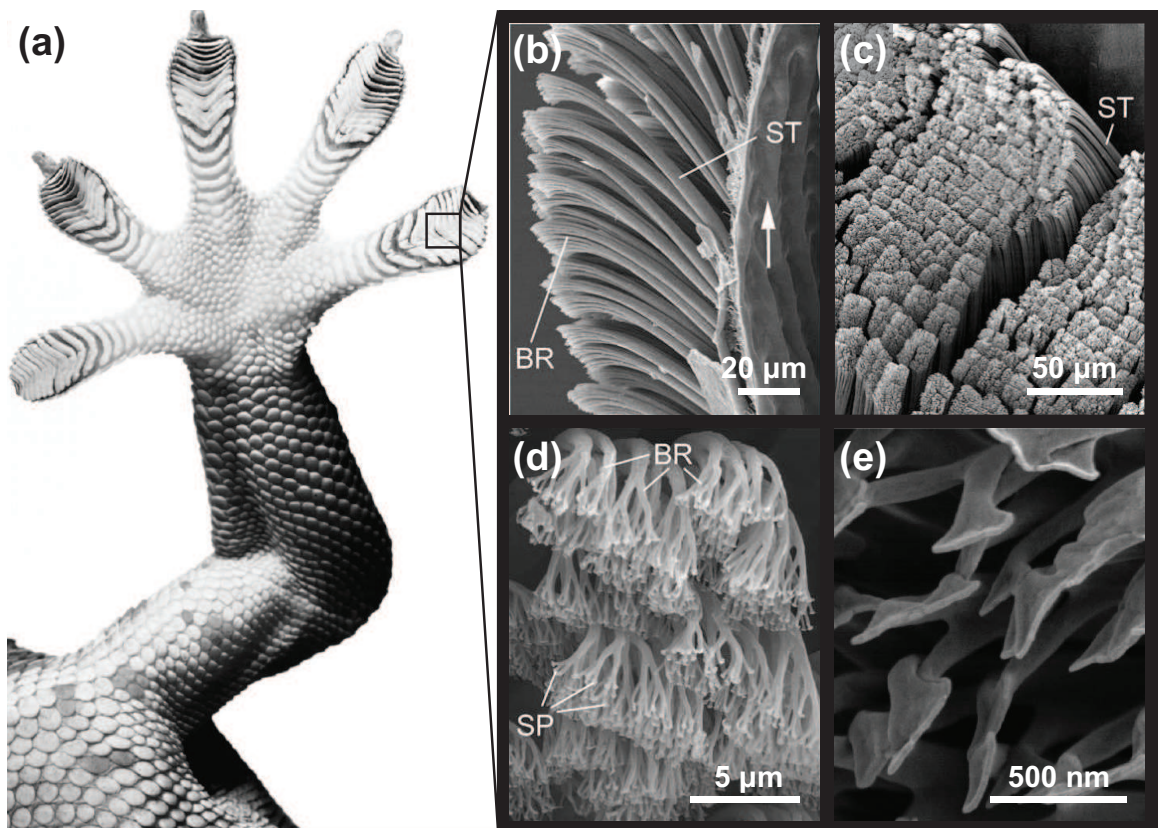


Figure 1.1: An overview of geckos' hierarchical fibrillar foot-hairs from macro-scale to nano-scale: (a) A Tokay gecko's foot on a flat glass, (b) a scanning electron microscopy (SEM) image of geckos' setae from side, and (c) the top, (d) a SEM image of tips of geckos' setae, and (e) a SEM image of numerous spatulae. ST: Seta, BR: Branch, and SP: Spatula

Despite of more than a decade of extensive researches on gecko-inspired fibrillar adhesives, many scientific/engineering challenges have not been addressed successfully for practical applications of the gecko-inspired fibrillar adhesives to industries and our daily lives. In micro-scale, although many theories and several preliminary experiments have investigated effect of the fibrillar geometries on the interfacial bond strength, systematical

experiments in testing the adhesion of different shapes of micro-fibrillar adhesives have not been conducted due to the lack of fabrication methods for controlling the shape of tip-endings of micro-fibers with high resolution. In macro-scale, previous gecko-inspired controllable adhesion mechanisms have been optimized and demonstrated for planar or simple shape of objects without the ability of dealing with complex 3D geometries (Figure 1.2(b) [22]), as the fibers exploits mechanical interaction with the objects when applying shear force for peeling, which their releasing performance can be significantly dependent on the object shapes [23, 24]. Also, using a soft adhesive interface (i.e., a membrane) for 3D conformability causes high stress concentration and low interfacial fracture strength, posing a fundamental dilemma which preventing a successful use of fibrillar adhesives for soft robots in gripping and locomotion on the complex 3D surfaces.

This thesis work aims at developing principles and knowledge on the interfacial load distribution and its control in multi-scale, depending on various design parameters of the gecko-inspired micro-fibrillar adhesive pads (e.g., tip-shape of micro-fibers or air pressure behind the membrane-backed micro-fiber array). The contributions of this work can be applied for broadening possible applications of the micro-fibrillar adhesives in various robotic areas, such as transfer printing systems [25, 26, 27, 28], robotic manipulators [29], and mobile robots that can climb on complex 3D surfaces, such as aircraft, space shuttle, or pipe surfaces [30, 31, 32].

1.2 Interfacial load sharing on micro-contact depending on different tip-geometries

K. Autumn *et al.* and G. Huber *et al.* have discovered that the strong adhesive force of the gecko's foot-hairs is mainly due to a combination of van der waals forces [33], which is normally considered as a weak intermolecular force, and possibly capillary forces [34]. The hierarchical fibrillar structures and spatulated tip-endings can significantly enhance these weak forces by improving surface roughness adaptability [35, 36], crack

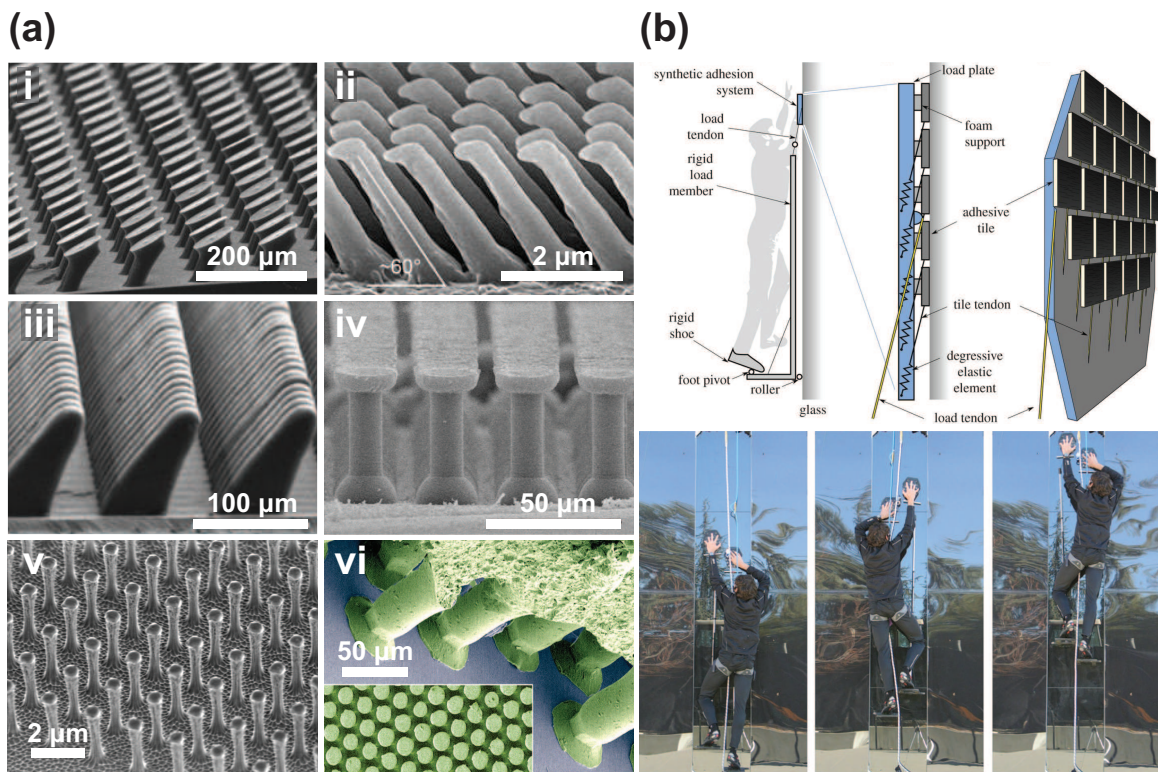


Figure 1.2: Previous works on gecko-inspired synthetic micro-fibrillar adhesives and equal load sharing system, ranging from micro-scale to macro-scale: (a) gecko-inspired slanted micro-wedges for enhanced friction (i-iii), and mushroom-shaped micro-fibers for the maximal adhesion with equal load sharing on micro-contact (iv-vi). (b) Design of synthetic load sharing system for friction on flat surface, capable of distributing the applied load to the load tendon and adhesive tiles evenly (top). Still frames of a 70 kg climber ascending a vertical glass wall using the device (bottom).

trapping [37] and increasing the effective work of adhesion [4, 38]. Especially, it has been revealed that the interfacial load sharing on individual micro-contacts of spatula plays a critical role in the enhanced adhesion [39, 40], suggesting that optimal tip-endings can dramatically improve the adhesion performance of the synthetic micro-fibrillar interfaces (Figure 1.2(a), iv-vi) [41].

Various theories have been proposed regarding the optimal shape of tip-endings, and verified experimentally. For example, Campo *et al.* tested various elastomeric micro-fibers with different tip shapes experimentally and found out the mushroom-like fiber-tip could provide the highest adhesion among many other tip patterns [42]. Aksak *et al.* theoretically studied the optimal shape of mushroom-like tip-endings of elastomeric micro-fibers as a function of tip diameter relative to stalk diameter (β) and the tip-ending wedge angle (θ). They reported β of 1.1 – 1.2 and θ of 45° as the optimal fiber parameters for the maximal adhesion [43].

Even though the previous work [43] has already computed the optimal shape of mushroom-like tip-endings for the maximal adhesion for elastomeric micro-fibrillar structures, the theory has not been experimentally validated yet due to limitations on fabrication of 3D optimal micro-/nano-structures. Benefiting from an emerging high-resolution 3D micro-/nano-fabrication technique called two-photon stereo nano-lithography techniques, we can precisely control different β and θ values and manufacture the elastomeric micro-fibers with high resolution enough to verify such optimal designs in theory.

1.3 A soft robotic gripper with controllable adhesion of micro-fibrillar adhesives on 3D surfaces

Soft robotics is a new emerging robotic field that develops robots out of soft matters (e.g., elastomers) capable of adapting various complex and unpredictable environments, not based on control systems but on the material properties and mechanical structures.

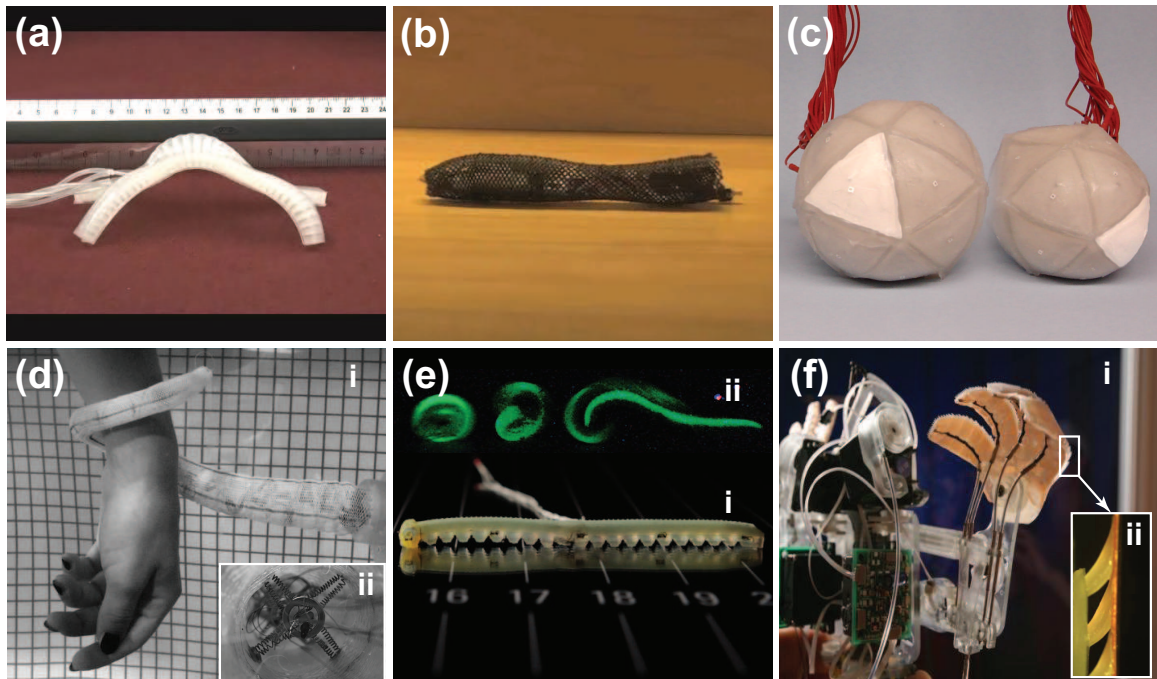


Figure 1.3: State of the art in soft robotics: (a) A pneumatically driven gaiting robot made out of soft deformable elastomer, (b) a peristaltically crawling soft robot driven by SMA actuators, (c) a sphere-shaped rolling robot based on jamming, (d) a soft manipulator wrapping around a human's hand (i) and its cross-section inspired by the muscle structure of octopus arm (ii), (e) a soft-bodied caterpillar robot (i) and its ballistic rolling locomotion (ii), and (f) a wall climbing robot (i) using gecko-inspired elastomeric micro-wedge structures (ii).

Figure 1.3 shows state-of-the-art soft robots developed by previous works. Body of those soft robots is made out of polymer-based elastomers which are not conventional for robotic systems composed of steels or plastics [44, 45, 46]. Instead of using common actuators such as electromagnetic motors and combustion engines, the soft robots make use of a difference in volumetric change of heterogeneous structures under pneumatic pressure differential (Figure 1.3 (a) [44]), a displacement of smart materials (e.g., Shape Memory Alloys(SMA)) (Figure 1.3 (b) [47]), or stiffness change in granular media (Figure 1.3 (c) [48]). movements of those soft robots are highly bio-inspired as well; motions are based on rolling (Figure 1.3 (c) [48] and (e) [49]), crawling (Figure 1.3 (a) [44] and (b) [47]), bending of a continuous body(Figure 1.3 (d) [50]), or climbing by adhesion(Figure 1.3 (f) [51]). The soft robots can conform to various surface geometries, distributing stress over a larger volume, and increasing contact time and minimizing the impact force [52]. In addition, comparing to the conventional robots comprised of a number of sensors and actuators, the soft robots can do the same tasks without requiring sophisticated control theories or path planning. The above features of the soft robots are crucial in interacting with unstructured environments or humans.

The aforementioned properties of soft robots can be a significant advantage for handling fragile objects with irregular geometry which are difficult for the conventional manipulators composed of rigid components such as electromagnetic actuators and sensors. Various soft grippers have been developed as shown in Figure 1.4. F. Ilievski *et al.* developed a soft pneumatic starfish-shaped gripper, and showed pick-and-release manipulation of an uncooked egg and a living animal successfully (Figure 1.4 (a)) [53]. J. R. Amend *et al.* developed a soft gripper using rigidity tuning of granular media based on particle jamming, and demonstrated the ability of handling a wide variety of different shapes of objects (Figure 1.4 (b)) [54, 55]. N. G. Cheng *et al.* developed a trunk-like manipulator based on the jamming technique, and successfully demonstrated the manipulator's ability to conform to irregular geometries of 3D objects (Figure 1.4 (c)) [56]. A. Pettersson *et al.* used magnetorheological (MR) fluid to mold irregular exteriors of soft and crushable food products by applying an magnetic field, exhibiting a high gripping force without bruising those fragile foods during manipulation [57].

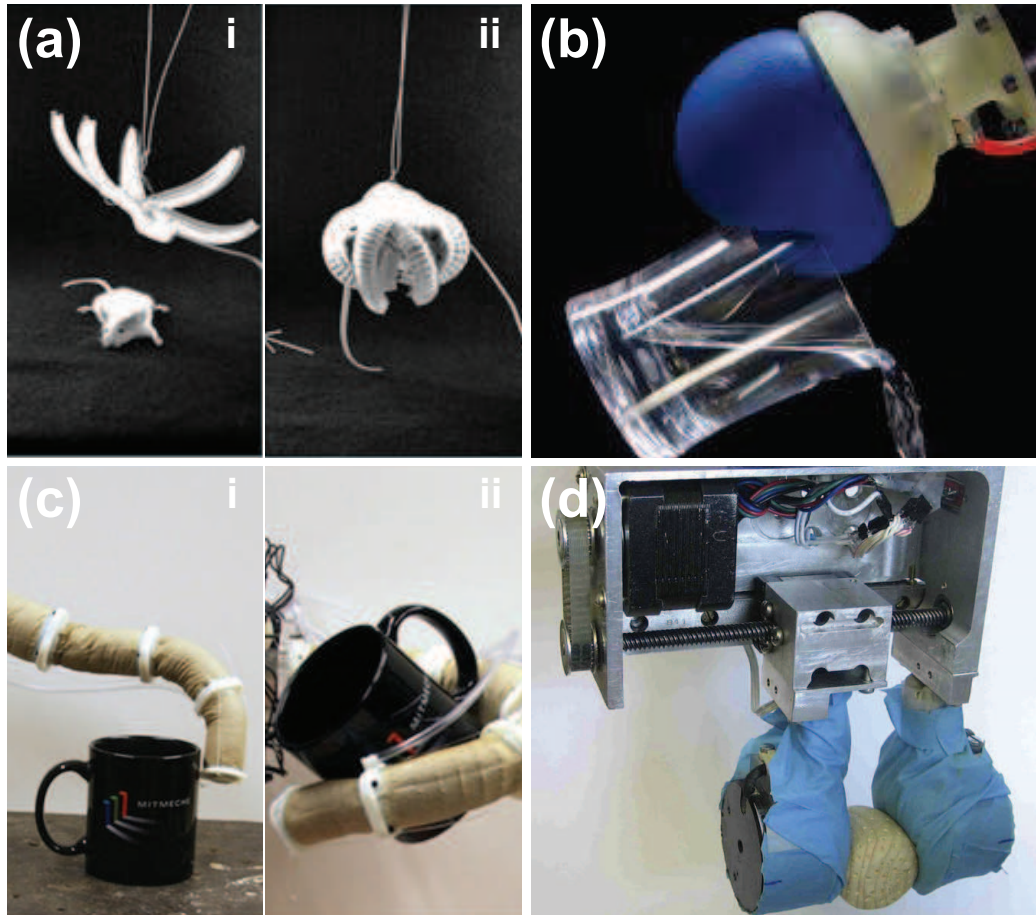


Figure 1.4: Soft robotic manipulators: (a) A starfish-shaped soft gripper catching a paralyzed mouse (i:approaching, ii:gripping), (b) a universal gripper pouring a glass of water, (c) a trunk-shaped soft manipulator wrapping around a cup (i:approaching, ii:wrapping), and (d) a soft gripper having pouches filled with magnetorheological fluids to mold objects' shape.

These manipulators have demonstrated the capacity of soft robotic hands being able to handle a wide variety of objects based on much simple control mechanisms with a cheaper price than the conventional rigid manipulators [58]. However, those soft grippers are still subject to geometrical features of the target objects similar to the conventional manipulators, as both soft and rigid grippers are based on the same principle of mechanical interlocking. Such grippers have difficulties in handling flat and thin objects which can be hard to be clipped. Not only the shape, but also size of the object has significant impacts

on its gripping performance; for example, gripping force of the jamming-based soft gripper will be significantly reduced, if size of the object is larger than 90 % of the gripper size [55] or contact angle between the object and the gripper is smaller than 45 deg [54].

The adhesion-based soft gripping mechanism can address the aforementioned issues on the principle of mechanical interlocking, or limitations of suction for 3D objects when securing an air-tight sealing at the interface [59]. A beauty of the adhesion-based soft grippers lies on the simple principle of adhesion that the gripping force is in proportional to the contact area, which allows a universal design of a soft gripper for a wide variety of 3D and planar objects in size, shape, and number. Developing an adhesion-based gripper, however, is difficult; while the adhesion mechanism enables objects to be easily picked up, the same mechanism would cause significant difficulties in releasing the objects. Therefore, being able to actively control the adhesion during pick and release steps is critical when developing such adhesion-based gripping devices [51].

Various controllable adhesion mechanisms for robotic manipulations using the gecko-inspired fibrillar adhesives have been developed in the previous arts, mainly suitable for thin and planar objects or ultra-lightweight micro-particles [20, 25, 26, 28, 60, 61, 62]. The micro-fibrillar structures in the previous works have been fabricated onto a rigid backing, resulting in limited payload on 3D surfaces due to the subsequent small contact area as shown in Figure 1.5 (a). For non-planar 3D parts, as shown in Figure 1.5(b), the micro-fibrillar adhesives must be incorporated with a soft backing (i.e., membrane), so that they can adapt to the non-planar surface geometries.

Several studies have investigated the effect of a soft backing on the fibrillar adhesion to a flat surface [63, 64]. Although J. Lee *et al.* demonstrated that a gecko-inspired lamellar structure can increase the adhesion of nano-fibers on surfaces with micro-scale roughness [65], no studies have fully explored the influence of backing softness on 3D object manipulation in macro-scale. Not only improving the ability to adapt to 3D surface geometries for enhanced and robust adhesion, but the soft and stretchable backing can also provide another degree of freedom for controlling the adhesion of fibrillar structures

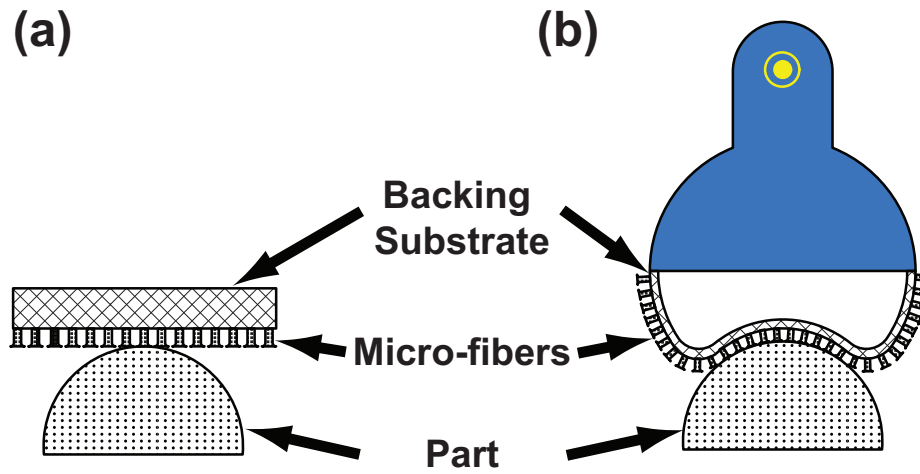


Figure 1.5: Schematics of picking up a non-planar 3D part: (a) A fibrillar adhesives on a rigid backing layer and (b) a soft gripper using the fibrillar adhesives on a soft membrane backing.

without using the principle of mechanical interactions. Unlike a rigid backing, the micro-fibrillar structures on a soft backing can easily be peeled off by stretch of the membrane during inflation, effectively reducing the contact area down to a single fiber-tip contact.

1.4 Interfacial load distribution control for a soft adhesive membrane on 3D surfaces

As we discussed above, by exploiting the principles of equal load sharing [41] and the interfacial crack pinning [37], the geckos can firmly adhere to planar surfaces with the van der Waals force [33]. Using the same attachment method, the synthetic fibrillar adhesives achieve bond strengths of over 100 kPa on smooth flat surfaces [66], surpassing the performance of the geckos on such surfaces [67], and exhibit quick release through peeling [68] or buckling [16] of the micro-fibers.

Although the micro-fibrillar adhesive structures formed onto a soft membrane backing exhibits robust adhesion and high controllability, the membrane is subjected to high stress

concentration on the contact interface, imposing a significant loss in interfacial bonding strength. According to our test and previous work, despite demonstrating a significant improvement over an unstructured elastomeric membrane with 10 times higher adhesion, the structured membrane with micro-fibrillar adhesives could achieve only 2 kPa of adhesion stress, a small fraction of the 55 kPa measured with rigid-backed micro-fiber arrays [69]. This implies that the improved conformability to 3D surfaces enabled by the more compliant membrane backing is at the expense of a 96% reduction in adhesion strength. Considering that the adhesion of a membrane scales with the circumferential length of the contact interface and not with the area [29], the results above suggest that the size of the membrane, whether containing structures or not, has to be vastly increased in order to support a high load-carrying capacity.

For a broad range of robotic applications, such as wall climbing [30, 51], perching devices for flyers [70], and grippers [20, 25, 62, 71], the applied load on an adhesive interface must be uniformly shared over the entire area in contact, so that the adhesion can be scaled by the area [72], as it does with a rigid backing. Hawkes *et al.* proposed a rigid frictional attachment systems that could improve the lateral load sharing capability and friction of micro-wedge structures by scaling up to larger areas on flat and slightly curved surfaces (Figure 1.2 (b)) [22]. However, no attachment system has succeeded yet in improving the perpendicular load sharing and adhesion of fibrillar structures for complex 3D surfaces. A backing layer made out of stiffness-tunable materials such as liquid metals [73], thermoplastics [74, 75] or shape memory polymers [76, 77] can adapt to 3D surfaces when they are soft and support high fracture strength when they are hardened. However, challenges still remain in managing deformable substrates (e.g., plastic foils, rubber-like stretchable surfaces, thin metal films), because the stiffened backing cannot accommodate deformation, resulting in stress concentrations at the contact edges. Therefore, all adhesive gripping tasks are limited by a fundamental dilemma between compliance/conformability and rigidity/strength [78]; while adhesives must be compliant enough to conform to complex 3D or deformable geometries, the same system must remain rigid enough to maximize interfacial (Mode I) fracture strength in order to support the objects weight.

1.5 Research Objectives

In this thesis work, principles on the load distribution and its control for the gecko-inspired fibrillar adhesive interfaces are investigated in multi-scale, ranging from a micro-contact of a single fiber-tip to a centimeter-sized membrane-backed micro-fiber array on 3D surfaces. The findings are then applied for developing a soft robotic gripper for pick-and-place manipulation and transfer printing of a wide range of various 3D objects in size, shape, and number.

The main objectives of this thesis work are:

- investigating effect of tip-shapes on the maximal adhesion of gecko-inspired micro-fibrillar adhesives with a series of experiments with precisely defined tip-geometries by two-photon stereo nano-lithography.
- Fabricating fibrillar adhesives on a membrane (FAM) by integrating micro-fibers with a soft and stretchable backing for enhanced interfacial bond strength and high controllability in adhesion for 3D surfaces. We also develop a soft robotic gripper capable of pick-and-place manipulation of various 3D objects in size, shape, and number. Finally, we confirm advantages of the FAM over the micro-fiber adhesives on a rigid backing or unstructured membrane for 3D object manipulation using force measurements and analytic models.
- Developing a soft robotic architecture to control the interfacial load distribution of the FAM on complex 3D surfaces by exploiting the influence of internal pressure. We also investigate effect of various design parameters of the FAM (i.e., thickness, stiffness, and work of adhesion of the FAM) on the membrane adhesion for different radii of curved surfaces.

1.6 Thesis Outline

In this work, Chapter 2 discusses about the experimental investigation on the effect of various tip-ending shapes on the normal adhesion of micro-fibrillar adhesives, characterized by the ratio between tip-to-stalk diameter (β) and wedge angle (θ). Fabrications of the mushroom-like tip-endings with high resolution nano-lithography technique are described in the experimental section 2.2, and force measurements of the micro-fibers made out of two different stiffnesses are discussed in the result section 2.3. Chapter 3 discusses incorporating the micro-fiber adhesives with a soft membrane backing; in this chapter, benefits of using the soft membrane backing are verified with experimental measurements of high picking forces on 3D surfaces (section 3.4.2) and high switching ratio (section 3.4.1), as well as theoretical analysis on picking (section 3.5.1) and releasing (section 3.5.2). In Chapter 4, we propose a controllable load sharing mechanism for a soft adhesive interface on complex 3D surface; a finite element analysis (FEA) in the section 4.4.1 shows the influence of internal pressure on the interfacial load distribution among micro-fibers in contact, while our theoretical model in the section 4.4.2 suggests that a pressure differential can be used as a controllable variable for adhesion tuning of a soft adhesive membrane. The theoretical findings are verified through a series of experiments in the section 4.4.2 and 4.5, as well as with demonstrations shown in Figure 4.1. Finally, summary of conclusions and contributions of this thesis work are outlined in Chapter 5.

1.7 Publications

Each sections of this thesis work has been published or presented in the following journals and conferences:

- **Shape Optimization of Micro-fibers for Equal Load Sharing (Contributed Equally)**
 - Hamidreza Marvi*, **Sukho Song***, and Metin Sitti. Experimental Investigation

of Optimal Adhesion of Mushroomlike Elastomer Microfibrillar Adhesives. *Langmuir*, 31(37):1011910124, 2015. [1]

- **Sukho Song***, Hamidreza Marvi*, and Metin Sitti. Experimental Investigation of Maximal Adhesion of Bio-inspired Micro-Fiber Adhesives with Mushroom Shaped Tip Endings. *38th Annual meeting of the Adhesion Society, Savannah, GA*, 2015. (Awarded **Pebbles Award**)

- **Fibrillar Adhesives on a Membrane for Large-scale 3D Surface Grasping**

- **Sukho Song** and Metin Sitti. Soft Grippers Using Micro-fibrillar Adhesives for Transfer Printing. *Advanced Materials*, 26(28):49014906, 2014. [29]
- **Sukho Song**, Carmel Majidi, and Metin Sitti. GeckoGripper: A soft, inflatable robotic gripper using gecko-inspired elastomer micro-fiber adhesives. *Intelligent Robots and Systems (IROS 2014), 2014 IEEE/RSJ International Conference on*, pages 4624-4629, 2014. [79]

- **Load Distribution Control of a Soft-backed Micro-fiber Array on 3D Surfaces**

- **Sukho Song**, Dirk-Michael Drotlef, Carmel Majidi, and Metin Sitti. Controllable Load Sharing for Soft Adhesive Interfaces on Three-Dimensional Surfaces. *Proceedings of the National Academy of Sciences*, 114(22):E4344-E4353, 2017. [80]

Chapter 2

Shape Optimization of Micro-fibers for Equal Load Sharing

2.1 Introduction

In this chapter, we experimentally investigate the optimal design of bio-inspired elastomeric fibrillar structures with mushroom-shaped tip-endings for maximizing the adhesion. Benefiting from the high-resolution three-dimensional (3D) two-photon stereo nano-lithography technique, we manufacture elastomeric micro-fibers with different β and θ values with high resolution enough to verify such optimal designs. Sixteen different mushroom-like tip patterns are fabricated using two different polyurethanes with different stiffness, and their pull-off forces are compared to the theoretical predictions. Finally, the effect of different tip-endings on the adhesion is discussed in terms of the stress distribution and stiffness of the micro-fibers. (This chapter has been reprinted with permission from [1]. Copyright © 2015 American Chemical Society.)

2.2 Experiments

A schematic of a mushroom-like micro-fiber is shown in Figure 2.1a. While we kept the fiber tip diameter ($d_t = 100 \mu\text{m}$) and the fiber length ($L = 100 \mu\text{m}$) constant to have

the same tip contact area and height for all fiber designs, we varied the tip wedge angle θ and the tip diameter relative to stalk diameter β in a range of $30^\circ - 60^\circ$ and $1.1 - 1.5$, respectively. Fifteen different designs of mushroom-like tip-endings were fabricated, in addition to a cylindrical micro-fiber that was fabricated as a control fiber. The designed micro-fibers were fabricated using a UV curable negative photoresist (IP-Dip, Nanoscribe GmbH), which can be polymerized in any arbitrary 3D shape based on two-photon polymerization process. Different steps of the fabrication process are shown in Figure 2.1c.

First, we polymerized the IP-Dip at the desired shape for positive structures using the two-photon lithography machine (Photonic Professional GT, Nanoscribe GmbH). We then developed the photoresist using 2-Methoxy-1-Methylethyl Acetate (PGMA) and hard baked the fibers at 120°C for 30 minutes. Next, we made a negative mold for the fibers using a soft silicon rubber (Mold Max 20, Smooth-On, Inc.; mixed 10:1 by weight). We cured silicon rubber for 24 hours at room temperature. We finally fabricated the positive fibers using both ST-1060 polyurethane (BJB Enterprises, Inc.; mixed 100:55 by weight) and ST-1087 polyurethane (BJB Enterprises, Inc.; mixed 100:50 by weight) elastomers. We degassed polymers 3 minutes after mixing and 10 minutes after pouring them on the mold [81]. Two sets of positive fibers for both ST-1060 and ST-1087 polyurethanes were fabricated and cured for 24 hours at room temperature followed by 16 hours at 71°C . Figure 2.1b shows a scanning electron microscope (SEM) image of a sample polymerized master fiber ($\beta = 1.2$, $\theta = 45^\circ$). Benefiting from the sub-micron resolution of the two-photon lithography, shape of the fabricated master fibers had generally good agreements with the original designs while the tip edge was rounded slightly as shown in the inset of Figure 2.1b. Also, we noticed fabrication defects (broken edge) for the master fiber with $\beta = 1.3$ and $\theta = 30^\circ$ and thus we did not perform any experiments with this fiber.

Adhesion of fabricated micro-fibers was measured by a customized setup shown in Figure 2.2a that was adapted from our previous work [81]. We used a plano-convex glass indenter with a diameter of 6 mm and a radius of curvature of 4.7 mm for our adhesion measurements. Different steps of the adhesion measurement process are illustrated in Figure 2.2b. We first approached a fiber at a speed of $10 \mu\text{m} \cdot \text{s}^{-1}$ and preloaded it with

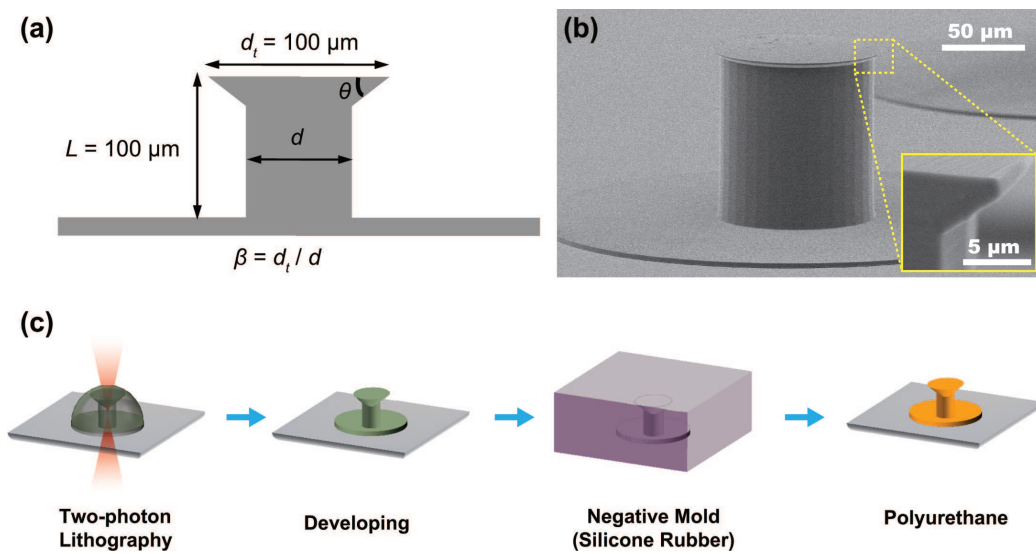


Figure 2.1: (a) Schematic of a mushroom-like elastomeric micro-fiber. (b) Scanning electron microscope (SEM) image of a 3D-printed micro-fiber. The inset shows cross-sectional SEM image of the micro-fiber tip edge, which is slightly rounded. (c) Fabrication process steps for the micro-fibers: 3D-printing the master fiber from a UV-curable photoresist using two-photon lithography, developing it, creating its negative silicone rubber mold, and molding the negative mold with polyurethane elastomers to create positive fibers. Copyright © 2015 American Chemical Society.

2.5 mN of normal load. Next, we made 30 seconds of contact with the fiber to make sure the viscoelastic fiber material was relaxed and the contact force was leveled out. We then retracted fiber at $1 \mu\text{m} \cdot \text{s}^{-1}$ until the indenter was fully detached from the fiber. The pull-off force of each fiber F_{off} was characterized as the maximum negative reaction force during the retraction step.

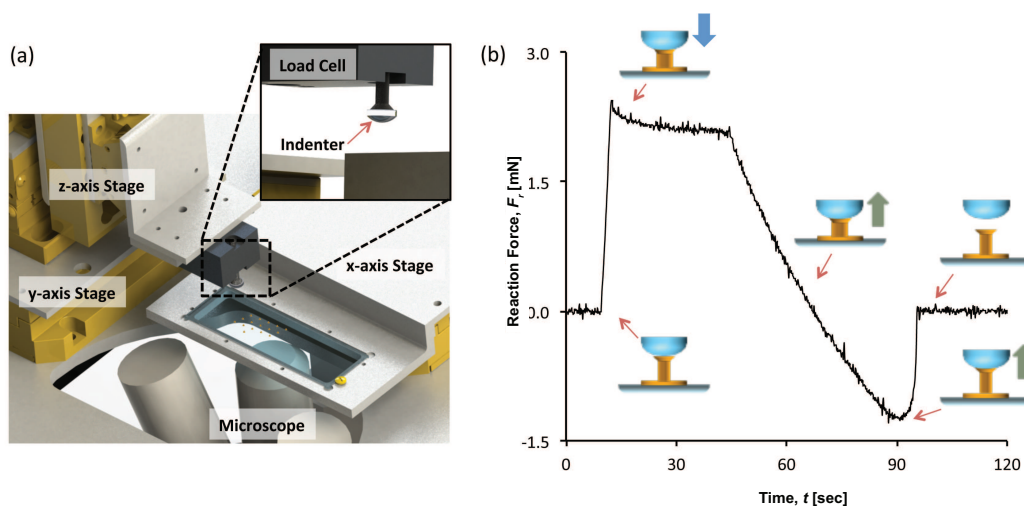


Figure 2.2: (a) Schematics of the custom automated adhesion characterization setup. A spherical glass indenter is attached to a load cell for vertical force measurement. The load cell is connected to a motorized XYZ-stage for motion control. An inverted microscope is used to observe the interaction between fiber tips and the spherical indenter. (b) Different steps of the adhesion test shown on a sample force-displacement data plot: A) The indenter approaches the fiber tip; B) The indenter makes contact with fiber tip and remains in contact for 30 seconds; C) The indenter starts the retraction process; D) The maximum reaction force is measured; E) Full tip detachment occurs. Copyright © 2015 American Chemical Society.

2.3 Results and Discussion

Experimental measurements of reaction force F_r as a function of vertical displacement z for fibers with $\beta = 1.2$ and $\theta = 30^\circ$, 45° , and 60° are plotted in Figures 2.3a and 2.4a for ST-1060 and ST-1087 polyurethane fibers, respectively. When applying a preload, the reaction force is shown to be positive resulting in a positive displacement. With retraction

of the indenter, the reaction force becomes negative exerting the pull-off force as shown in Figures 2.3a and 2.4a. Since the ratio of tip to base diameter β is constant for these samples, slopes of force-displacement curves during the preload are the same for all of them. However, different tip ending wedge angles θ resulted in different pull-off forces; the larger the wedge angle was, the lower the pull-off force was for this β value. Changing θ from 30° to 60° , the pull-off force in average decreased from 2.00 ± 0.30 mN to 0.96 ± 0.03 mN for ST-1060 fibers and from 3.75 ± 0.02 mN to 0.31 ± 0.02 mN for ST-1087 fibers.

As can be seen in Figures 2.3a and 2.4a, the larger the pull-off force was, the sharper the trough was. A sharper trough in this case represents a faster crack propagation and quicker detachment. Such detachment is due to relatively uniform stress distribution, which is one of the main reasons resulting in a higher pull-off force. As shown in Figures 2.3c and 2.4d, the crack propagation time t_d at $\theta = 30^\circ$ and $\beta = 1.4$ resulting in the maximal adhesion for ST-1060 fibers fabricated in this study was around 400 msec. However, the crack propagation time at the minimal pull-off force ($\theta = 60^\circ$ and $\beta = 1.1$) was 13.5 sec, approximately 34-fold longer than that of the maximal adhesion. Figures 2.4c and 2.4d illustrate the maximal ($\theta = 30^\circ$ and $\beta = 1.2$, $t_d < 60$ msec) and non-optimal ($\theta = 45^\circ$ and $\beta = 1.3$, $t_d = 2.5$ sec) set of parameters for ST-1087 fibers. As shown in these figures, stiffer fibers made of ST-1087 show higher sensitivity to the shape of wedge angle θ than the softer ST-1060 fibers; approximately 42-fold difference between the maximal and the minimal adhesion.

Figures 2.3b and 2.4b show reaction force for $\theta = 45^\circ$ and $\beta = 1.1 - 1.5$. In this case, the largest pull-off force occurred at $\beta = 1.4$ for ST-1060 ($F_{\text{off}} = 2.04 \pm 0.25$ mN) and $\beta = 1.5$ for ST-1087 ($F_{\text{off}} = 0.66 \pm 0.10$ mN) fibers. Moreover, the larger the β was the smaller the slope of force-displacement curve was. This is mainly due to the decrease in stem diameter and thus its lower stiffness with increasing β . In addition, β has also an impact on stress distribution as illustrated by changes in the sharpness of the troughs in Figures 2.3b and 2.4b [39].

Figures 2.3e and 2.4e illustrate the pull-off force F_{off} for fibers with different β and θ values. We used two samples for each combination of β and θ and performed three measurements on each fiber (90 measurements for each material). The measured pull-off force for all ST-1060 fibers ranged between 2.56 ± 0.06 to 0.87 ± 0.05 mN, and 3.75 ± 0.02 to 0.31 ± 0.04 mN for ST-1087 fibers. As shown in Figures 2.3e and 2.4e, changing β had different effects depending on the tip ending wedge angle and the fiber material. The highest theoretical pull-off force for fibers of different β and θ was estimated at $\beta = 1.1 - 1.2$ and $\theta = 45^\circ$ in the previous work [43]. In our study, on the other hand, the maximum pull-off forces were observed at $\theta = 30^\circ$ and $\beta = 1.4$ for ST-1060 and ST-1087 fibers, respectively. One of the possible reasons for this discrepancy could be the rounded shape at the edge as shown in the inset of Figure 2.1b. Aksak *et al.* predicted that even nano-scale rounded shape of the edge could have a significant impact on the normalized pull-off stress [82]. They also showed that for $\theta = 45^\circ$ there is a lower limit for the pull-off force resulting in a robust adhesion. However, at larger values of θ , there will be a stress singularity at the tip edge resulting in reduced pull-off force [43].

According to Tang *et al.*, normalized pull-off stress $\Phi = \sigma_s/\sigma_0$ (σ_s is the pull-off stress and σ_0 is the theoretical strength of the interface, which could be in between $E/10$ to $E/5$ where E is the elastomeric materials Youngs modulus [82]) of a soft elastic cylindrical fiber that is in contact with a rigid flat surface depends on the dimensionless parameter χ as [83]

$$\chi = \frac{\sigma_0^2 a_s (1 - \nu^2)}{2\pi E \omega_{\text{ad}}}. \quad (2.1)$$

where a_s is the fiber stem radius, ν is the fiber Poissons ratio, and ω_{ad} is the work of adhesion at the fiber-surface interface. In our study, χ was between 2 to 3 for soft ST-1060 fibers and between 20 to 30 for stiff ST-1087 fibers. Figures 2.5a and 2.5b show that soft ST-1060 fibers could achieve higher normalized pull-off stress Φ than stiff ST-1087 fibers over the entire range of different β and θ values. Also, as predicted by Aksak *et al.*, at the existence of the rounded edge shown in the inset of Figure 2.1b, Φ was observed to decrease with increasing χ , as shown in Figure 2.5c [43]. We should note that even though Φ of the stiff fibers is much smaller than that of the soft fibers, the actual pull-off force of stiff fibers was higher than that of the soft fibers due to the high theoretical strength

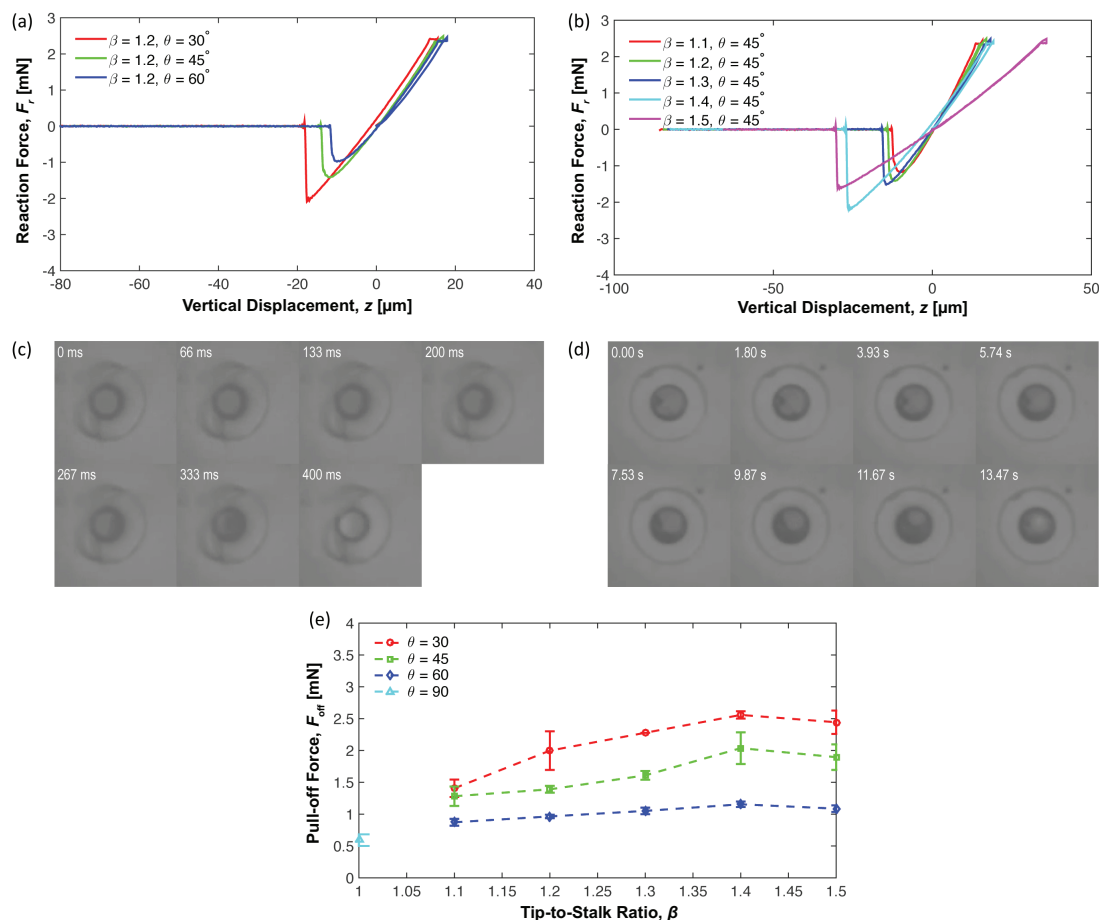


Figure 2.3: Reactive force F_{re} as a function of displacement z for ST-1060 polyurethane fibers at (a) $\beta = 1.1$ and $\theta = 30^\circ - 60^\circ$ and (b) $\theta = 45^\circ$ and $\beta = 1.1 - 1.5$. Snapshots of crack propagation in ST-1060 fibers at (c) $\theta = 45^\circ$ and $\beta = 1.3$ (optimal) and (d) $\theta = 60^\circ$ and $\beta = 1.2$ (non-optimal). Scale bars on (c) and (d) correspond to 100 μm . The first images on both (c) and (d) show the crack initiation and the last images on these parts correspond to full detachment. The entire crack propagation process takes around 400 msec for the optimal set of parameters while it takes around 13.47 sec for the non-optimal case. (e) Experimental pull-off force F_{off} results at different β and θ values. Each data point is an average of six measurements and the error bar indicates the standard deviation. Copyright © 2015 American Chemical Society.

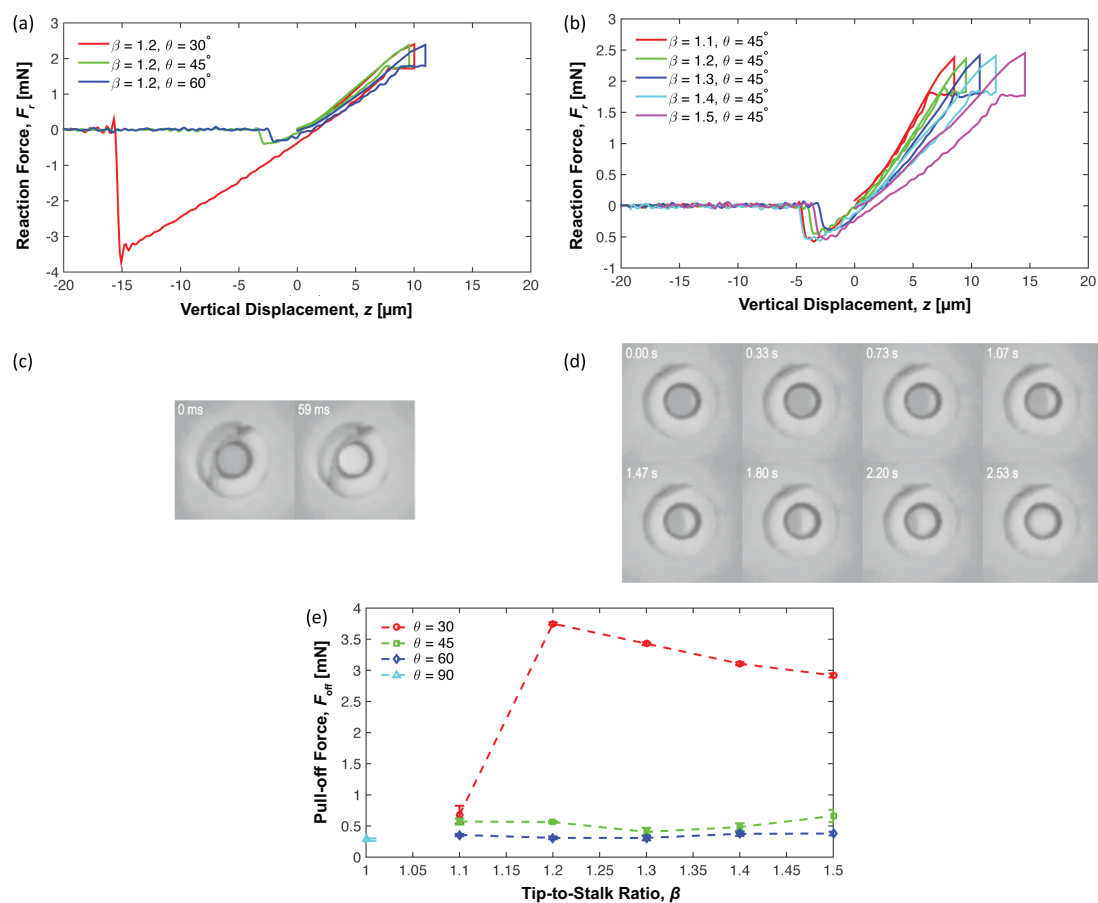


Figure 2.4: Reactive force F_{re} as a function of displacement z for harder ST-1087 polyurethane fibers at (a) $\beta = 1.1$ and $\theta = 30^\circ - 60^\circ$ and (b) $\theta = 45^\circ$ and $\beta = 1.1 - 1.5$. Snapshots of crack propagation in ST-1087 fibers at (c) $\theta = 30^\circ$ and $\beta = 1.2$ (optimal) and (d) $\theta = 45^\circ$ and $\beta = 1.3$ (non-optimal). Scale bars on (c) and (d) correspond to $100 \mu\text{m}$. The first images on both (c) and (d) show the crack initiation and the last images on these parts correspond to full detachment. The entire crack propagation process takes less than 60 msec for the optimal set of parameters while it takes around 2.53 sec for the non-optimal case. (e) Experimental pull-off force F_{off} results at different β and θ values. Each data point is an average of six measurements and the error bar indicates the standard deviation. Copyright © 2015 American Chemical Society.

of the interface σ_0 , implying that the stiffer material could be better for higher adhesion strength if we could more precisely fabricate the optimal tip ending shape of micro-fibers and achieve a full tip contact on the surface.

2.4 Summary

Theoretical studies of optimal adhesion for bio-inspired mushroom-like fibers have shown the significance of tip diameter relative to stalk diameter (β) and the tip-ending wedge angle (θ) [43]. However, there has been no experimental verification of such studies due to issues related to precise fabrication of 3D mushroom-like fiber tip-endings with controlled β and θ . In this study, we used a new 3D nano-lithography technique to fabricate elastomeric mushroom-like fibers with different β and θ values. Conducting measurements of single fiber adhesion, we found changing β at each θ affects the slope of force-displacement curve as a result of changes in fiber stiffness; the higher the β was, the lower the slope of this curve was. Moreover, θ had a significant impact on the sharpness of the troughs on force-displacement curves and thus on crack propagation, which is mainly due to different stress distributions at different values of θ (although β has also an impact on stress distribution by changing the fiber stiffness) [39]. $\theta = 30^\circ$ resulted in the sharpest troughs and fastest crack propagation (for both tested polyurethane materials) due to a relatively uniform stress distribution. In addition, we found maximal pull-off force at $\theta = 30^\circ$ and $\beta = 1.4$ and 1.2 for ST-1060 and ST-1087, respectively. The discrepancy between computational estimation and experimental results could be mainly due to the rounded shape at the edge of micro-fibers as predicted by Aksak *et al* [43].

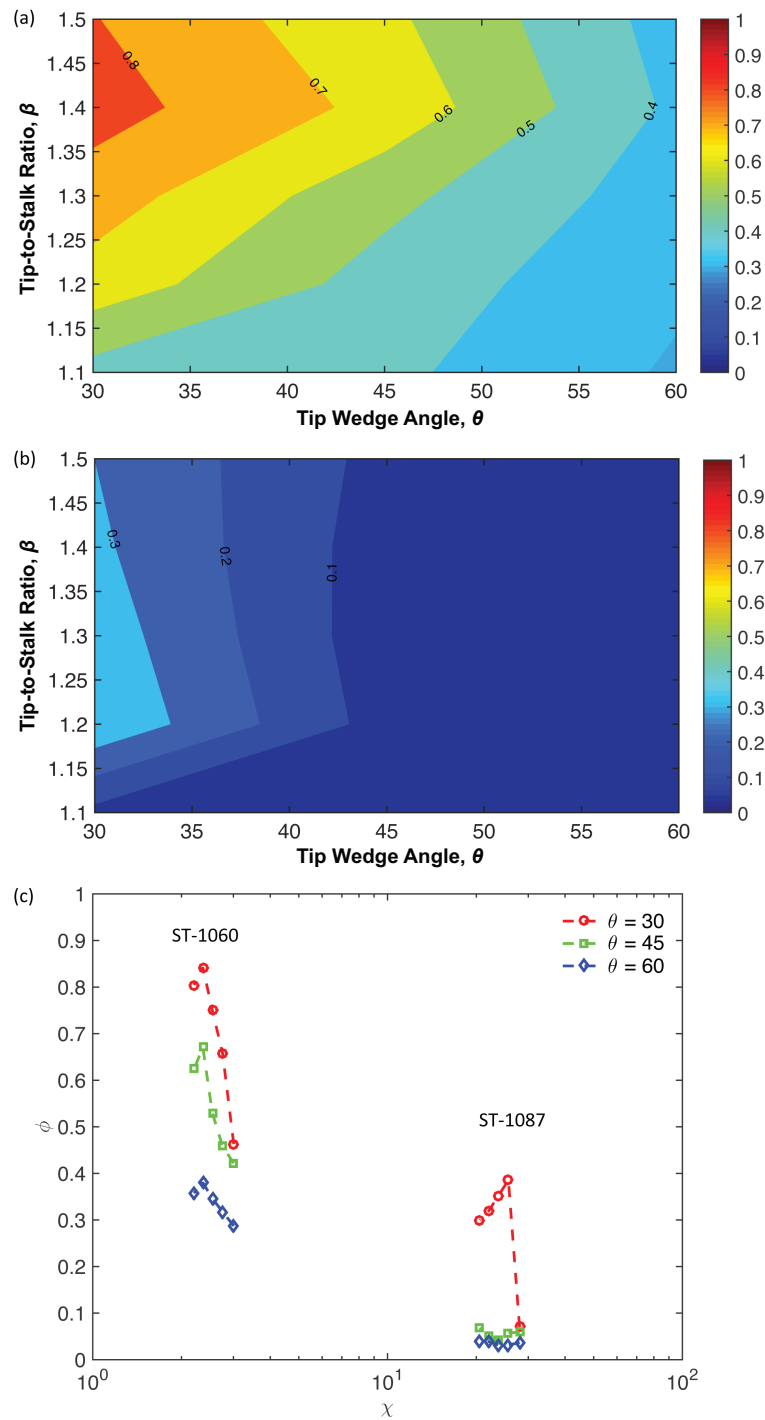


Figure 2.5: Contour plots of normalized experimental pull-off stress Φ values as a function of β and θ for (a) ST-1060 and (b) ST-1087 mushroom-like polyurethane fibers. (c) Φ versus χ for both ST-1060 and ST-1087 fibers at different wedge angles. Copyright © 2015 American Chemical Society.

Chapter 3

Fibrillar Adhesives on a Membrane for Large-scale 3D Surface Grasping

3.1 Introduction

In this chapter, we propose fibrillar adhesives on a membrane (FAM) where a soft, inflatable elastic, thin membrane covered with gecko-inspired micro-fibrillar elastomer adhesives [63, 64] is used for transferring various three-dimensional (3D) objects in size, shape and number. While benefiting from the mushroom-shaped fibrillar adhesives to increase the pull-off forces via the equal load sharing on micro-contacts, the FAM utilizes stretch of the soft membrane during inflation to peel off the micro-fibers in contact by shear force, mimicking the hyper-extension of the geckos when releasing their toes. (This chapter has been reprinted with permission from [79] (Copyright © 2014 IEEE) and [29] (Copyright © 2014 John Wiley & Sons, Inc.).

Various adhesion control methods have been developed for micro-/nano-fibrillar adhesive structures on a rigid backing. M. Yiğit, *et al.* fabricated a slanted single elastomer micro-fiber to make use of its anisotropic stiffness towards bucking direction [28]. The buckling can significantly reduce the adhesion of the micro-fiber, yielding 39 of switching ratio. The angled micro-fiber successfully demonstrated repeatable pick-and-release manipulation of flat micro-objects. H. Jeong, *et al.* fabricated mushroom-shaped slanted nano-hairs

by a specially tuned Deep-Reactive Ion Etching(D-RIE) machine, and used directional adhesion of the nano-hairs for pick-and-release manipulation of a piece of 47.5x37.5 m² glass [20]. W. Bae, *et al.* developed fibrillar structures connected with each others via thin soft bridges, which allows a control of crack propagation on flat surface [61]. Even though these previous methods could manipulate planar objects, problems arise when handling non-planar 3D objects, as the previous controllable adhesion mechanisms rely on mechanical interactions between the gripper and the object, which can be influenced by an object's shape. Therefore, the releasing performance of an adhesion-based gripper must be independent on surface geometries in order to achieve stable pick-and-release manipulation for 3D objects. The inflation-based releasing mechanism proposed in this chapter enables such adhesion control for non-planar surface geometries, by exploiting stretch of soft membrane which can effectively reduce the contact area down to a single fiber-tip contact. The inflation-based peeling also provides an additional degree of freedom in the adhesion control, which is suitable for handling a wide range of 3D objects.

First, in the section of experimental methods 3.2 describes fabrication of the FAM and the experimental setup. Section 3.3 discusses the controllable adhesion mechanism for pick-and-release manipulation based on inflation of the soft backing of the FAM. A full range of manipulatability of the FAM is characterized as the switching ratio in section 3.4 which is the ratio between the maximum and the minimum pull-off forces on a flat glass. Advantages of using the FAM over other possible alternatives (e.g., unstructured membrane or micro-fibers on a rigid backing) in achieving high pull-off forces is also discussed in the section 3.4. Simple analytic models for picking and releasing discussed in section 3.5 will provide basic design rules for optimizing dimensions and performance of the FAM for specific applications. Various pick-and-place manipulations of real-world objects are demonstrated in section 3.6 Finally, conclusions are summarized in Section 3.7.

3.2 Experimental Methods

3.2.1 Fabrication of the FAM

The fibrillar adhesives on a membrane (FAM) has been fabricated with two different polyurethane elastomers for the micro-fibers and the membrane, respectively. The fabrication process of the FAM is shown in Figure 3.1(a). As shown in Figure 3.1(a)-i, the mushroom-shaped fibrillar structures were made out of ST-1060 polyurethane (BJB Enterprises, Inc.), which has been widely used to fabricate fibers and obtains a high work of adhesion of $133 \text{ mJ}\cdot\text{m}^{-2}$ on glass, from a negative mold of the mushroom-shaped fibrillar structures prepared based on the previous work [9]. After removing remnants of the elastomer, another highly deformable elastomer F-25 polyurethane (BJB Enterprises, Inc.), which can endure a large deformation up to 1,100 % of elongation, was coated onto the negative mold at 2,000 rpm for 20 seconds as shown in Figure 3.1(a)-ii. A 3D printed gripper body was brought down to contact with the mold and the uncured elastomers along with the gripper were fully cured for 24 hours at room temperature (Figure 3.1(a)-iii, iv). The fabricated FAM is approximately 16 mm in diameter and 75 μm in thickness (Figure 3.1(b),(c)). The micro-fibers are 105 μm in height, 45 μm in diameter at the stem, and 95 μm in diameter at the mushroom-shaped tip (Figure 3.1(d)).

3.2.2 Experimental Setup

As shown in Figure 3.2, the pull-off force of the FAM are measured by a customized experimental system described in the previous work [28]. Two linear motorized stages for x-axis (462 Series, Newport) and z-axis (MFA-CC, Newport) is attached to an inverted optical microscope (TE200 Eclipse, Nikon) which visualizes the contact area between micro-fibers and a surface. A vertical motion of the FAM is carefully aligned by a two axis customized manual stage and two goniometers for each axis (GON40-U, Newport) prior to a measurement. A high-resolution load cell (GSO-250, GSO-1000, MLP-10, Transducer Techniques) is placed in between the vertical stage and the gripper to sense a change in the pull-off force of the membrane. The gripper is connected with a syringe pump (BS-8000,

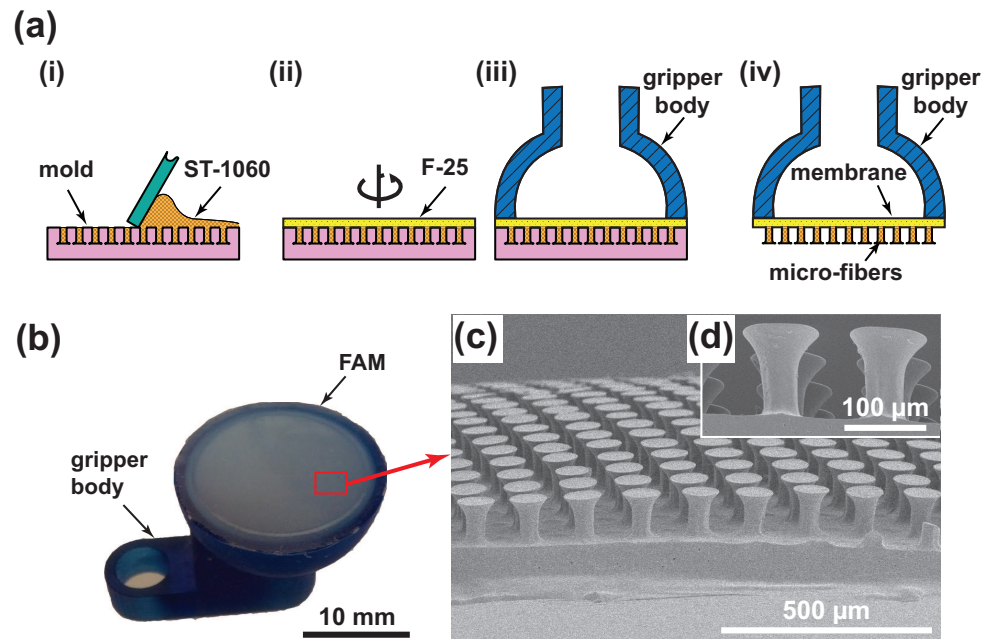


Figure 3.1: (a) Schematics of fabrication process steps of the FAM: (i) molding micro-fibers, (ii) spin-coating the membrane, (iii) mounting the gripper body, and (iv) curing and releasing the FAM, (b) Fabricated FAM on a gripper, (c) Scanning electron microscope (SEM) image of a cross-section of the FAM. (d) SEM image of micro-fibers with mushroom-shaped tip endings. (Copyright © 2014 IEEE)

Braintree Scientific Inc.) through air tubing for applying a preload or inflating the FAM. The measured force in a form of voltage data is processed using customized software on a computer.

3.3 Picking and releasing mechanisms

3.3.1 Picking Mechanism

During the picking task, the gripper is brought down to a target object until the maximum contact area is achieved, as shown in Figure 3.3(a). The tension in the FAM pushes down on the object and applies the preload force F_m . Since the adhesion of the micro-fibers is largely dependent on the applied preload [69], an additional air force F_a is provided to

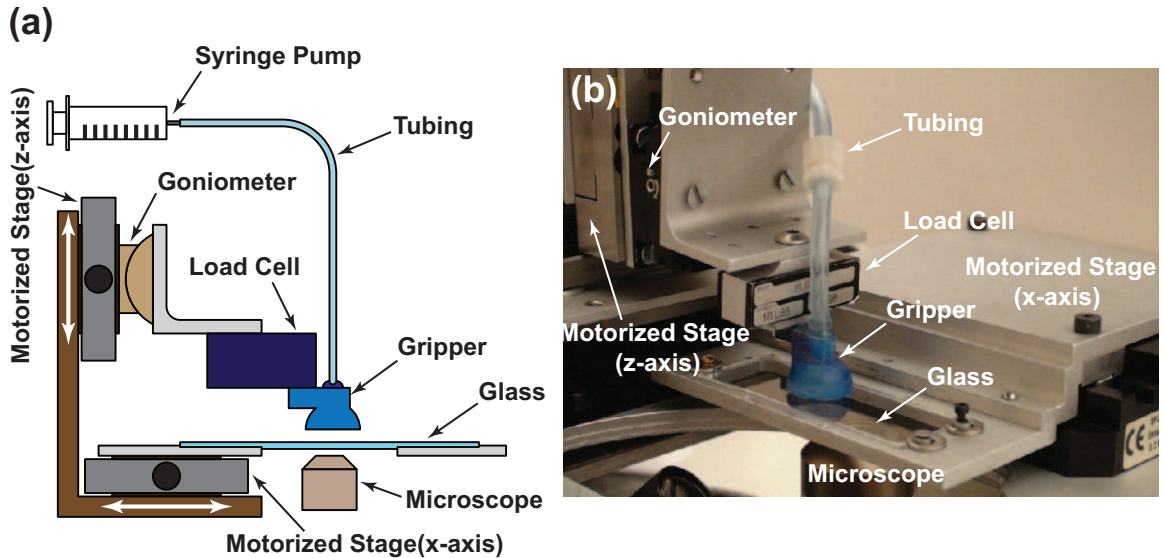


Figure 3.2: Force measurement set-up: (a) schematic figure and (b) photographic image.

further improve the adhesion and adaptation to the target geometry. The applied air force is removed in step (b) before the gripper is pulled away from the stage in step (c). In order to lift the object off from the stage, the picking force F_{pc} , which is defined as the maximum pull-off force, must overcome the sum of the object weight F_w and the adhesion between the part and the stage F_s , such that

$$F_{pc} > F_w + F_s. \quad (3.1)$$

Once the object is lifted up, the holding force F_h is balanced by the object weight F_w as shown in Figure 3.3(d).

3.3.2 Releasing Mechanism

In the releasing task as shown in Figure 3.3(e)-(h), the pull-off force is reduced by controlled inflation of the FAM. From the holding step (d), the object is carried and transferred to the desired target destination and is brought down to the stage in step (e). In step (f), the syringe pump begins to apply an air pressure into the gripper so that the FAM can be inflated while the gripper is retracted. The upward gripper movement creates a space for the FAM to be stretched by the positive air pressure inside the gripper body, resulting in

successive detachments of the micro-fibers in contact. As shown in the steps (e) and (f), the direction and magnitude of the reaction force F_r between the object and the gripper are dependent on retraction speed of the gripper and rate of influx of air. In order to keep the object in contact with the stage, the reaction force F_r between the object and the gripper must be less than the object weight F_w ,

$$F_r < F_w. \quad (3.2)$$

At the releasing step (g), the FAM is fully stretched, and the micro-fibers remaining in contact are stretched. In order to release the object, the reduced pull-off force defined as the releasing force F_{rs} must be smaller than the sum of the object weight F_w and adhesion between the object and the stage F_s ,

$$F_{rs} < F_w + F_s. \quad (3.3)$$

A demonstration of manipulating a 19.1 mm in diameter steel ball and its reaction force profile (F_r) in terms of time (t) are shown in Figure 3.4. The y axis in Figure 3.4 indicates the reaction force between the gripper and the object. For the convenience of understanding, we define positive reaction force to be adhesion at the interface, while negative force to be pushing force onto the stage called preload F_{pre} in this chapter. During the entire manipulation sequences, two plastic holders were placed into the origin and the target destination for holding the sphere shaped ball in a position. Since the plastic holders are not sticky, the adhesion between the object and the stage F_s is neglected during the entire manipulation process.

Starting at the step (a), the FAM is brought down to the object, applying approximately 0.5 N of a preload force by means of the membrane tension in the step (b). Having enough picking force F_{pc} to satisfy the picking condition given by the equation 3.1, the 28 grams steel ball is lifted off from the stage as shown at the step (c). At the holding step (d), the holding force F_h is measured as approximately 0.3N, which is equal to the weight of the target ball F_w . After transferred to a desired destination, the sphere ball is brought down to the stage and made in contact detected by the force sensor as shown in the step (e). During the step (f) and (g), the FAM is inflated with a high positive pressure inside of the

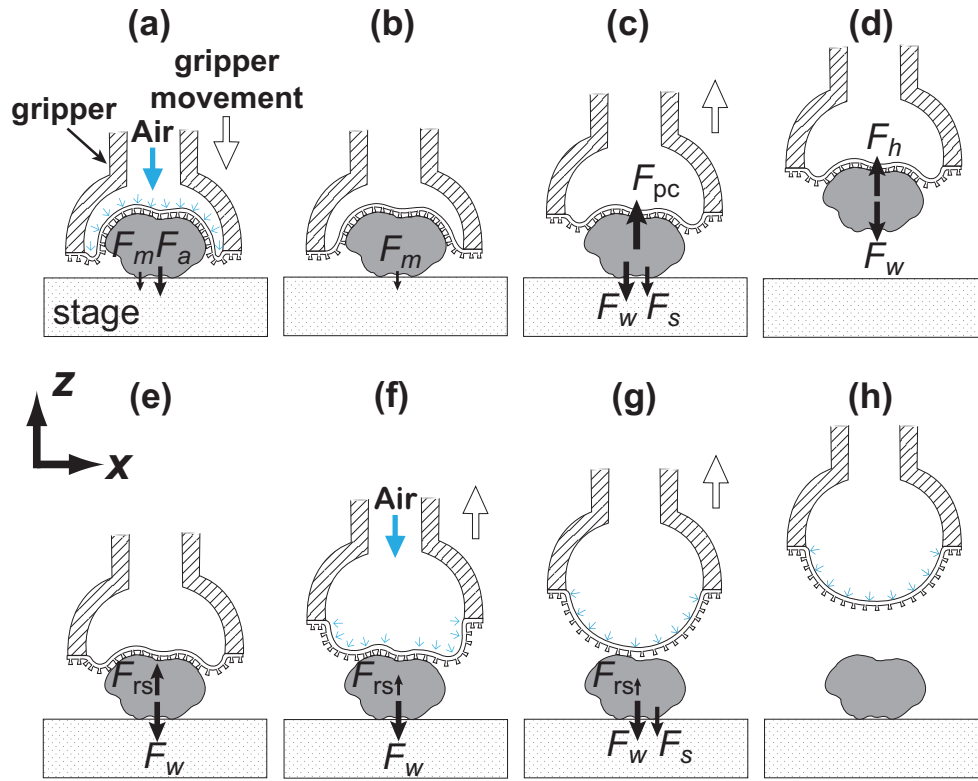


Figure 3.3: Schematics of the pick-and-release manipulation process steps of a soft gripper using the FAM: For picking manipulation, (a) the gripper conforms to the objects 3D shape and applies an additional preload using an internal air force F_a , (b) the internal air force is relaxed, (c) the part is picked from a donor substrate, and (d) the object is carried to a desired position. For releasing, (e) the object is placed onto a receiver substrate, (f) the FAM is inflated by an internal air pressure while the gripper is being moved upward, (g) the micro-fibers are peeled off during the inflation of the membrane and only several fibers stay in contact with the object just before its release, and (h) the object is fully released. (Copyright © 2014 IEEE)

gripper, while the gripper is pulled off from the stage detaching micro-fibers from the ball surface with the stretch of the FAM. As it is discussed in the releasing mechanism 3.3.2, the positive reaction force, which means the pull-off force, is not exceeding the weight of the ball F_w , satisfying the condition described in the Equation 3.2 in order for the object to stay on the stage. At the releasing moment in the step (g), the fully stretched FAM is in a point contact with the steel ball, having approximately 5 mN of the releasing force F_{rs} . Considering the releasing condition given by the equation 3.3, the releasing force F_{rs} of the FAM is smaller than the weight of the ball F_w , placing the ball onto the target destination



(a) ~ (b) (c) (d) (e) (f) (g) (h)

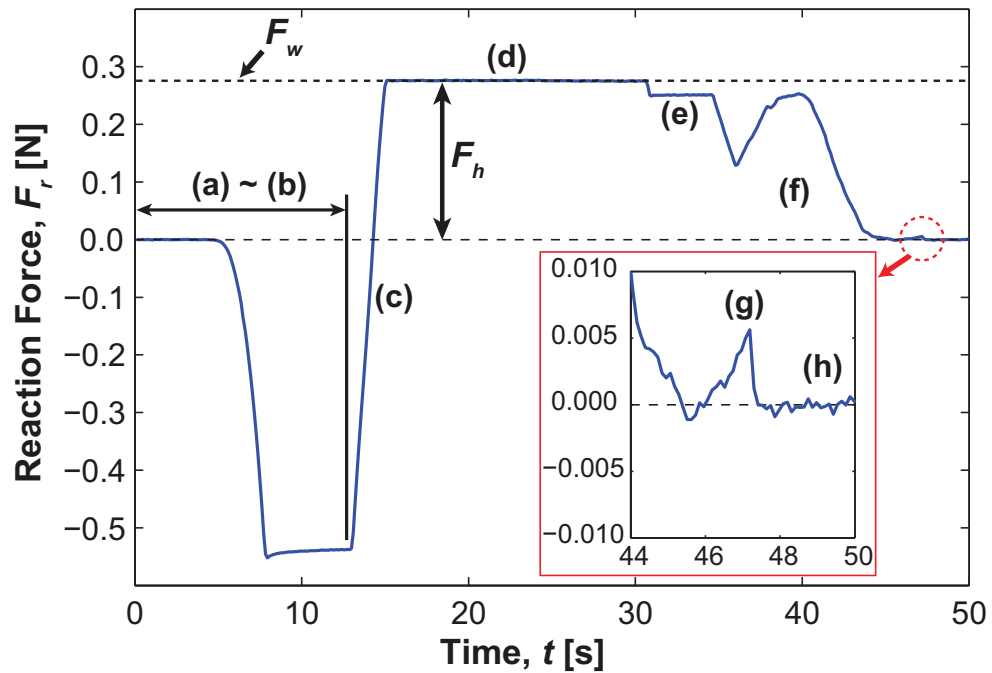


Figure 3.4: reaction force profile of pick-and-release manipulation of a 19.1 mm diameter steel ball: video snapshots in (a)-(d) correspond to the picking mechanism steps 3.3.1 and video snapshots in (e)-(h) correspond to the releasing mechanism steps 3.3.2 described in Figure 3.3. Below plot shows the reaction force data during each pick-and-release manipulation step.

in the step (h).

3.4 Characterization of the FAM

Picking-and-releasing control and yield of the fibrillar adhesives are dependent on the adhesion switching ratio of the gripper-object interface, which is defined as the ratio

between the maximum and minimum producible pull-off forces at the interface. In this section, the maximum pull-off force is defined to be picking force (F_{pe}), while the minimum pull-off force is defined to be releasing force (F_{rs}). According to the picking and releasing conditions given by the Equation 3.1 and 3.3, the fibrillar adhesive on a membrane (FAM) will not be able to pick up an object heavier than the picking force, and not be able to release an object lighter than the releasing force. Therefore, greater switching ratio means that the adhesive gripper can manipulate a wider range of objects in weight. Subsection 3.4.1 describes experimental results of estimation of the switching ratio by measuring the maximum and minimum producible pull-off forces of the FAM on a flat glass surface.

In the subsection 3.4.2, effects of having the soft backing on the pull-off force of fibrillar structures are tested by measuring the picking forces on fixed steel balls of various size, ranging from 1.6 mm to 25.4 mm in diameter. As a control, fibrillar adhesives on a rigid punch (FARP), which has micro-fibers of the same dimension as the FAM on a rigid flat acrylic substrate, and the flat, unstructured membrane mounted to the same 3D printed FAM gripper body have also been examined on the same steel balls.

3.4.1 Estimation of Switching Ratio

Picking Force Measurements

The picking force of the FAM is characterized as follows based on the sequences described in the picking mechanism section 3.3.1; first, the gripper is brought down to a flat glass surface and made in contact. The FAM is pressurized with a positive air pressure to a given preload (F_{pre}) so that micro-fibers can fully be attached to the glass. The applied air pressure inside of the gripper is removed before the gripper is retracted from the glass surface at 0.01 mms^{-1} of retraction speed. The reaction force (F_r) between the FAM and the glass is measured under no applied air pressure during the retraction as shown in Figure 3.5(b). With no applied pressure inside the gripper, the FAM deforms into a truncated cone shape when it is retracted (Figure 3.5(a)-i iii), pulling off the micro-fibers from the edge of the contact area (Figure 3.5(a)-iv vi). Defined as the peel

zone [84], only the micro-fibers at the edge of the contact actively participate in exerting the pull-off force. Within the measured force profile, the maximum reaction force is defined to be the pull-off force for the preload. Since it is reported that the pull-off force of fibrillar structures are dependent on the applied preload [7], the pull-off force with different amount of preloads ranging from 0.03 N to 5.0 N are identified and the maximum pull-off force among the results is characterized as the picking force of the FAM.

To examine the effect of the micro-fibers, the pull-off force of the FAM is also compared to that of a flat, unstructured membrane. To fabricate the flat membrane, F-25 was coated onto a flat silicone rubber at 2,000 rpm for 20 seconds and cured with the same gripper body of the FAM for 24 hours at room temperature as illustrated in Figure 3.1(ii-iv). Figure 3.5(b) shows that the FAM has a higher pull-off force (F_{off}) and larger membrane displacement than that of the flat membrane due to enhanced adhesion by the fibrillar structures. Under the same preload of 0.5 N, the FAM has 0.41 N of pull-off force, about 12 times higher than that of the flat membrane. Figure 3.5(c) shows the pull-off force of the FAM and the flat membrane with different preloads. As reported in the previous work, the pull-off force of the FAM is also dependent on the preload, which could be caused by mechanical bending of the micro-fibers during preload application as shown by photographic images in Figure 3.5(c).

As the preload varied, the FAM pull-off force decreased to 0.26 N at the maximum preload of 5 N, with the picking force of 0.41 N occurring at a preload of approximately 1 N. In contrast, the pull-off force of the flat membrane was almost constant with respect to the preload and was about 0.04 N on average.

Releasing Force Measurements and Estimation of the Switching Ratio

The releasing force of the FAM is characterized based on the sequences described in the releasing mechanism section 3.3.2. Figure 3.6(b) shows the reaction force with respect to each of the experimental step Figure 3.6(b)-i v. After the FAM is brought into contact with a flat glass surface, a high positive air pressure is applied inside of the gripper in step i. A vertical retraction creates room for the FAM to stretch to a spherical shape in step ii

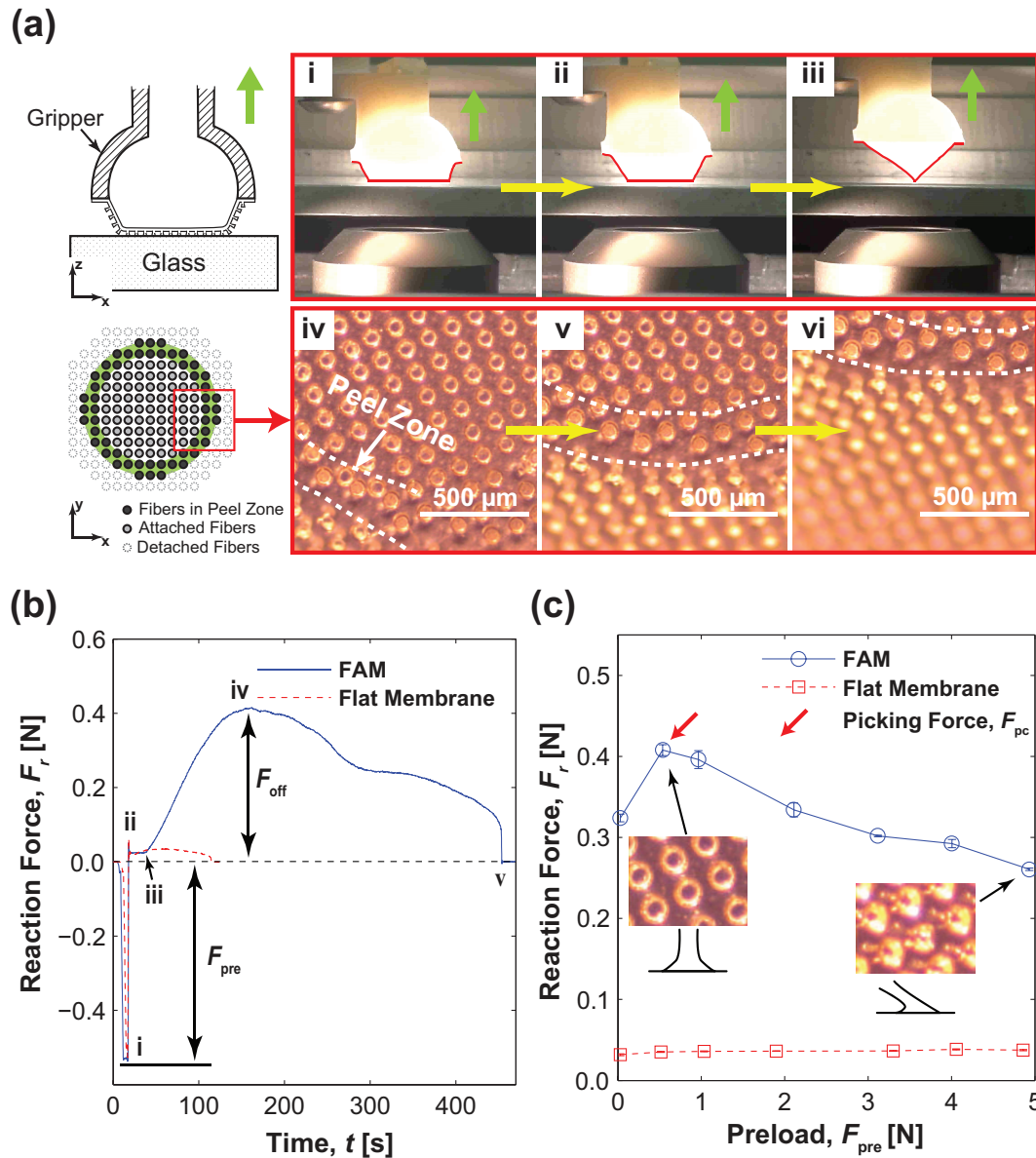


Figure 3.5: Picking force measurement on a flat glass surface: (a) schematic images and snapshots of the FAM retracted from a glass surface with no air pressure (i-iii), and microscopic images at the edge of the contact showing a recession of the peel zone with increasing the gripper movement (iv-vi), (b) reaction force (F_r) of the FAM and the flat membrane without applied air pressure at 0.01 mms^{-1} of retraction speed (i: applying a preload force (F_{pre}), ii: releasing preload, iii: retracting the specimen, iv: reaching to pull-off force, v: pulled off from the surface), and (c) pull-off force of the FAM and the flat membrane on a flat glass surface under the no air pressure in terms of preload. Each data point is the average of three experiments, and the error bar indicates the standard deviation. (Copyright © 2014 John Wiley & Sons, Inc.)

and this stretch peels off the micro-fibers in a concentric direction, resulting in a reduced pull-off force of the FAM in step iii. The gripper was retracted with two different retraction speeds, v_r , to examine the viscoelastic effect of the elastomer micro-fibers [85, 86].

As shown in Figure 3.6(a), micro-fibers on the inflated FAM are pulled off from a surface in different manners from the micro-fibers on the FAM under no air pressure. When the FAM is inflated by a positive air pressure, all of the micro-fibers are stretched in a concentric direction (Figure 3.6(a)-iv,v) due to the spherical deformation of the FAM (Figure 3.6(a)-i iii). Micro-fibers are peeled off with this deformation simultaneously, leaving only a few fibers in contact at the center before the FAM is fully detached (Figure 3.6(a)-vi). The pull-off force of the FAM can be further reduced up to the pull-off force of a single fiber by a sufficient inflation of the FAM with air as it is retracted from a surface. The inflation was quantified in terms of the displacement z_i of the center of the membrane for an applied air pressure. As shown in Figure 3.6(c), the pull-off force by micro-fibers remaining in contact is inversely proportional to the inflation distance of the FAM. The releasing force equal to the pull-off force of a single fiber was approximately 2 mN achieved with 8 mm of inflation distance at 0.01 mms^{-1} as indicated by a dashed green line. The pull-off force is increased with faster retraction speed (0.1 mms^{-1}), requiring increased inflation of the FAM (11 mm of the inflation distance in order to achieve the same single fiber adhesion).

By selecting low surface energy materials or smaller diameter fibers, the releasing force could be further reduced, which would enable micromanipulation of lightweight small parts such as electronic components or particles [17]. When the shape of the deformation of the FAM is assumed to be a perfect spherical shape, the inflation distance can be correlated with the stretch of the FAM λ_m [87] by dividing the expanded area A_m with the original area A_0 as given by

$$\lambda_m = \frac{A_m}{A_0} = \left(\frac{z_i}{R}\right)^2 + 1, \quad (3.4)$$

where R is the radius of the soft gripper, and z_i is the inflation distance at the center of the membrane for the applied air pressure. According to this equation 3.4, the minimum

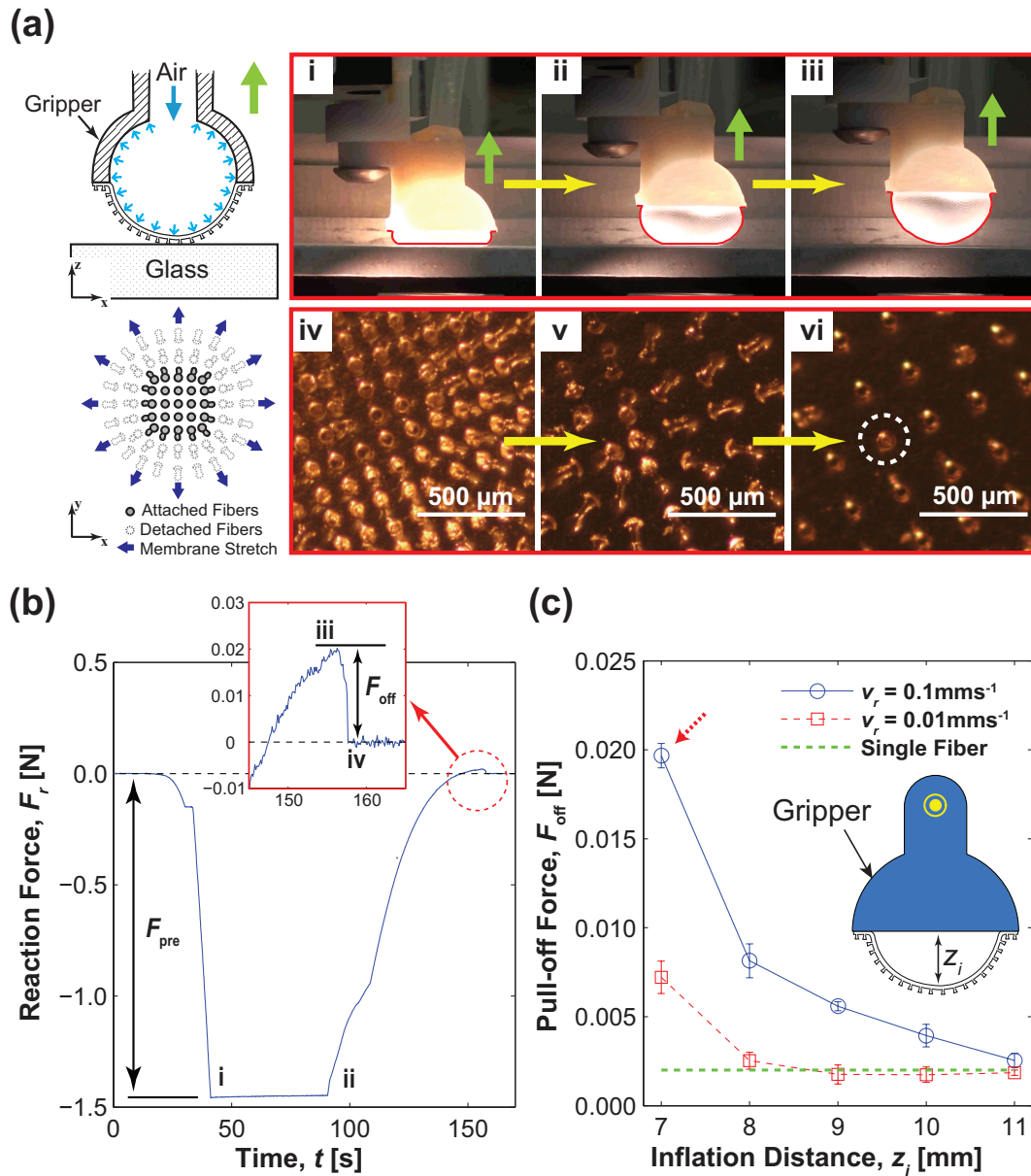


Figure 3.6: Releasing force measurement on a flat glass surface: (a) Schematic images and snapshots of the inflated FAM retracted from a glass surface with a positive air pressure (i-iii), and microscopic images of the contact area showing all fibers are peeled off at once but a single fiber remaining at the center (indicated as a white circle) before the FAM is completely pulled off from the surface (iv-vi), (b) reaction force of the FAM under the positive air pressure corresponding to 7.0 mm of vertical displacement at the center. The retraction speed is 0.1 mms^{-1} (corresponding pull-off force is indicated as a red dashed arrow in Figure 3.6(c)), and (c) pull-off force of the FAM on a flat glass surface under positive air pressure in terms of inflation distance at the center z_i . The green dashed line indicates the minimum pull-off force of a single fiber. Each data point is the average of three experiments, and the error bar indicates the standard deviation. (Copyright © 2014 John Wiley & Sons, Inc.)

stretch of the FAM at the releasing force is approximately 2.3 at 0.01 mms^{-1} and 2.9 at 0.1 mms^{-1} , respectively. The controllable adhesion switching ratio of previous works based on the peeling angle control of the fibrillar structure was up to 39 [28], 10 [60], and 14.8 [61]. With the picking force of 0.41 N (for a flat surface shown in Figure 3.5(c)) and the releasing force of 2 mN for a single fiber (Figure 3.6(c)), however, the switching ratio of the developed device is approximately 204, which is superior to the previous works.

3.4.2 Picking Forces on Non-planar 3D Objects

The advantage of the soft backing of the FAM over the rigid backing for picking up a 3D object is examined by comparing the picking force between the FAM, the FARP, and the flat membrane on different radius of steel balls ranging from 1.6 mm to 25.4 mm in diameter based on the sequences described in the picking mechanism section 3.3.1. First, the specimen is brought to a steel ball fixed onto a flat surface, and a preload within a range from 0.1 N to 2.0 N is applied by the combination of a membrane tension and an air pressure. The reaction force is measured while the specimen is being pulled off from the ball, and the pull-off force on the given size of the steel ball and the preload is determined to be the maximum reaction force. Due to the preload dependency of the fibrillar adhesives, the pull-off forces of the FAM and FARP have been measured at different preloads, and the maximum pull-off force has been identified as the picking force for the given ball size as shown in Figure 3.7(d).

In contrast, since the pull-off force of the flat membrane is independent of the preload as confirmed in Figure 3.5(b), the picking force of the flat membrane measured at only 0.5 N of a preload, which is high enough for the flat membrane to have a full contact with the steel balls. Figure 3.7(a) shows the pull-off forces of the FARP on different ball sizes depending on the preloads. The measured pull-off forces are saturated within zero to 0.12 N of the preloads for all sizes of the steel balls and the maximum pull-off force is approximately 0.12 N on the biggest size of 25.4 mm diameter steel ball. On the other hand, the pull-off forces of the FAM require up to 2.0 N of the preloads at maximum to be saturated on the all tested steel balls as shown in Figure 3.7(b). The maximum pull-off force measured is 0.44

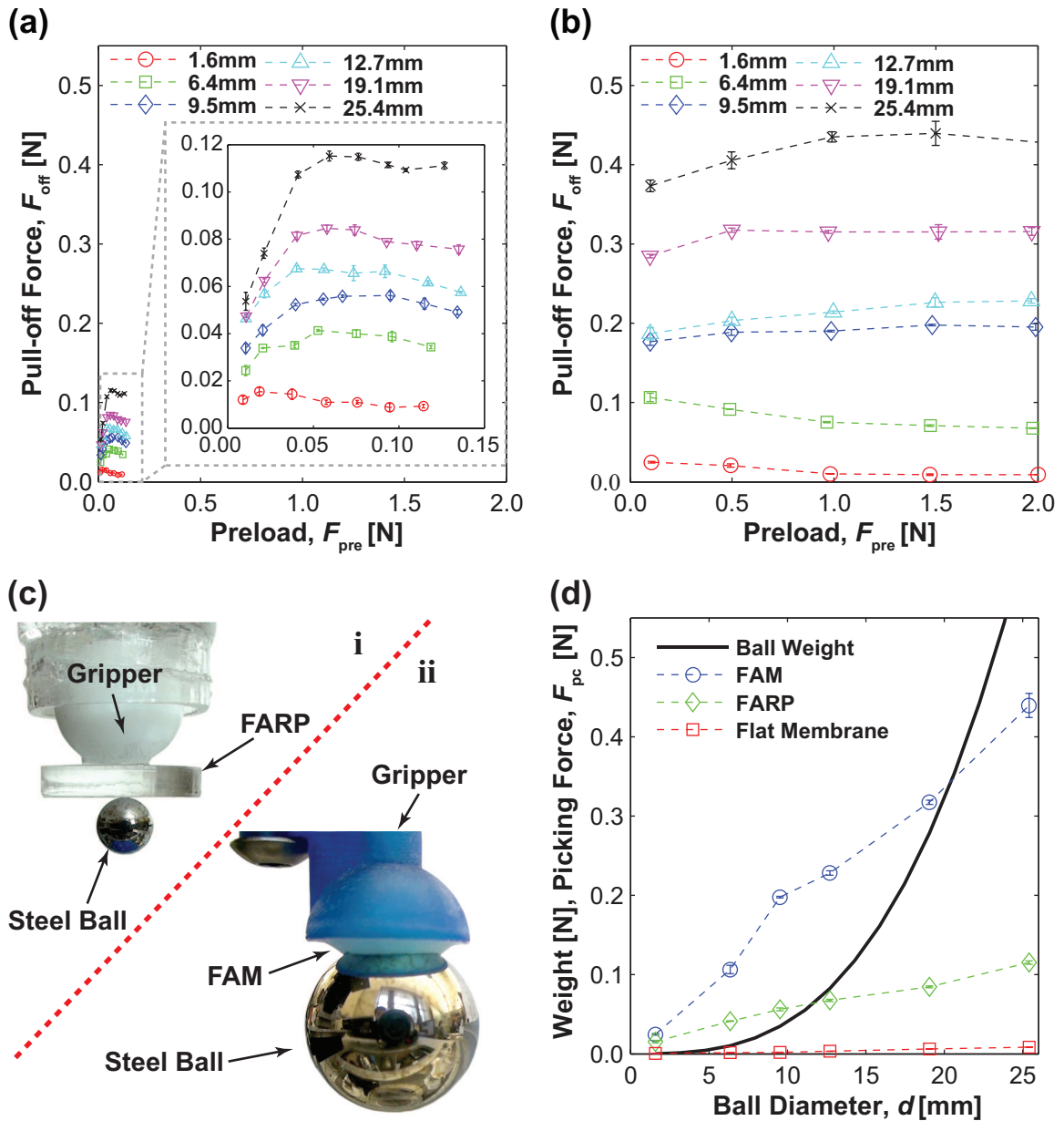


Figure 3.7: Adhesive forces of the FARP and the FAM on various diameters of steel balls ranging from 1.6 mm to 25.4 mm: (a) pull-off forces of the FARP in terms of the applied preload. The dashed box is a magnification of the force plots within 0 to 0.15 N of preload range, (b) pull-off forces of the FAM in terms of the applied preload, (c) photographic images of the FARP holding a 5.5 mm in diameter steel ball (i), and the FAM holding a 19.1 mm diameter steel ball (ii), (d) The picking force comparison of the FAM, FARP, and the flat membrane in terms of ball diameter. Each data point is the average of three experiments, and the error bar indicates the standard deviation. (Copyright © 2014 John Wiley & Sons, Inc.)

N on the 25.4 mm diameter steel ball, approximately 3.7 times higher than that of the FARP.

Figure 3.7(d) shows that the picking force increases with ball size for all of the tested adhesives: FAM, FARP and flat membrane. Based on the results of the FAM and the flat membrane, the enhancement in adhesion using fibrillar adhesives has also been confirmed for curved surfaces. The soft backing layer further improves the adhesion. The FAM has a higher pull-off force than that of the FARP due to the increased contact area with the ball as shown in Figure 3.7(c). Comparing the results with the weight of the balls as indicated by the solid line in Figure 3.7(d), the maximum payload of the FAM is estimated to be 35 grams (0.35 N) corresponding to a 20 mm diameter steel ball, while the FARP can only carry up to 5 grams (0.05 N) corresponding to steel balls less than 12 mm in diameter. The larger contact area of the FAM shows 7 times higher maximum payload than the FARP, which agrees with the concepts of the FAM. For the flat membrane, a ball that is bigger than 3 mm in diameter could not be carried since its weight of 0.13 grams (1.3 mN) is heavier than that of the membranes maximum payload.

3.5 Theoretical Analysis on adhesion of the FAM

In this section, the reaction force (F_r) of the FAM during retraction of the gripper is simulated analytically in order to predict the picking force and the maximum vertical displacement z_{\max} of the membrane before it is completely pulled off from a surface. These two parameters provide crucial information for the FAM gripper design, since the picking force will limit the maximum payload of the gripper, while the maximum vertical displacement can be an indirect measure of the membrane's ability of adapting to an irregular surface. Softer and more stretchable membrane will yield greater vertical displacement, implying that the membrane could potentially adapt to a wider range of irregular 3D objects. On the other hand, the releasing force F_{rs} of the FAM is defined as the minimum pull-off force when it is pulled off from an object with a positive pressure differential inside of the gripper. Inflation of the membrane induced by the air pressure behind the FAM causes stretches effectively detaching micro-fibers from the object surface. The releasing force can be reduced down to a single fiber adhesion by the stretch of the membrane as discussed in the

section 3.4.1. The inflation of the membrane required for achieving the single fiber-tip adhesion is calculated with a simple analytic model.

3.5.1 Picking Force Modeling of the FAM

A cross-section of the flat membrane has been inspected to investigate effect of thickness variance on adhesion quality of the membrane. The flat membrane was casted by a hard polyurethane plastic TC-892 (BJB Enterprises, Inc.), cut it into half using a band sawing machine and polished with a fine sand paper sheet, as shown in Figure 3.8(a). The thickness of the flat membrane was approximately 70~80 μm , same with the thickness of the FAM measured in the section 3.2.1 (Figure 3.8(c)). However, as confirmed in Figure 3.8(b) and (d), the flat membrane had triangular shape of irregular edge at the interface between the membrane and the gripper body, thicker than the regular thin membrane of the center. The size and shape of the irregular edge was slightly different depending on the position on the membrane due to manufacturing imperfection caused by manual fabrication methods, ranging from 500 $\mu\text{m} \times 400 \mu\text{m}$ to 700 $\mu\text{m} \times 500 \mu\text{m}$ in length and thickness. It is found that the adhesion quality of the membrane is largely dependent on the shape and thickness variance of the membrane. A FAM and a flat membrane were brought in contact with a flat glass surface and the edge of contact of those membranes were inspected by the inverted microscope. As shown in Figure 3.8(e) and (f), approximately 400 ~ 500 μm of both FAM and the flat membrane from the edge of the gripper body, which is equal to the length of the irregular edge, was not able to achieve a good engagement with the glass surface no matter how big preload is applied. In order to get an accurate analytical prediction of the reaction force between a membrane and an object, the membrane is discretized into two regimes and analytic models are developed separately; regime I is the edge of the membrane with irregular shape, and regime II is the rest of regular thin membrane. Based on the inspection of the cross-section of the FAM and filtered images at the edge of contact of both FAM and the flat membrane shown in Figure 3.8, two assumptions are made in the following analytic modeling for regime I,

1. Regime I is thicker than regime II and has irregular shape.
2. Regime I cannot adhere to a substrate.

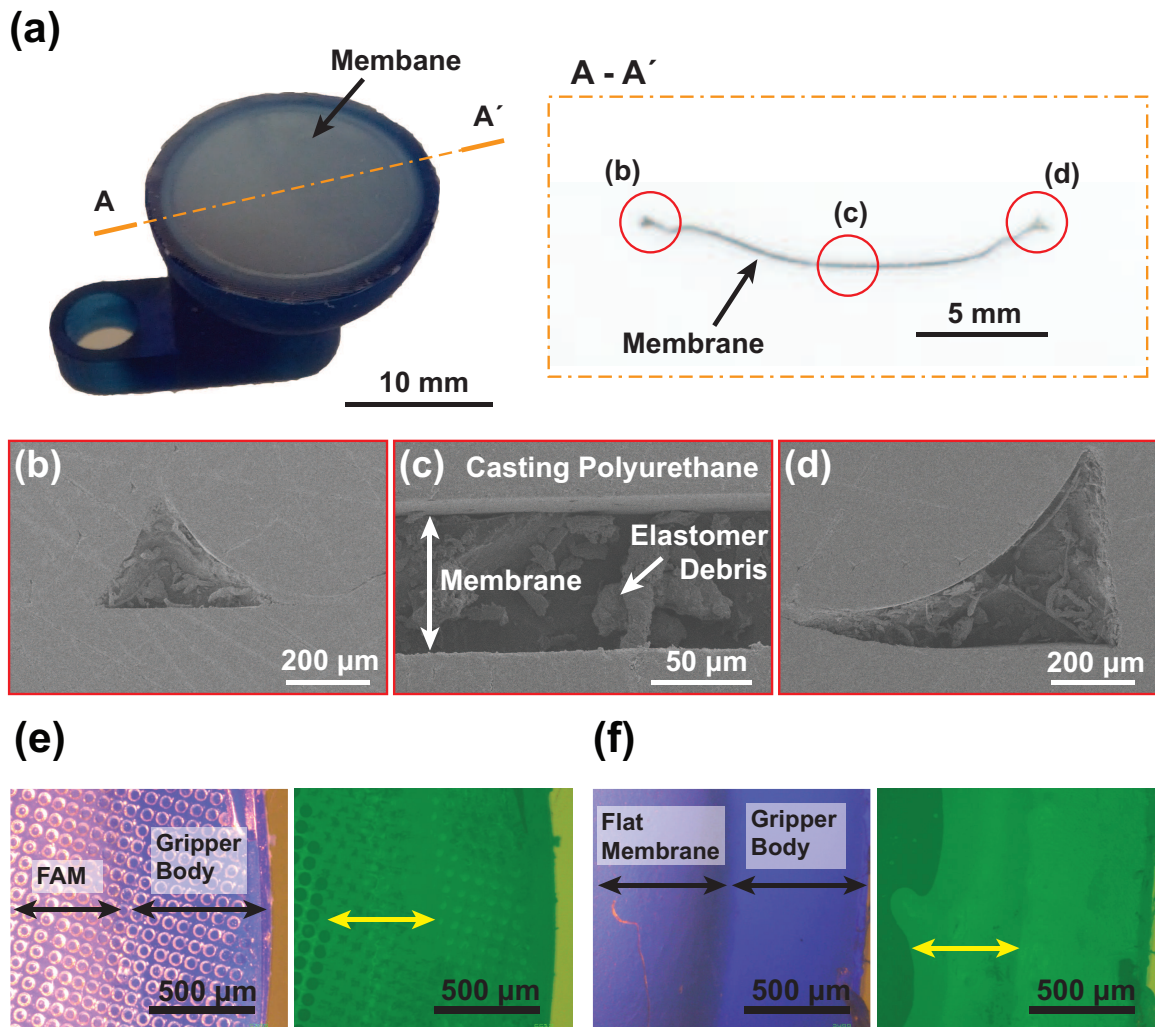


Figure 3.8: Contact condition of a membrane depending on the thickness profile: (a) photographic image of cross-section of the flat membrane, (b) SEM image of the left edge of the flat membrane, (c) SEM image of the center of the flat membrane, (d) SEM image of the right edge of the flat membrane, (e) optical microscopic images of the edge of the FAM (left: unfiltered, right: filtered) and (f) optical microscopic images of the edge of the flat membrane (left: unfiltered, right: filtered).

As shown in Figure 3.9(i), at the initial stage of retraction of the gripper, the regime I begins to deform downwards toward the glass surface while the regime II is fixed onto the flat substrate due to adhesion of the membrane. Elastic restoring force of the regime I keeps increasing with the vertical displacement of the gripper until it overcomes the pull-off force of the regime II. Once the restoring force of the regime I becomes bigger than the

pull-off force of the regime II, the regime II starts peeled off from the surface, deforming into a truncated corn shape as discussed in the section 3.4.1 (3.9(ii)). The total vertical displacement of the gripper z is given as a sum of the vertical displacement of the regime I z_I and the vertical displacement of the regime II z_{II} ,

$$z = z_I + z_{II}. \quad (3.5)$$

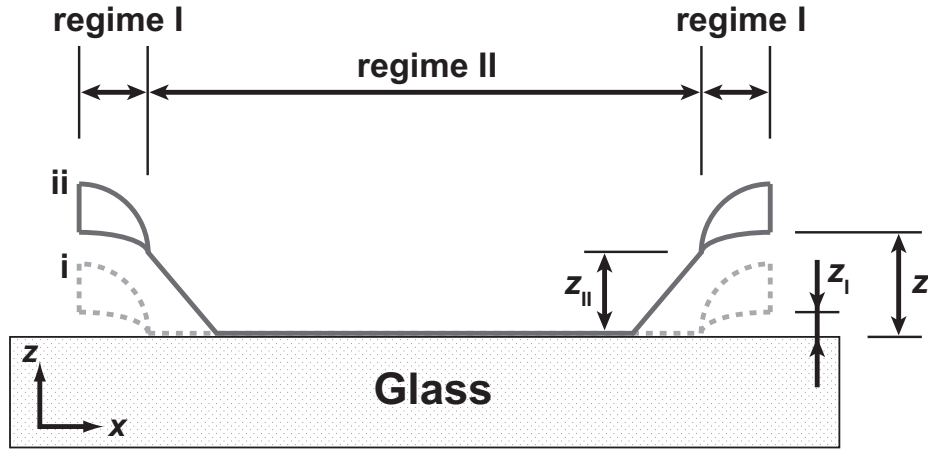


Figure 3.9: Schematic of regime I and regime II during retraction of the gripper: (i) the initial stage of retraction of the gripper whose vertical displacement is dominated by deformation of the regime I, (ii) after the initial stage of the retraction of the gripper whose vertical displacement is dominated by detachment of the regime II.

Modeling of the Regime I

Here, we estimate the vertical displacement and reaction force of the FAM based on linear elastic beam bending, assuming the regime II is in full contact. The FAM is assumed to have the same shape of the edge with that of the flat membrane shown in Figure 3.10(a). At a free standing mode of the membrane, as shown in Figure 3.10(b), the regime I of the FAM is simplified to be a triangular shape with linear decrease in thickness $h(x)$ which is given by,

$$h(x) = \frac{h_0 - h_e}{l_e}x + h_e, \quad (3.6)$$

where h_0 , h_e , and l_e are thickness of the regime II, thickness of the regime I at the interface

on the gripper body, and length of the regime I, respectively. When the gripper is retracted from the glass surface, the regime I is bent toward the glass substrate since the regime II is pinned by the adhesion of the micro-fibers. Deformed configuration of the regime I experiencing the reaction force at the boundary between two regimes is shown in Figure 3.10(c). The reaction force induces a bending moment $M(x)$ around the neutral axis of the regime I indicated by a single-dashed line,

$$M(x) = F_r (l_e - x) = \int_0^h 2\pi (R_0 - x) z \sigma_{11}(x) dz, \quad (3.7)$$

where σ_{11} is the principal stress of the regime I. Assuming the principal stress to be a linear function of thickness z ,

$$\sigma_{11}(z) = C_0 + C_1 z. \quad (3.8)$$

C_0 and C_1 are unknown constants. According to the boundary condition shown in Figure 3.10(c), the principal stress has to be symmetric about the neutral axis and be maximized at the upper and lower boundary,

$$\sigma_{11}\left(\frac{h}{2}\right) = 0, \quad \sigma_{11}(0) = -\sigma_{\max}, \quad \text{and} \quad \sigma_{11}(h) = \sigma_{\max}. \quad (3.9)$$

where σ_{\max} is the maximum value of the principal stress at both boundaries. Substituting the boundary conditions 3.9 into Equation 3.8, the principal stress is given by,

$$\sigma_{11}(z) = \sigma_{\max} \left(\frac{2z}{h} - 1 \right). \quad (3.10)$$

The maximum principal stress σ_{\max} can be expressed in terms of x , z , and F_r by substituting Equation 3.10 into Equation 3.7,

$$\sigma_{\max} = \frac{3F_r (l_e - x)}{\pi h^2 (R_0 - x)}. \quad (3.11)$$

By substituting Equation 3.11 to Equation 3.10, the principal stress σ_{11} can be given by,

$$\sigma_{11} = \frac{6F_r (l_e - x)}{\pi h^3 (R_0 - x)} \left(z - \frac{h}{2} \right). \quad (3.12)$$

Assuming the linear relationship between stress and strain of the regime I based on Hook's Law, strain of the regime I in the principal direction is given by,

$$\epsilon_{11} = \frac{6F_r(l_e - x)}{\pi E_m h^3 (R_0 - x)} \left(z - \frac{h}{2} \right), \quad (3.13)$$

where E_m is Young's modulus of the FAM's membrane. Curvature of the bending κ has a relationship with the principal strain ϵ_{11} ,

$$\kappa = \frac{\epsilon_{11}}{z - \frac{h}{2}}. \quad (3.14)$$

Therefore, the curvature of the bending κ can be only a function of x direction as given by,

$$\kappa = \frac{6F_r(l_e - x)}{\pi E_m h^3 (R_0 - x)}. \quad (3.15)$$

By taking a double integral of Equation 3.15, the vertical displacement of the regime I z_1 can be calculated by,

$$z_1 = \iint \kappa(x) dx = \iint \frac{6F_r(l_e - x)}{\pi E_m h^3 (R_0 - x)} dx, \quad (3.16)$$

where the boundary conditions are given by,

$$z_1(0) = 0, \quad \dot{z}_1(0) = 0. \quad (3.17)$$

The measured values of all parameters of the fabricated FAM are given in Table 3.1. As shown in Figure 3.10(d), the reaction force of the regime I on the FAM is linearly increased depending on the vertical displacement of the gripper. According to the physical geometry of the regime I inspected by the SEM in Figure 3.10(a), the slope of increase in the reaction force in terms of the vertical displacement is approximately 0.5 Nmm^{-1} , which shows a good agreement with the experimental verification Figure 3.12. Figure 3.10(d) also shows other calculations for the reaction force for different sizes of regime I ranging from $140 \mu\text{m} \times 100 \mu\text{m}$ to $700 \mu\text{m} \times 500 \mu\text{m}$ in length and thickness. The slope of the reaction force depending on the vertical displacement is increased with smaller size of the regime I; the slope varies from 1.40 Nmm^{-1} at the size of $140 \mu\text{m} \times 100 \mu\text{m}$ to 0.49 Nmm^{-1} at the size of $700 \mu\text{m} \times 500 \mu\text{m}$. Without the regime I, the slope can be further increased up to 5.10 Nmm^{-1} as shown in Figure 3.11(c) and (d) in the section 3.5.1, which is approximately 10 times greater than that of the fabricated FAM.

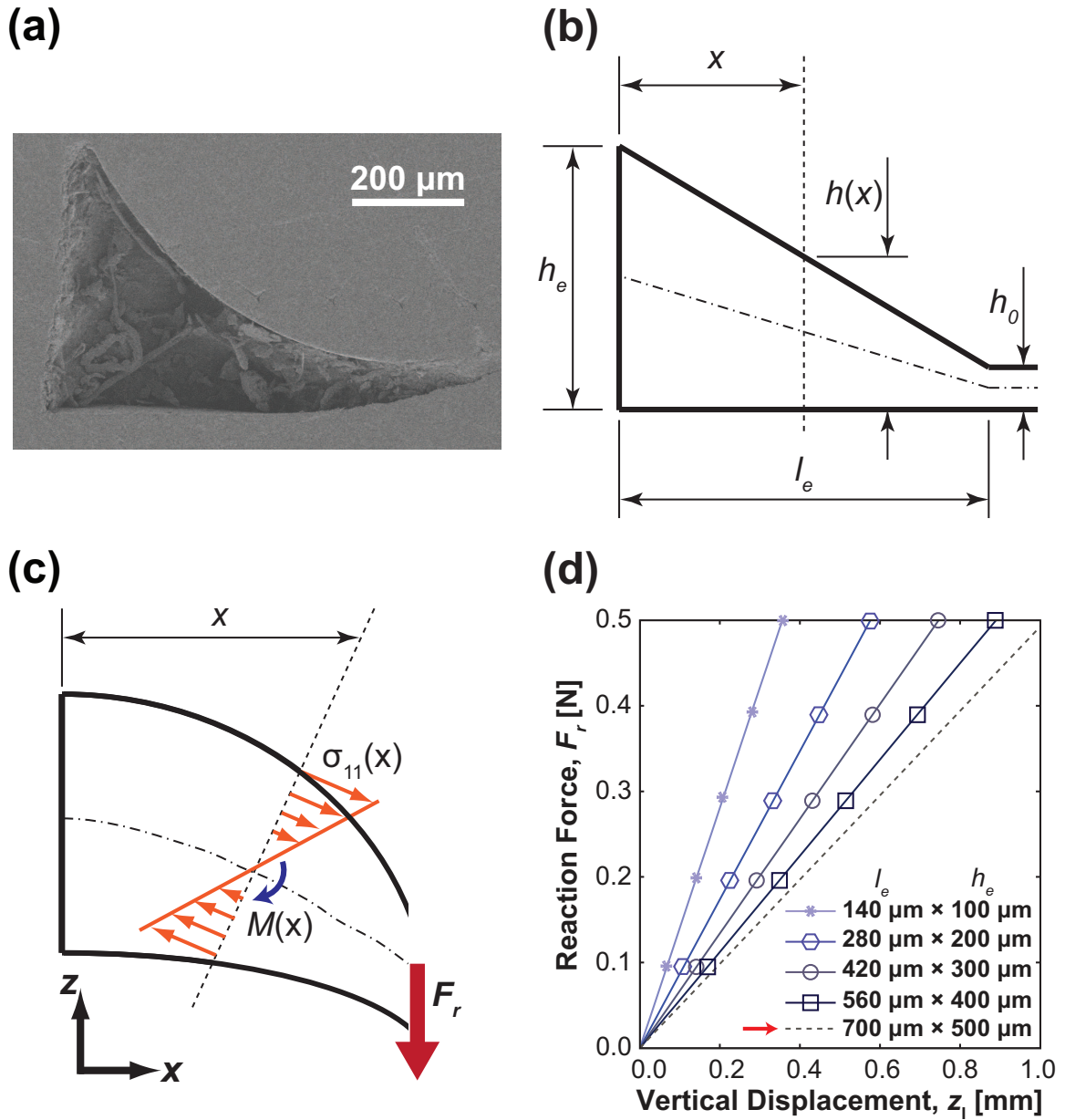


Figure 3.10: Analytical modeling of picking force of the FAM at regime I: (a) SEM image of cross-section of regime I of the flat membrane, (b) schematic of undeformed regime I simplified to be a triangular cross-section, (c) schematic of deformed regime I under the reaction force due to adhesion of regime II, and (d) analytic solutions of vertical displacement z_1 depending on the reaction force. Analytical estimations for the fabricated FAM were marked with a red arrow in (d).

Table 3.1: Design Parameters of the FAM

Fiber Tip Diameter, a_t	95 [μm]
Fiber Stem Diameter, a_s	45 [μm]
Fiber Length, l_0	105 [μm]
Stem Length, l_s	75 [μm]
Fiber Pitch, p_0	120 [μm]
Fiber Density, ρ_f	6.94×10^7 [fibers \cdot m^{-2}]
Membrane Radius, R_0	8 [mm]
Membrane Thickness, h_0	75 [μm]
Edge Length of Membrane Regime I, l_e	700 [μm]
Edge Thickness of Membrane Regime I, h_e	500 [μm]
Young's Modulus of Membrane (F-25), E_m	0.36 [MPa]
Young's Modulus of Micro-fibers (ST-1060), E_f	2.9 [MPa]
Surface Energy on glass (F-25), $\omega_s _{F-25}$	71 [$\text{mJ} \cdot \text{m}^{-2}$]
Surface Energy on glass (ST-1060), $\omega_s _{ST-1060}$	133 [$\text{mJ} \cdot \text{m}^{-2}$]
Area Fraction of Micro-fibers, η_f	0.492

Modeling of the Regime II

As it is discussed in the previous section 3.5.1, the FAM in regime II is considered to be a perfectly uniform and thin membrane. The shape of deformation of the regime II membrane during retraction of the gripper is shown in Figure 3.11(a) and simplified as a truncated cone shape as shown in Figure 3.11(b). The stretch of the membrane in each circumferential λ_ρ , meridional λ_φ and thickness direction λ_t are respectively given as

$$\lambda_\rho = \frac{s}{\rho} = \frac{\sqrt{z^2 + (R_0 - r)^2}}{(R_0 - r)}, \lambda_\varphi = 1, \lambda_t = \frac{1}{\lambda_\rho \lambda_\varphi} = \frac{(R_0 - r)}{\sqrt{z^2 + (R_0 - r)^2}}. \quad (3.18)$$

where R_0 is the gripper radius, r is the contact radius, and z is the vertical displacement. The reaction force with respect to the vertical displacement z from the substrate can be calculated by the principle of minimum potential energy. The Neo-Hookean model is adopted for the strain energy density function $W_o(r, z)$, which is given as

$$W_o(r, z) = \frac{E_m}{6} (\lambda_\rho^2 + \lambda_\varphi^2 + \lambda_t^2 - 3), \quad (3.19)$$

where E_m is the Young's modulus of the FAM's membrane, assuming small deformations. A critical contact radius r_c , the radius at which detachment is initiated for a given deformation of the membrane induced by the vertical displacement z , can be calculated as a point where the first partial derivative of the sum of elastic and adhesion energy of the FAM becomes zero, satisfying Equation 3.20,

$$\left[\frac{\partial \Pi}{\partial r} \right]_z = 0, \text{ where } \Pi(r, z) = \pi (R_0^2 - r^2) h_0 W_o(r, z) - \pi r^2 \omega_{\text{ad}}, \quad (3.20)$$

ω_{ad} is the effective work of adhesion, and h_0 is the thickness of the FAM's membrane. The new total potential energy $\hat{\Pi}(z)$ evaluated at the critical contact radius r_c gives the reaction force (F_r) of the FAM at a certain vertical displacement (z^*),

$$F_r(z^*) = \left[\frac{\partial \hat{\Pi}}{\partial z} \right]_{z=z^*}, \text{ where } \hat{\Pi}(z) = \Pi(r_c, z). \quad (3.21)$$

In order to calculate profile of the reaction force using Equation 3.21, the effective work of adhesion at the interface between the gripper and the object must be measured, or analytically estimated. The effective work of adhesion can be approximated as follow :

$$\omega_{\text{ad}} = \eta_f (\omega_s + \omega_e), \quad (3.22)$$

where η_f is the fraction of the fiber tip area to the total area of the FAM's membrane, ω_s is surface energy for creating another surface from the membrane and glass boundary, and ω_e is the work done by the elastic deformation of a fiber. To estimate the work done by a fiber, it is assumed that most of the deformation of the mushroom-shaped fiber occurs at the stem. According to a cylindrical deformation defined by the Neo-Hookean model, the critical stretch of the fiber, λ_c , to cause detachment can be calculated from the condition of

$$\lambda^3 - \frac{(3f_c)}{E_f \pi r_s^2} \lambda^2 - 1 = 0. \quad (3.23)$$

where E_f is the Young's modulus of the micro-fiber, f_c is the critical force for a fiber measured experimentally, and r_s is the radius of the fiber stem, which is $a_s/2$. As a result, the work done by a fiber can be estimated to be the work done by the critical force to achieve the critical stretch, which is given as

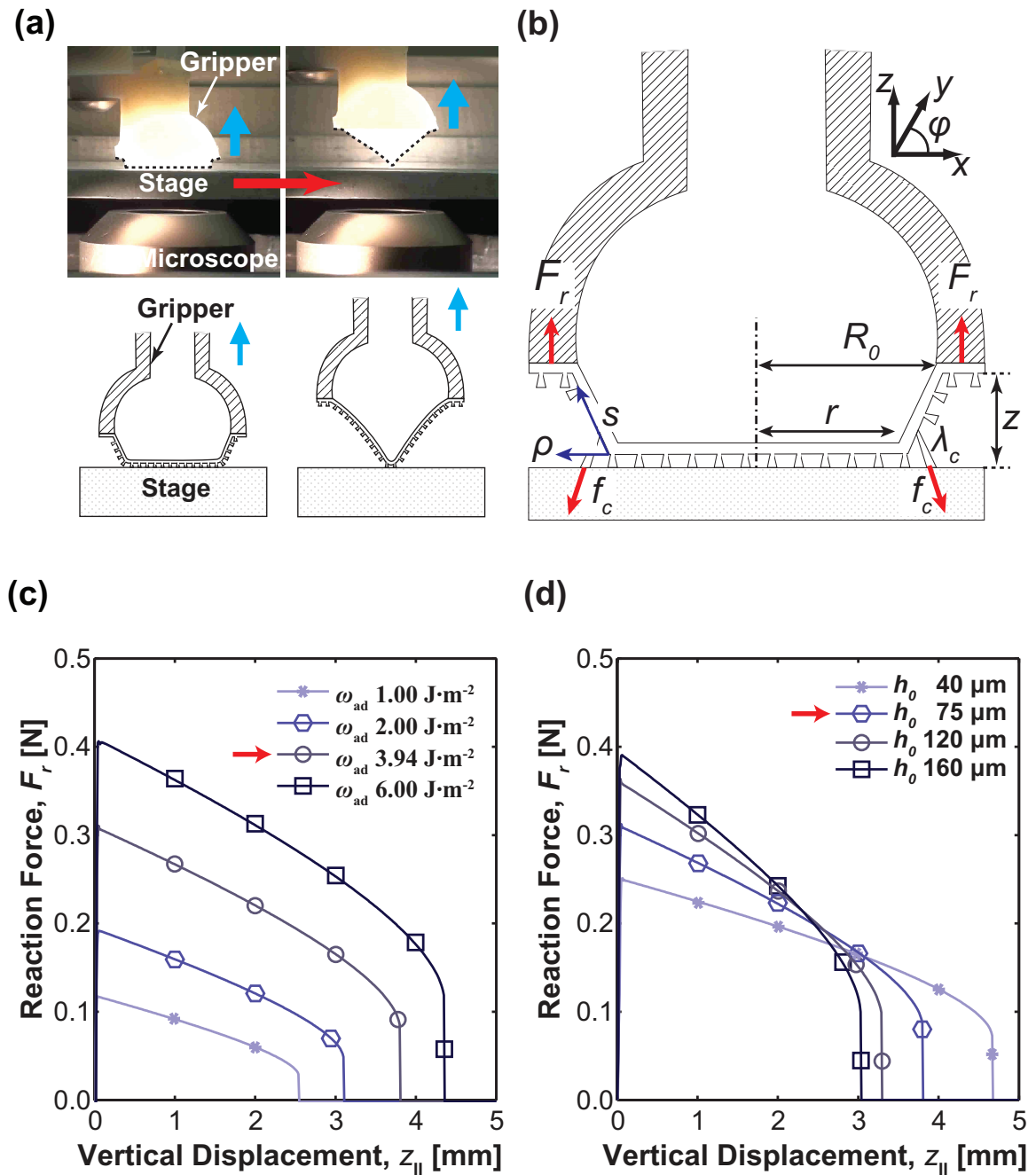


Figure 3.11: Analytical modeling of picking force of the FAM at regime II: (a) Shape of deformation of the FAM while it is retracted from a flat surface under no air pressure, (b) Definition of parameters for the modeling, (c) reaction force F_r depending on vertical displacement z for different work of adhesions ω_{ad} , (d) reaction force F_r depending on vertical displacement z for different membrane thicknesses h_0 . Analytical estimations for the fabricated FAM were marked with red arrows in (c) and (d). (Copyright © 2014 IEEE)

$$\omega_e = \frac{E_f r_s^2 l_s}{3r_t^2} \left(\frac{\lambda_c^2}{2} + \frac{1}{\lambda_c} - \frac{3}{2} \right), \quad (3.24)$$

where l_s is the length of the stem and r_t is the radius of the fiber tip, which is $a_t/2$.

The critical stretch of a fiber, which is a ratio between the fibers initial and final length during its pull-off, is estimated to be 1.66 by Equation 3.23 and the work done by the fiber is $7.87 \text{ J}\cdot\text{m}^2$ by Equation 3.24. The effective work of adhesion of fibrillar adhesives on the FAM is calculated to be $3.94 \text{ J}\cdot\text{m}^{-2}$ by Equation 3.22, significantly greater than the work done by a flat, unstructured surface ω_s . As shown in Figure 3.11(c)-(d), without considering effects of the irregular shape of the regime I, the reaction force rapidly increases with the vertical displacement z and reaches to the pull-off force. After reaching the pull-off force, the reaction force starts decreasing with respect to the vertical displacement. At some point, the FAM is suddenly detached from the surface when the adhesion energy on the boundary can no longer support the reaction force. Here, the reaction force becomes zero and the corresponding vertical displacement is defined as the critical displacement. As shown in Figure 3.11(c), the pull-off force and the critical displacement for detachment increase with the effective work of adhesion. As previously discussed, the effective work of adhesion of the FAM is approximately $4 \text{ J}\cdot\text{m}^2$ due to the effect of the fibrillar structures, and the picking force is estimated to be approximately 0.31 N . Figure 3.11(d) shows the effect of different thicknesses; an increase in the membrane thickness results in a higher pull-off force, while the critical displacement is decreased. A thicker membrane cannot achieve larger displacements than a thinner membrane and the adhesion energy is the same for thick and thin membranes since it is only dependent on the contact radius. Therefore, a thicker membrane would have a higher adhesive force in order to conserve the adhesion energy with the elastic work done by the membrane.

Verification of Picking Force Modeling

Three FAMs with same physical dimensions are fabricated to verify the developed analytic models for regime I and regime II, and tested to measure the reaction force profile

following the experimental procedures introduced in the picking mechanism section 3.3.1 as shown in Figure 3.12(a). The reaction forces for the three FAMs have been measured under the same 1 N of preload force which has been verified as an optimal preload for exerting the picking force in the picking force characterization section 3.4.1.

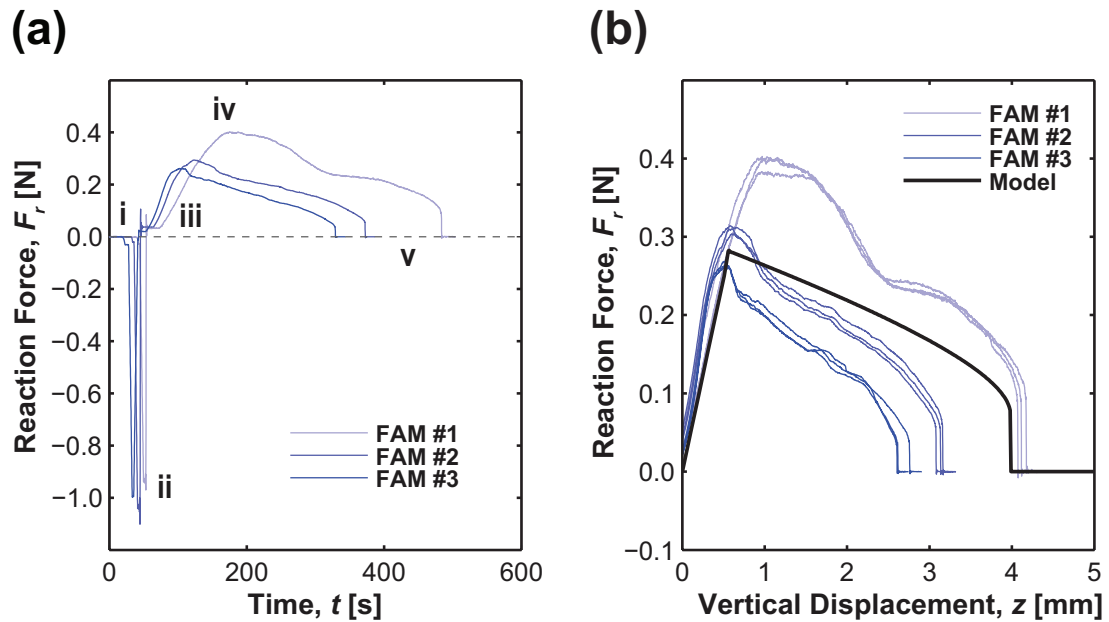


Figure 3.12: Picking force measurements and verification of the developed analytic model: (a) reaction force profile of three FAMs in terms of time (i:contacting with a surface, ii: applying a preload, iii: retracting, iv: achieving the maximum reaction force, and v: pulled off from the surface) and (b) the reaction force profile of three FAMs F_r depending on vertical displacement z and analytical solution (indicated by solid line). all three FAMs are tested three times per each samples.

Figure 3.12(b) shows the results of three times of the reaction force profile measurement per each samples depending on the vertical displacement z . Even though the three specimens were fabricated with same design of micro-fibers and membrane, the picking force of the three FAMs were varied ranging from 0.26 N to 0.41 N. The average picking force of the three FAMs is approximately 0.32 N, which is closed to that of the analytically estimated solution of 0.28 N. Also, as shown in Figure 3.12(b), the initial slope of increase in the picking force at the regime I has a good agreement with the analytical estimation.

However, estimation of the maximum vertical displacement z_{\max} before the membrane is fully detached is not matched with the experimental results. After reached to the maximum positive value, the reaction force of the FAM decreased with a ratio faster than expected by the analytic model. Various factors can cause the difference between the above theoretical estimation and the experimental results; simplification of the deformation shape, measuring error of the physical parameters such as thickness of the membrane, Youngs modulus, errors in estimating the effective work of adhesion of the membrane, etc. Especially, the Neo-Hookean solid could not calculate the saddle shape of the reaction force profile. The saddle shape becomes greater when the pull-off force increases. The Odgen Model which uses higher order term of stretches might be able to calculate the saddle shape.

3.5.2 Releasing Force Modeling of the FAM

The releasing force F_{rs} is defined as the minimum pull-off force reduced by the inflation of the FAM's membrane. As we discussed in the section 3.4.1, the releasing force of the membrane will be equal to the pull-off force of a single fiber f_c and it can be achieved by inflating the FAM with air as it is retracted from a surface. The inflation shape of the membrane with a small contact area before it is pulled off can be approximated as spherical, whose radius R can be given as a function of an inflation distance z_i as shown in Fig. 5(a),

$$R(z_i) = \frac{R_{II}^2 + z_i^2}{2z_i}, \quad (3.25)$$

where R_{II} is given by,

$$R_{II} = R_0 - l_e, \quad (3.26)$$

A magnified schematic of the contact area of the inflated membrane is shown in Fig. 5(b). The inflation increases the pitch between fibers p_0 due to the stretch of the membrane and the new fiber pitch p is given as,

$$p(z_i) = \frac{p_0 (R_{II}^2 + z_i^2)}{2R_{II}z_i} \cos^{-1} \left(1 - \frac{2z_i^2}{R_{II}^2 + z_i^2} \right). \quad (3.27)$$

Positions of each fiber on the inflated membrane can be described with the angular displacement θ_s between fibers as given by,

$$\theta_s(z_i) = \frac{p_0}{R_{II}} \cos^{-1} \left(1 - \frac{2z_i^2}{R_{II}^2 + z_i^2} \right). \quad (3.28)$$

Comparing to the initial position, the displacement in the radial direction Δu and vertical direction Δv of a k^{th} fiber from the center can be calculated as,

$$\Delta u(z_i) = R(z_i) \sin k\theta_s(z_i) - kp_0, \quad \Delta v(z_i) = R(z_i) (1 - \cos k\theta_s(z_i)). \quad (3.29)$$

As it is assumed that the most of the deformation of a fiber will occur at the stem, the stretch of each fiber λ_f caused by the inflation of the membrane can be calculated by,

$$\lambda_f = \frac{1}{l_s} \left[\{(l_0 + \Delta v(z_i))^2 + \Delta u(z_i)^2\}^{\frac{1}{2}} - l_s + l_0 \right]. \quad (3.30)$$

When the stretch of a fiber λ_f exceeds the critical stretch λ_c calculated by Equation 3.23, the fiber can no longer withstand the inflation of the FAM and is detached from the surface. Assuming a $(k+1)^{th}$ fiber has reached the critical stretch and is detached from the surface, the radius of the contact area r_k where the k^{th} fiber still remains in contact along the edge can be estimated as,

$$r_k(k) = p_0(k-1) + \frac{p_0}{2}, \quad (k = 1, 2, 3, \dots). \quad (3.31)$$

The releasing force F_{rs} at the radius of contact r_k can be calculated by multiplying the critical pull-off force of a single fiber with the number of fibers in contact,

$$F_r(k) = \pi f_c \rho_f r_k(k)^2, \quad (3.32)$$

where ρ_f is the fiber density and f_c is the critical mean pull-off force for a single fiber, which was measured to be 2 mN experimentally. As shown by the circular markers in Figure 3.13(d), Equation 3.32 provides a discretized estimation of the releasing force with respect to the position of the k^{th} fiber from the center that is located on the edge in contact. Between the detachment of $(k+1)^{th}$ and $(k)^{th}$ fiber, even if the number of fibers in contact will not be changed, the releasing force will be reduced since those fibers will still be stretched by the inflation of the FAM. To simplify the analytical model, the discontinuous

releasing force between the $(k + 1)^{th}$ and k^{th} fiber is interpolated as a line based on the linear relationship of Hookes Law as shown by the dashed line in Figure 3.13(d).

According to the above model, the FAM can reach the releasing force of 2mN (indicated as alternated long and short red dashed line) at approximately 9.7 mm of inflation distance, which is equal to a membrane stretch λ_m of 2.47 as estimated by Equation 3.4. As discussed in the releasing force measurement section 3.4.1, the single fiber adhesion was achieved at 8 mm of inflation distance z_i corresponding to 2.3 of the membrane stretch (indicated as boxed solid line). Various factors can cause the difference between the simple theoretical estimation and the experimental results. First, the shape of membrane deformation might not be a perfect sphere. The configuration of the inflated FAM can only be assumed to be a sphere when the deformation is governed by the Neo-Hookean model, which can be valid only for small deformation. The thickness variance of the FAM could also cause an irregular shape of deformation deviated from the assumed sphere shape. Bending moment of micro-fibers at stem might have a non-negligible effect on the releasing. All the above possibilities must be carefully examined in order to develop a more advanced releasing modeling.

3.6 Demonstrations of Pick-and-release Manipulation

The superior adaptability of the soft gripper using the FAM has been demonstrated by the simultaneous transferring of 4.76, 5.55 and 6.35 mm in diameter steel balls as shown in Figure 3.14(a). With a small amount of inflation, the gripper could engage with all three of the different sized steel balls at once and successfully released them to the target site by inflating the FAM. Using such adhesion-based manipulation method, a piece of cover glass that is larger than the gripper and hard to pick up mechanically could also be manipulated as shown in Figure 3.14(b). Furthermore, the soft and inflatable gripper can manipulate lightweight and small parts by engineering the adhesion of micro-fibers on the FAM. As shown in Figure 3.14(c), a less sticky FAM, which has approximately 4 times smaller pull-off force than the FAM used for characterization of switching ratio

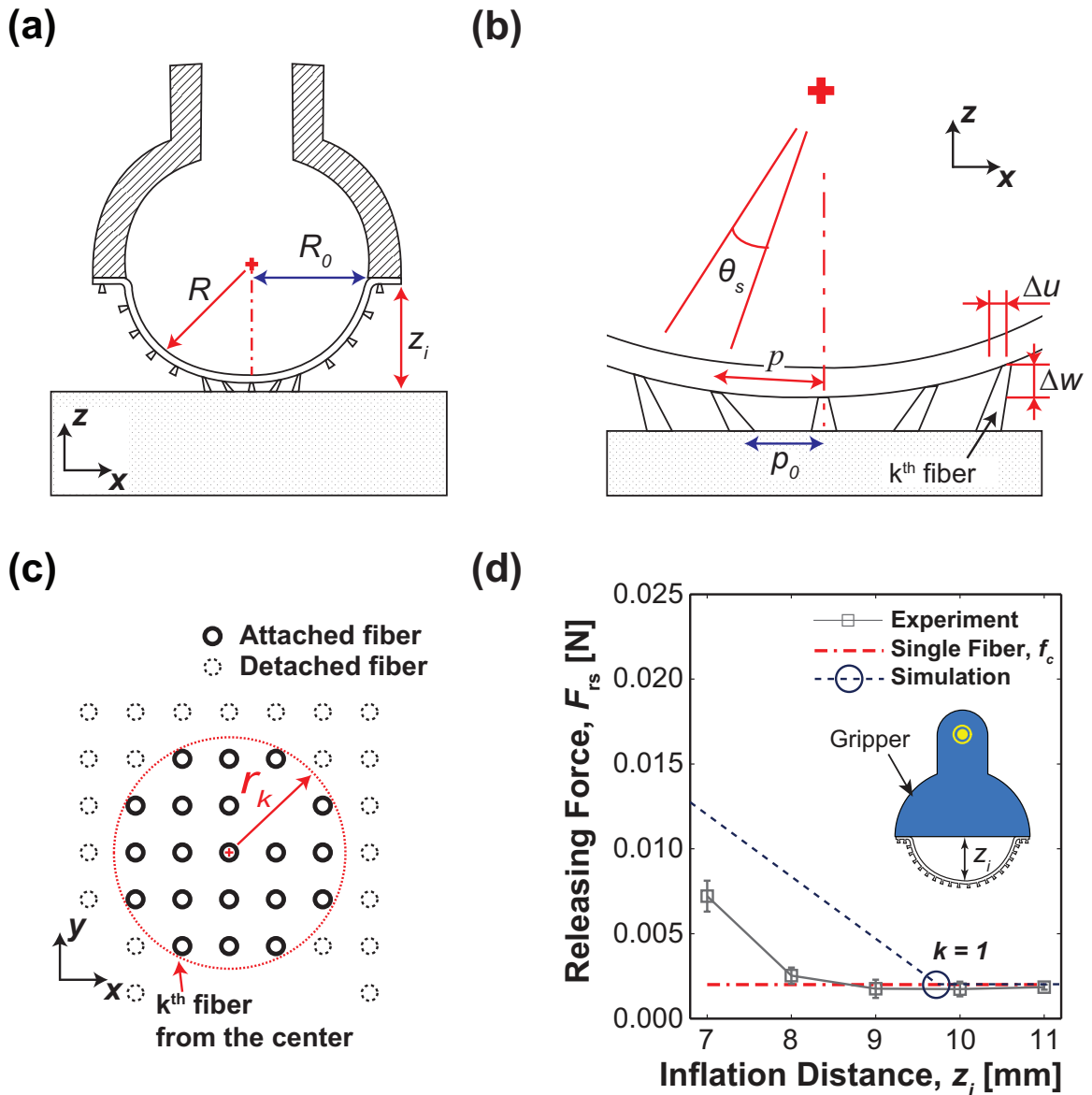


Figure 3.13: Analytical modeling of the releasing force F_{rs} : (a) Schematic figure of the shape of the inflated FAM, (b) Magnified figure of micro-fibers remained in contact at an inflated configuration, (c) Magnified figure of the contact area at an inflated configuration, and (d) Analytic estimation of the releasing force model depending on the inflation distance z_i where k represents the k^{th} fiber and the experimental results with 0.01 mms^{-1} of retraction speed. (Copyright © 2014 IEEE)

of pull-off force 3.4, could pick up and place a 2x2 array of 1 mm diameter silicon disks with 220 m thickness (weight of around 400 μg). Unlike previous soft gripping methods [53, 54, 57], the adhesion-based gripping mechanism is not sensitive to parts geometries, which allows the gripper to pick-and-release various shapes of 3D objects, such as an electrical resistance (Figure 3.14(d)), a right angle prism (Figure 3.14(e)), and a metal wrench (Figure 3.14(f)). The adhesive gripper could also manipulate a paper clip, which is hard to make tight air-sealing to be gripped by suction methods as shown in Figure 3.14(g). Without using a sophisticated feedback control system, the soft and adhesive gripper is versatile and can manipulate a range of different objects leaving no residue on the part surface, as far as the weight of the part is heavier than the adhesion of a single fiber and have enough stiffness not to be deformed by the stretch of the FAM during the releasing process.

3.7 Summary

The fibrillar adhesives on a membrane (FAM) has been fabricated with two different polyurethane elastomers. The mushroom-shaped fibrillar structures were made out of a polyurethane with a high work of adhesion for greater pull-off forces, while the other highly stretchable polyurethane allows the membrane to withstand up to 11 mm of vertical displacement when exposed to a high positive pressure differential. The fabricated FAM is approximately 16 mm in diameter and 75 μm in thickness and the micro-fibers are 105 μm in height, 45 μm in diameter at the stem, and 95 μm in diameter at the mushroom-shaped tip.

During the picking task, the gripper is brought down to a target object until the maximum contact area is achieved, and the preload is applied by a combination of the tension in the FAM and an additional air force F_a improving the adhesion and adaptation to the target geometry simultaneously. If the pull-off force is larger than the weight of the object F_w , the object can be lifted up and the holding force F_h is balanced by the object weight F_w .

In the releasing task, the pull-off force is reduced by controlled inflation of the FAM. A combination of a positive pressure differential inside of the gripper and the upward gripper movement creates a room for the FAM being stretched, resulting in successive detachments of the micro-fibers in contact by peeling. When the FAM is fully stretched at the final releasing step, and the micro-fibers remaining in contact are pulled off, reducing the pull-off force defined to the minimum releasing force F_{rs} . When the releasing force is smaller than the sum of the object weight F_w and adhesion between the object and the stage F_s , the object can be released from the gripper and placed onto the target destination.

Manipulability of the fibrillar adhesives on a membrane (FAM) has been characterized by the adhesion switching ratio of the gripper-object interface, which is defined as the ratio between picking and releasing force at the interface. First, the picking force of the FAM has been characterized based on the sequences described in the picking mechanism section 3.3.1 and measured to be approximately 0.41 N occurring at a preload of 1 N almost 10 times higher than that of the flat membrane. The releasing force of the FAM has also been characterized based on the sequences described in the releasing mechanism section 3.3.2 which is approximately 2 mN corresponding to a single fiber adhesion achieved with 8 mm of inflation distance at 0.01 mms^{-1} . Due to viscoelastic behavior of elastomer micro-fibers, the reduced pull-off forces of the inflated FAM were increased with faster retraction speed (0.1 mms^{-1}), requiring increased inflation of the FAM (11 mm of the inflation distance in order to achieve the same single fiber adhesion). Since the releasing force can be reduced up to a single tip adhesion with a stretch of the FAM, by engineering material or dimension of micro-fibers, the releasing force can be further reduced, enabling micromanipulation of lightweight small parts such as electronic components or particles. The controllable adhesion switching ratio of the FAM has been estimated to be approximately 204, which is superior to the previous works based on the peeling angle control of the fibrillar structure was up to 39 [28], 10 [60], and 14.8 [61].

The advantage of a soft backing of the FAM over a rigid backing for picking up a 3D object is examined by comparing the picking force between the FAM, the fibrillar adhesives on a rigid punch (FARP), and the flat membrane on different radius of steel balls ranging

from 1.6 mm to 25.4 mm in diameter based on the sequences described in the picking mechanism section 3.3.1. The picking forces of all the FAM, FARP, and the flat membrane were increased with ball size. Based on the results of the FAM and the flat membrane, the enhancement in adhesion using fibrillar adhesives has also been confirmed for curved surfaces. Especially, it has been confirmed that having the soft backing was advantageous over the rigid backing for fibrillar adhesion. The FAM showed higher picking force than that of the FARP due to the increased contact area. Comparing the weight of the balls, the maximum payload of the FAM was estimated to be 35 grams (0.35 N) corresponding to a 20 mm diameter steel ball, while the FARP could only carry up to 5 grams (0.05 N) corresponding to steel balls less than 12 mm in diameter. For the flat membrane, a ball that is bigger than 3 mm in diameter could not be carried since its weight of 0.13 grams (1.3 mN) is heavier than that of the membrane's maximum payload. The larger contact area of the membrane of the FAM covered with micro-fibers provided the higher maximum payload than that of the FARP, which proves the initial concept of the FAM.

In the analytical modeling section, simple models of the FAM for picking and releasing have been developed in order to provide design rules for optimization of dimensions and performance of the FAM. For the picking simulation, the membrane was discretized into two regimes, regime I is for the edge of the membrane having irregular shape and regime II is for the rest part of thin and regular membrane, and analytic models are developed separately for each regime. The developed model had good agreements with the experimental results for estimating the picking force and initial slope of linear increase in the reaction force. However, the maximum vertical displacements and eccentric saddle shape of force profile remained as future works to be improved. For the releasing simulation, the deformed configuration of the FAM when it is inflated has been considered to be a sphere shape by assuming the deformation is governed by the Neo-Hookean solid with a perfect and uniform thickness of the membrane. The releasing condition of micro-fibers in contact with a surface has been considered from geometrical relationships between the fibers and the inflated membrane geometry. The simple analytic estimation could calculate the minimum inflation distance of the FAM z_i for achieving the single fiber-tip adhesion to be 9.7 mm, which is approximately 1.7 mm bigger than the experimental results. In order

to improve in accuracy for both picking and releasing models, various assumptions and factors made for simplification of the models must take into account, such as simplification of the deformation shape, effect of irregular thickness, error in estimating the effective work of adhesion, the effect of fiber bending at the stem, and limitation on using the Neo-Hookean model for large deformation of hyperelastic membrane.

The superior adaptability and adhesion controllability of the soft gripper using the FAM have been demonstrated with a wide range of various 3D objects in size, shape, and number, such as three different sizes of steel balls, a cover glass, sub millimeter-sized silicon disk, electrical resistance, right angle prism, 60 mm long metal wrench, paper clip, and so on. The soft and adhesive gripper is versatile and can manipulate various objects leaving no residue on the part surface, as far as the weight of the part is heavier than the adhesion of a single fiber and have enough stiffness not to be deformed by the stretch of the FAM during the releasing process.

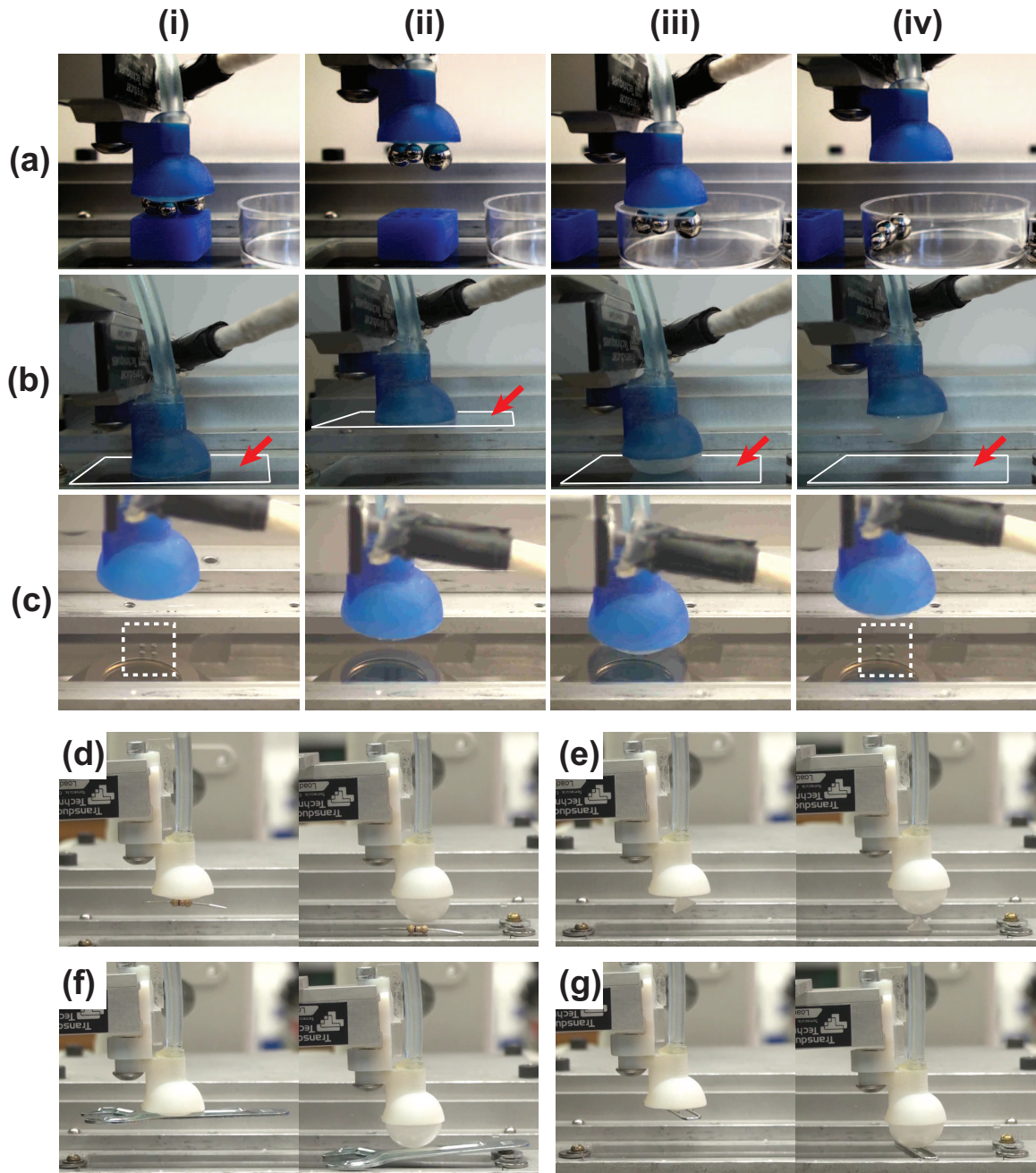


Figure 3.14: Demonstration of pick-and-release manipulations of the inflatable and adhesive Grip-per: (a) three different sizes of steel balls (4.76, 5.55 and 6.35 mm diameter) in parallel, (b) a piece of $24 \times 40 \times 0.13 \text{ mm}^3$ fragile cover glass (indicated by the red arrow and the white frame), and (c) 22 array of 1 mm diameter silicon disks (indicated by the white dashed box) ((i): applying a preload; (ii): picking up; (iii): inflating the FAM; (iv): releasing). (d) an electrical resistance, (e) a $5 \times 5 \times 5 \text{ mm}$ right angle prism, (f) a 60 mm long metal wrench, and (g) a paper clip (left: picking up; right: releasing). (Copyright © 2014 IEEE and Copyright © 2014 John Wiley & Sons, Inc.)

Chapter 4

Load Distribution Control of a Soft-backed Micro-fiber Array on Complex 3D Surfaces

4.1 Introduction

In this chapter, we discuss a soft robotic architecture for enhancing the interfacial load distribution on a large area of soft membrane. As shown in Figure 4.1, the soft adhesion-based gripping system proposed in this chapter allows the control of internal pressure to achieve equal load sharing on the interface over a large 3D surface. Our soft adhesion system increases adhesion through a combination of two fundamental mechanisms: (i) using a negative pressure differential to distribute the load more uniformly on the interface, and (ii) taking advantage of passive deformation of the soft system in response to the reduced chamber pressure, which can prevent the adhering membrane from peeling at a high negative pressure differential. Pneumatic pressure has been a popular choice as an actuator for soft systems due to its low drag resistance and rapid transport, abundant accessibility, and environmental compatibility [44, 88]. Here, we show that the pressure differential is also effective for enhancing the adhesion of a membrane-backed micro-fiber array on a wide range of curved geometries. This is accomplished with the existing pneumatic system used for gripping actuation and does not require the introduction of additional hardware,

including sensors and electronics. Experimental results show that pressure-controlled load sharing among the micro-fibers in contact with the surface does not only enhance adhesion but also leads to an area scaling law similar to that of the natural geckos adhesive system 4.6. Such area scalability has not been observed in other micro-fiber adhesives and suggests that improved interfacial load sharing is critical when grasping 3D non-planar geometries. (This chapter has been reprinted with permission from [80].)

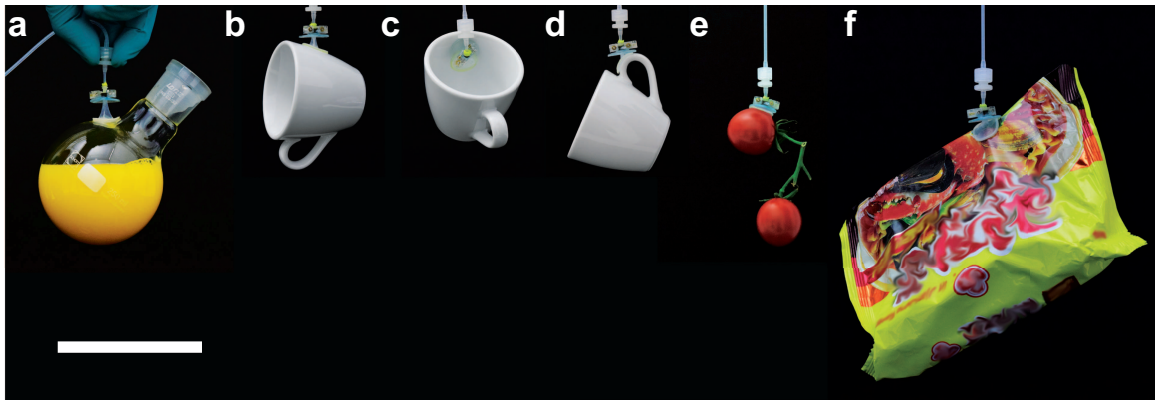


Figure 4.1: Demonstration of the proposed soft adhesion-based gripping system holding various 3D objects such as a (a) rounded glass flask filled with 200 mL of liquid (total weight of 307 grams), (b-d) 118 gram coffee cup, (e) 41 grams pair of cherry tomatoes, and (f) 139 gram plastic bag. The scale bar is 10 cm.

4.2 Structure and Basic Mechanism of the Soft Adhesion System

Figure 4.2a details structural features of the proposed soft adhesion system. A FAM is supported by a soft, deformable chamber, which is connected to a syringe pump to allow control of the system internal pressure (Figure 4.2a-I). The soft gripper chamber is 18 mm in diameter, 600 μm thick, and contains 400 μm diameter pillar-like internal spacers made out of a soft and highly stretchable silicone elastomer. The soft chamber is bracketed by a 3D-printed plastic outer case, ensuring evenly distributed preload over the whole contact area. Each silicone component of the system is bonded using a vinylsiloxane elastomer. The FAM is composed of an array of vertically aligned, mushroom-shaped,

polydimethylsiloxane (PDMS) micro-fibers with 69 μm tip diameter, 31 μm spacing, and 42 μm height, supported by a thin PDMS backing layer with 250 μm thickness (Figure 4.4 and 4.5). As shown in Figure 4.2a-II, the micro-fibers (Figure 4.2a-II8) covering entire area of the membrane provide a gap between the substrate and the membrane, allowing air to seamlessly travel through the contact interface, preventing development of any suction that could contribute to the soft system adhesion. The FAM can be cleaned using a wet [89] or dry process [90], allowing reliable and repetitive performance, which can otherwise be influenced with the buildup of dust, oil, or dirt [13].

The effect of a negative pressure differential (ΔP) on the load sharing is shown in Figure 4.2b. Here, the internal pressure (P_i) corresponds to the air pressure in the gripper chamber, tubing, and syringe pump and is always positive. The pressure differential is defined as the internal pressure subtracted by the atmospheric pressure (P_{atm}), and can be either positive or negative. Therefore, a negative pressure differential means that an absolute value of the internal pressure is lower than the atmospheric pressure (101.3 kPa). Likewise, a high negative pressure differential indicates that the internal pressure is substantially lower than the atmospheric pressure. Under a high negative pressure differential, the atmospheric pressure forces the chamber to collapse over the FAM (Figure 4.2b-I). The spacers in the chamber (Figure 4.2b-III6) ensure that the FAM is exposed to the pressure differential even when the chamber has collapsed (Figure 4.2b-III). In contrast to typical adhesion systems that peel and exhibit poor adhesion under large deformations during pulling, our gripping system benefits from deformation since it allows the spacers in the soft chamber to lift up from the backing and exposes a larger area of the membrane to the negative pressure differential. This, in turn, enhances the load sharing by enabling the negative pressure differential to more uniformly distribute the interfacial tensile stress and improve bonding strength (F_{ad}) (Figure 4.2b-II).

Figure 4.2c shows a representative force measurement of the soft adhesion system with its corresponding force (blue) and pressure (red) curves. Figure 4.2c-III gives reaction force (F_r) as a function of time (t). Unlike previous Chapter 3, here we define positive reaction force to be pushing force down to substrates called preload (F_{pre}), while negative reaction

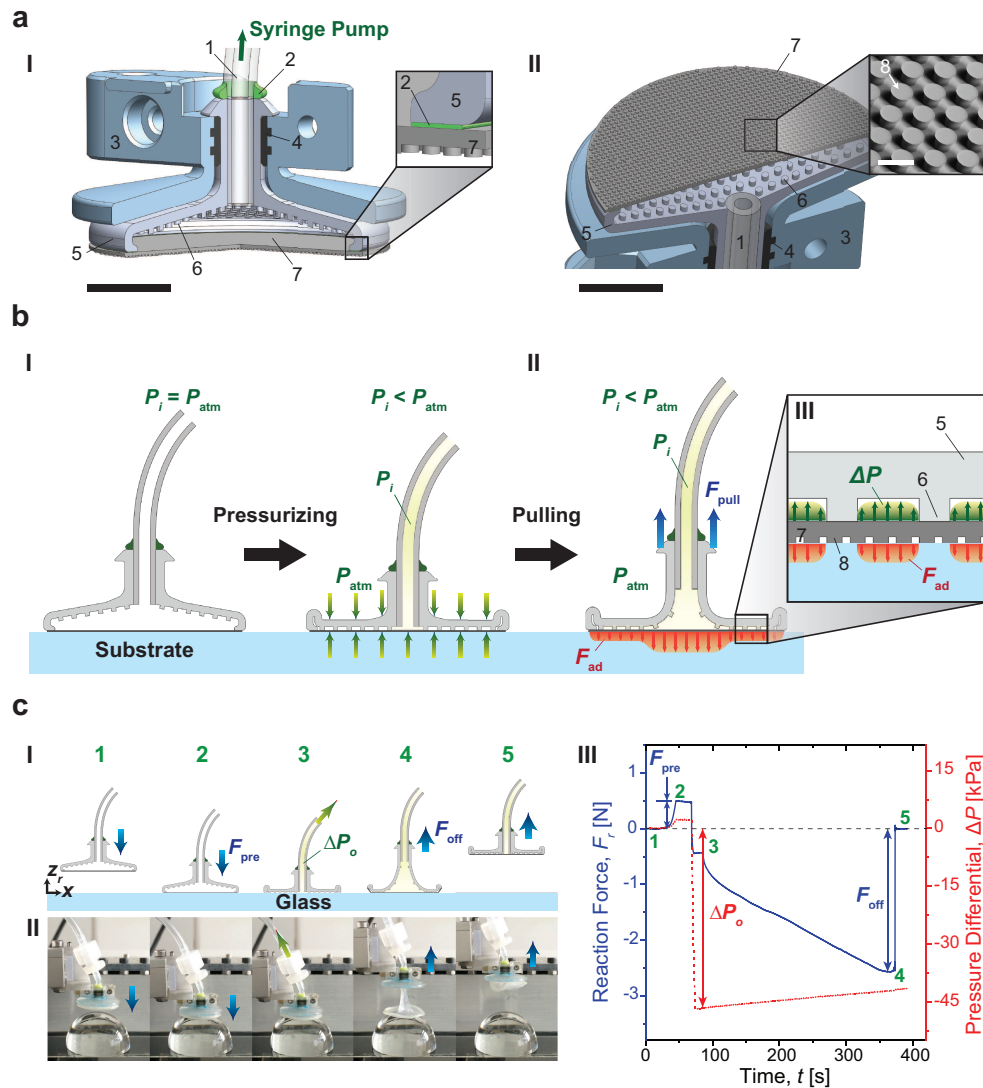


Figure 4.2: Schematics of structure, mechanism and a representative adhesion test of the soft adhesion system. (a) A cross-section of 3D assembly of the proposed system from side (I) and from bottom (II) of the system. 1: silicone tubing, 2: vinylsiloxane, 3: outer case, 4: rubber ring, 5: soft chamber, 6: spacer between the chamber and the FAM, 7: the FAM, 8: mushroom-shaped PDMS micro-fibers. Larger scale bars (black) indicate 5 mm, while the smaller scale (white) inside of the inset in (II) corresponds to 100 μm . (b) A schematic of the proposed system when pressurized with a negative pressure differential (ΔP) (I) and pulled with a pull-up load (F_{pull}) (II). The inset (III) shows a schematic of pressure distribution between the spacers in the soft chamber and adhesion stress on the contact interface. (c) Adhesion test of the soft system. A schematic of experimental procedure (I), snapshots of the soft system under a negative pressure differential on a 30 mm diameter glass hemi-sphere in accordance with each step (II), and corresponding profiles of reaction force (F_r) and pressure differential inside the chamber with respect to elapsed time (III). The initial pressure (ΔP_o) here is approximately -47 kPa. The numbers indicated in green are correlated with the experimental procedure: (1) approaching, (2) preloading, (3) applying initial pressure, (4) pulled off, and (5) detached.

force to be adhesion at the interface. First, the soft adhesion system approaches a substrate (Figure 4.2c-I1) and is brought to contact (Figure 4.2c-I2) with a compressive preload force (F_{pre}) induced at the interface. The preload is the maximum reaction force as shown in Figure 4.2c-III, ranging from 0.5 N to 1.0 N depending on the substrate radius of curvature. A negative pressure differential is applied to the inside of the soft chamber during a pre-defined contact time, then the system is slowly retracted at $50 \mu\text{m} \cdot \text{s}^{-1}$ unloading speed to minimize possible viscoelastic effects on the adhesion. The pressure differential at the beginning of the retraction (Figure 4.2c-I3) is defined as initial pressure (ΔP_o), which can be either positive or negative. The reaction force decreases during the retraction until it reaches the pull-off force (F_{off}) (Figure 4.2c-I4), which corresponds to the minimum reaction force in Figure 4.2c-III. The soft adhesion system snaps off from the substrate instantaneously after the pull-off force is reached (Figure 4.2c-I5), as shown in Figure 4.2c-III.

4.3 Fabrication

4.3.1 Fabrication of the Elastomer Fibrillar Adhesives on a Membrane (FAM)

Soft PDMS molds containing cylindrical cavities were obtained by replicating SU-8 lithographic templates as previously reported [91, 92]. Sylgard[®] 184 siloxane base and curing agent were mixed in a 10:1 ratio, degassed and casted on the PDMS mold shaped in the cylindrical cavities. The excess prepolymer was removed by a bar coater (K-Hand-Coater, Erichsen GmbH & Co. KG) creating a ca. 250 μm thin backing layer. The sample was cured in a vacuum oven at 90 °C for 1 hour and demolded (Figure 4.3). Micro-patterns with 52 μm diameter, 48 μm spacing and 38 μm height were received (Figure 4.4). Sylgard[®] 184 prepolymer was poured on a glass plate and a thin film of ca. 20 μm thickness was created by a film applicator (Multicator 411, Erichsen GmbH & Co. KG). The thin polymer film was precured in the oven at 90 °C for 3 minutes. The cylindrical fibers, fabricated in the previous step, were manually inked onto the precured thin film and placed on a perfluorinated silicon wafer. The precuring of the polymer film

is necessary in order to increase its viscosity and thereby enhancing the transfer of the polymer material to the fibers for creating optimal mushroom-shaped tips. After curing at 90 °C for 1 hour, the printed patterns were carefully peeled off and the FAM with 69 μm tip diameter, 31 μm spacing and 42 μm height mushroom-shaped micro-fibers were obtained (Figure 4.4 and 4.5).

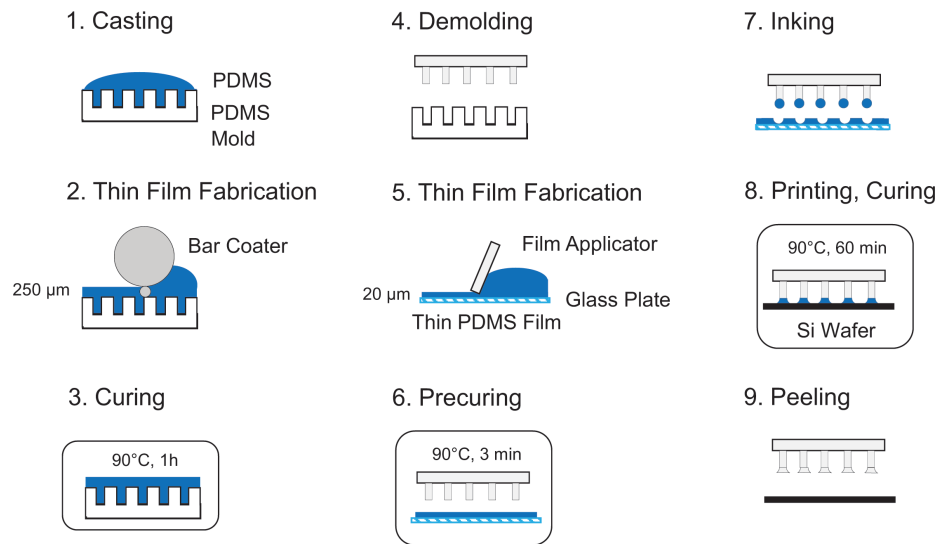


Figure 4.3: Experimental procedure for fabricating the FAM. A schematic shows the individual steps of the fabrication process.

4.3.2 Fabrication of the Rigid Adhesion System

The rigid chamber was designed with a CAD software (SolidWorks) and fabricated by a 3D printer (Objet260 Connex, Stratasys Ltd.) using VeroClearTM as the rigid material. The printed rigid chamber was thoroughly cleaned with 1 mol of NaOH solution in order to remove supporting materials. Surface modification on surface of the chamber was performed by inking the chamber into a primer (1200 OS Primer, Dow Corning[®]), followed by a drying step at room temperature for 30 minutes. The surface modification is important to ensure strong bonding between the chamber and the FAM. A silicone adhesive (Sil-Poxy[®], Smooth-On Inc.) was poured on a glass plate and a thin film of ca. 50 μm in

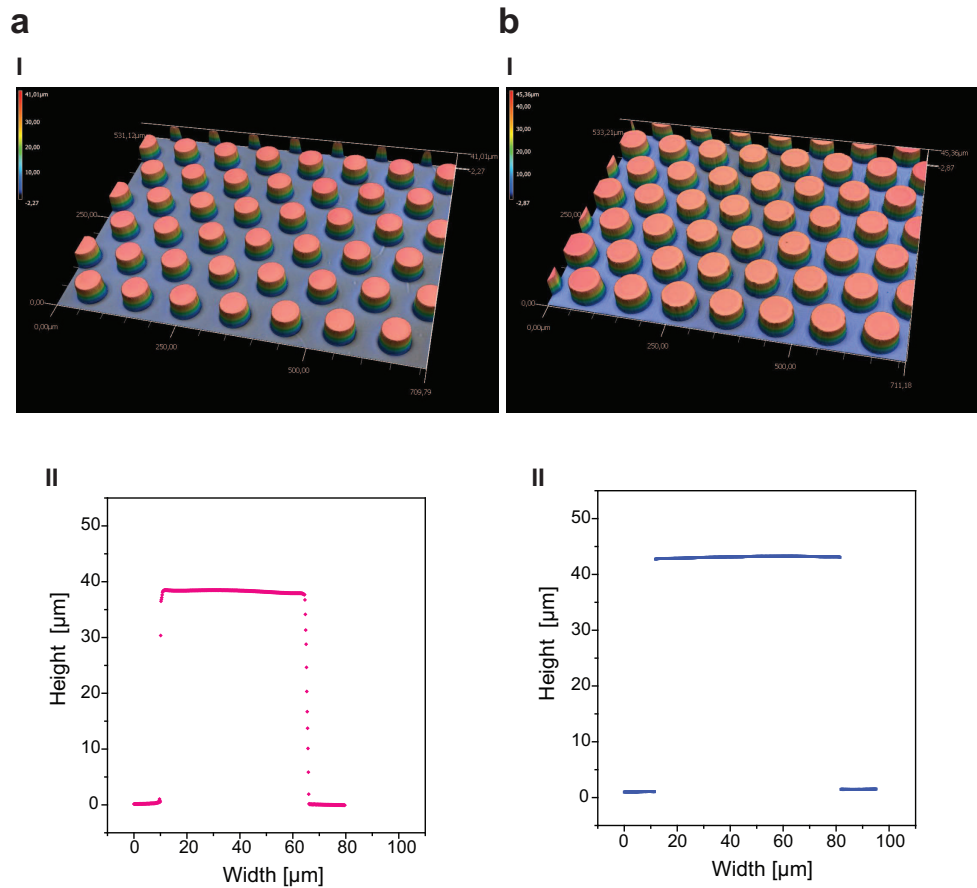


Figure 4.4: 3D scanned images of PDMS patterns and dimensions. (a) 3D image (I) and profile (II) of cylindrical PDMS patterns with $52\ \mu\text{m}$ diameter, $48\ \mu\text{m}$ spacing and $38\ \mu\text{m}$ height. (b) 3D image (I) and profile (II) of mushroom shaped PDMS patterns with $69\ \mu\text{m}$ diameter, $31\ \mu\text{m}$ spacing and $42\ \mu\text{m}$ height. Note that the pillar stems of the mushroom shaped patterns cannot be measured since they are covered by the overhanging tips.

thickness was created by a film applicator (Multicator 411, Erichsen GmbH & Co. KG). The chamber was inked into the thin Sil-Poxy[®] film and placed onto the FAM. After curing at room temperature for 30 minutes, the FAM was strongly bonded to the rigid chamber (Figure 4.6).

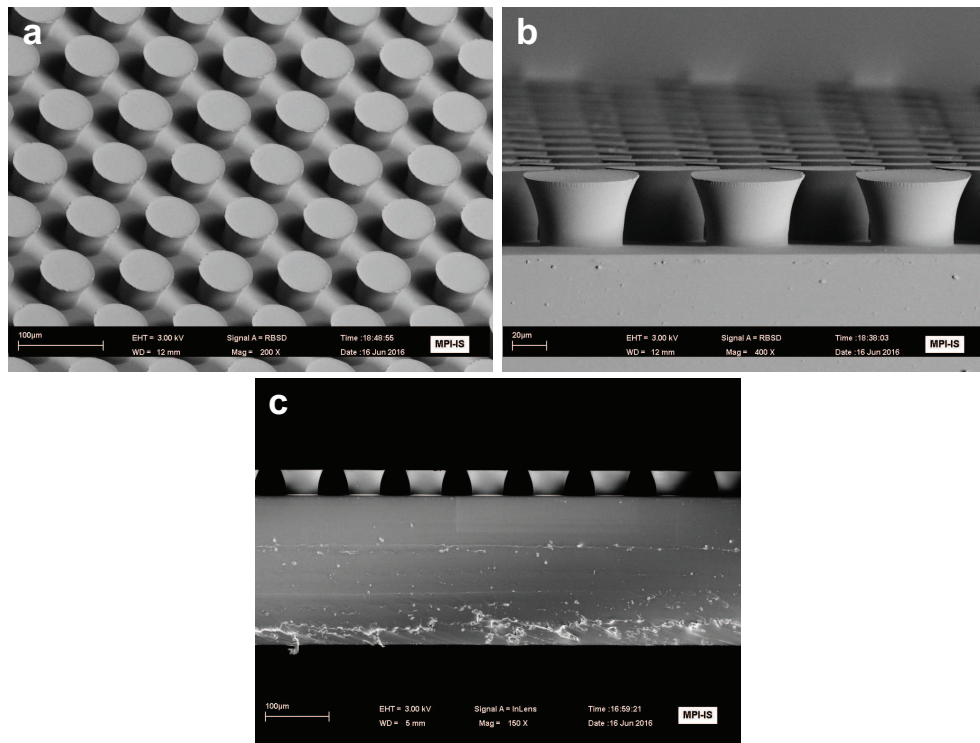


Figure 4.5: SEM images of mushroom-shaped elastomer micro-fiber arrays on the FAM. Top (a) and side-view (b) of mushroom-shaped micro-fiber arrays with $69\ \mu\text{m}$ in diameter, $31\ \mu\text{m}$ in spacing, and $42\ \mu\text{m}$ in height. (c) A side-view of the FAM supported by a thin backing layer with ca. $250\ \mu\text{m}$ in thickness.

4.3.3 Fabrication of the Soft Adhesion System

A negative mold made out of Ecoflex[®] 00-30 (Smooth-On Inc.) for the soft chamber was obtained by replicating a 3D-printed composite model shaped as the chamber. The composite model was designed with a CAD software and fabricated by a 3D printer (Objet260 Connex, Stratasys Ltd.) using VeroClear[™] as rigid and TangoBlack[™] as soft materials. The rigid axis grants stability to the model, while the soft body facilitates the peeling. The printed chamber model was thoroughly cleaned with 1 mol of NaOH solution in order to remove supporting materials. The chamber was fixed using a double-sided tape in a small plastic petri dish. A 1:1 ratio of Ecoflex[®] 00-30 prepolymer and crosslinker was mixed, degassed, and casted into the petri dish and cured at room temperature for 6 hours (Figure 4.7). After the elastomer was cured, the composite model of the soft

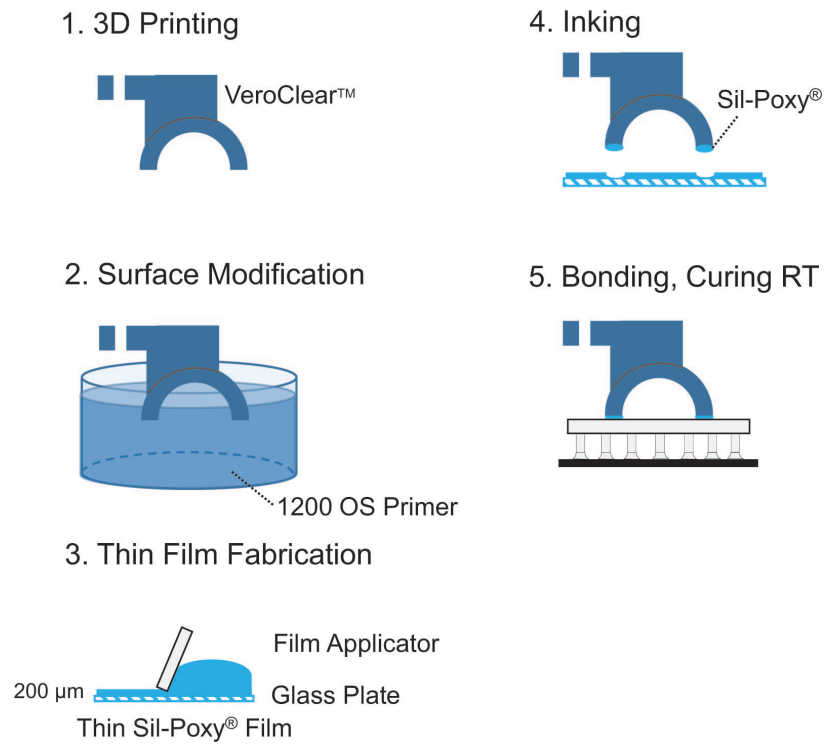


Figure 4.6: Experimental procedure for fabricating the rigid adhesion system. A schematic shows the individual steps of the fabrication process for obtaining a rigid system with the FAM.

chamber was carefully demolded.

The fabricated negative mold of the soft chamber was treated in an oxygen plasma at 100 W for 2 minutes, followed by the surface modification using Hexadecafluoro-1,1,2,2-tetrahydrooctyltrichlorosilane for 1 hour in vacuum and curing at 90 °C for 30 minutes. The perfluoro coating of the mold is important to reduce the adhesion of the casting materials in the following replication process. The mold consists of two components, the soft negative of the chamber and a thin metal bar used for a spacer to create an air channel in the chamber (Figure 4.7). A 1:1 ratio of Ecoflex[®] 00-50 (Smooth-On Inc.) Parts A and B were mixed, degassed and injected inside of the negative mold using a syringe. After curing at room temperature for 6 hours, the mold and the soft chamber were carefully demolded. A Vinylsiloxane polymer (Flexitime[®] Medium Flow, Heraeus Kulzer GmbH) was applied on a glass plate and a thin film of ca. 50 μm thickness was created by a film applicator

(Multicator 411, Erichsen GmbH & Co. KG). The soft chamber was manually inked into the polymer film and placed on the FAM. The vinylsiloxane could develop a strong bond between the soft chamber and the FAM after 5 minutes of curing at room temperature.

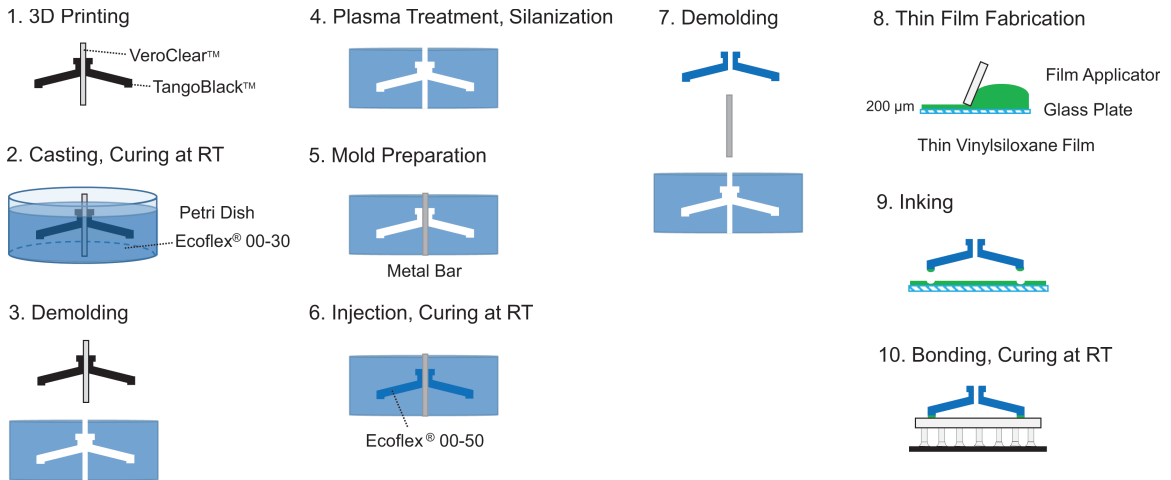


Figure 4.7: Experimental procedure for fabricating the soft adhesion system. A schematic shows the individual steps of the fabrication process for obtaining a soft system with the FAM.

4.4 Modeling the Effect of Pressure Differential on Adhesion

4.4.1 Modeling Load Distribution among Microfibers

We used principles of elasticity and stationary potential to examine the influence of internal pressure differential (ΔP_o) on the distribution of load among the micro-fibers in contact with the surface and to estimate the membrane adhesion on curved surfaces. To develop a qualitative understanding of the load distribution among fibers, the axisymmetric array on the FAM is modeled using 2D plane-strain linear elasticity [93]. As shown in Figure 4.8a, the FAM is simplified as an incompressible Hookean solid (Young's modulus $E_m = 2.1$ MPa [94]), which has a diameter $L_m = 2.15$ mm and thickness $h_0 = 250$ μm. The edge of the FAM is subject to a vertical displacement (u_0) corresponding to 5% of the thickness at the edge. Each micro-fiber has a width $L_f = 50$ μm, height $h_f = 50$ μm, and spacing $L_g =$

50 μm , and is assumed to remain in contact to the substrate with the prescribed loading conditions.

We perform a numerical calculation to obtain vertical stress (σ_{22}) within the FAM when pulling it up from a flat substrate under various differential pressures (ΔP_o). The FAM is simplified as an incompressible Hookean solid whose dimensions and boundary conditions are detailed in Figure 4.8a. The analysis is further simplified by modeling the axisymmetric system in 2D and assuming plane strain conditions.

The elastic deformation is represented by a displacement field $\mathbf{u} = u_1(X_1, X_2)\mathbf{E}_1 + u_2(X_1, X_2)\mathbf{E}_2$, where the Cartesian coordinates X_1 and X_2 and Euclidean bases \mathbf{E}_1 and \mathbf{E}_2 correspond to the horizontal and vertical directions, respectively. According to the Hookes law, stress in the $\mathbf{E}_1 - \mathbf{E}_2$ plane has components (1)

$$\begin{aligned}\sigma_{11} &= \frac{E_m}{1 - \nu^2} \left(\frac{\partial u_1}{\partial X_1} + \nu \frac{\partial u_2}{\partial X_2} \right), \sigma_{22} = \frac{E_m}{1 - \nu^2} \left(\nu \frac{\partial u_1}{\partial X_1} + \frac{\partial u_2}{\partial X_2} \right), \\ \sigma_{12} = \sigma_{21} &= \frac{E_m}{4(1 + \nu)} \left(\frac{\partial u_1}{\partial X_2} + \frac{\partial u_2}{\partial X_1} \right).\end{aligned}\quad (4.1)$$

At static equilibrium, the stress tensor $\boldsymbol{\sigma}$ must satisfy the balance law $\nabla \cdot \boldsymbol{\sigma} = 0$, where ∇ is the Lagrangian nabla operator. For 2D plane-strain elasticity, divergence-free stress implies the following form of the Navier-Lame equations:

$$\begin{aligned}\frac{\partial^2 u_1}{\partial X_1^2} + \nu \frac{\partial^2 u_2}{\partial X_1 \partial X_2} + \psi \left(\frac{\partial^2 u_1}{\partial X_2^2} + \frac{\partial^2 u_2}{\partial X_2 \partial X_1} \right) &= 0 \text{ and} \\ \frac{\partial^2 u_1}{\partial X_2^2} + \nu \frac{\partial^2 u_1}{\partial X_2 \partial X_1} + \psi \left(\frac{\partial^2 u_2}{\partial X_1^2} + \frac{\partial^2 u_1}{\partial X_1 \partial X_2} \right) &= 0,\end{aligned}\quad (4.2)$$

where $\psi = (1 - \nu)/4$. The solution to Eq. 4.2 must satisfy the following boundary conditions: $u_1 = u_2 = 0$ where the membrane is in contact with the substrate, $u_1 = 0$ and $u_2 = u_0$ at the membrane edges, $\sigma_{22} = \Delta P_o$ along the top of the membrane, and $\boldsymbol{\sigma} \cdot \mathbf{n} = 0$ everywhere else, where \mathbf{n} is the surface normal. The resulting boundary value problem is solved with the method of finite elements using the pdenonlin function in MATLAB

(R2015a; Mathworks, Inc.).

Of particular interest is the vertical stress σ_{22} within the micro-fibers, which is normalized by the Young's modulus E_m . It is also convenient to define a normalized surface pressure $\hat{p} = ((1 - \nu^2)\Delta P_o)/E_m$. In the absence of a negative pressure differential (i.e., $\hat{p} = 0$), stress is concentrated in the outermost fibers when the edges of the membrane (thickness h_0) are lifted by the prescribed vertical displacement (Figure 4.8b). Decreasing the pressure leads to a more uniform stress distribution, with the vertical stress at the center fiber ($\sigma_{22,c}$) approaching the stresses at the edge ($\sigma_{22,e}$). Referring to Figure 4.8c, the ratio $\sigma_{22,c}/\sigma_{22,e}$ steadily decreases and can even drop below 1.0 for a sufficiently high negative pressure differential. Although these results are based on 2D plane-strain elasticity, they nonetheless give qualitative insights on how negative pressure can be used to control the load distribution within the axisymmetric system.

4.4.2 Modeling Adhesion of a Soft Membrane on Spherical Geometries

To investigate the influence of internal air pressure on membrane adhesion to non-planar 3D geometries, we adapt our previous analysis [79] based on the principle of minimum potential energy [95, 96, 97]. As shown in Figure 4.9a, this rigid version of the adhesion system is composed of the circular FAM supported along its edge by a hemispherical chamber. The chamber has the same 18 mm diameter, but slightly thicker wall of 1 mm, compared to the soft chamber. As with the soft gripper, the FAM used for the rigid gripper is composed of PDMS and has a thickness of 250 μm . Examining this alternative system simplifies the analysis by eliminating the elastic deformation of the chamber and allowing us to instead focus on the deformation of the membrane. In particular, it enables us to examine the influence of various design parameters (e.g., membrane thickness and elastic modulus) and identify conditions that lead to more uniform load sharing control.

As with the fiber array load distribution model, the purpose of the membrane adhesion

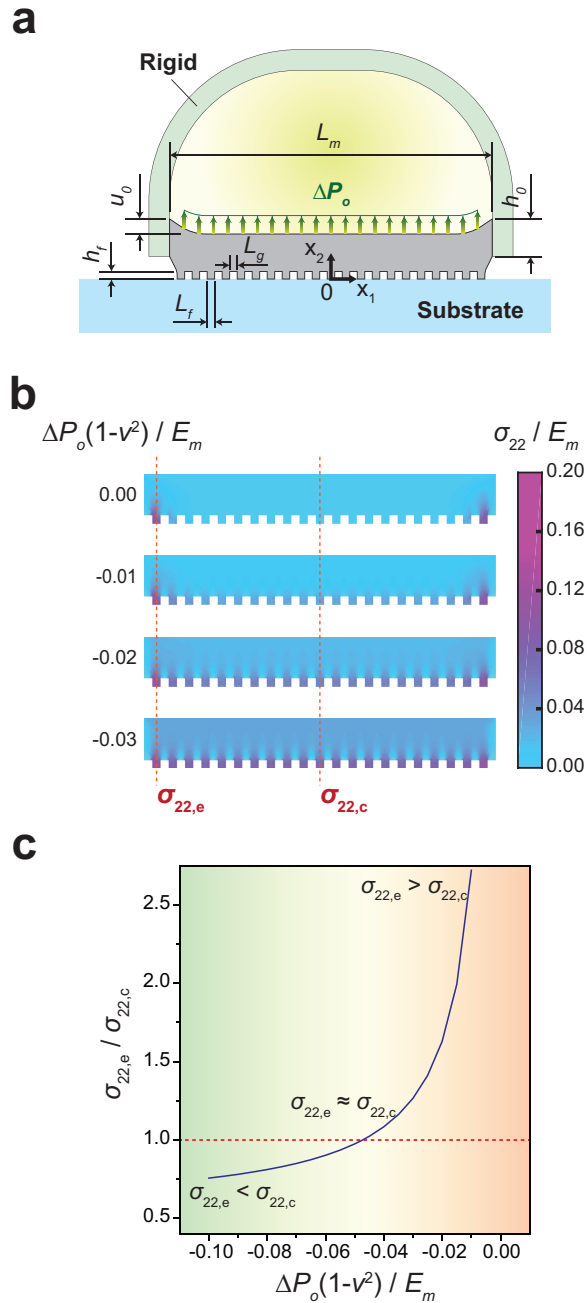


Figure 4.8: Finite element analysis for modeling vertical stress within the FAM. (a) A schematic of dimensions and boundary conditions of the FAM clamped at the edge and being pulled up by a rigid support under a negative pressure differential (ΔP_o). (b) A colormap of normalized vertical stress (σ_{22} / E_m) within the FAM for selected normalized pressures $\hat{p} = ((1 - \nu^2)\Delta P_o) / E_m$. (c) A ratio in the vertical stress between the edge and the center ($\sigma_{22,e} / \sigma_{22,c}$) depending on the normalized pressure \hat{p} . Here, $\sigma_{22,e}$ is the vertical stress on the first fiber from the edge of the FAM and $\sigma_{22,c}$ is on the fiber at the center.

theory is to establish a qualitative understanding of how negative differential pressure influences the interfacial mechanics. To further simplify the analysis, while still preserving the primary mechanics that govern adhesion, we make the following assumptions. First, the fibrillar interface is assumed to be a non-structured flat adhesive surface. Next, the elastomeric FAM is assumed to be incompressible, has a uniform thickness over the entire area, and deforms into the shape of a truncated cone. These assumptions imply the principle stretches in the circumferential (λ_ρ), meridional (λ_φ), and thickness (λ_t) directions on a spherical substrate as follows:

$$\lambda_\rho = \sqrt{(z + r_b - \sqrt{r_b^2 - r^2})^2 + (R_0 - r)^2} / (R_0 - r), \lambda_\varphi = 1, \text{ and } \lambda_t = 1 / \lambda_\rho \cdot \lambda_\varphi. \quad (4.3)$$

Such a simple geometry assumption for the deformed shape is reasonable for a membrane that is subject to a relatively low negative pressure differential (ΔP_o) and high work of adhesion (ω_{ad}). Here, R_0 is the radius of the FAM, which is 8 mm, r_b is the radius of a curved surface, z is the vertical position of the rigid adhesion system with respect to the top of the curved surface where the origin (o) is located, and r is the contact radius at the given z (Figure 4.9a).

The FAM on the rigid system making contact with a spherical curved substrate is shown in Figure 4.10. Additional boundary conditions and equations are employed to consider the mechanics of membrane adhesion on spherical substrates under a pressure differential. Initial boundary conditions for the vertical position of the system (z_0) and the contact radius (r_i) will be different depending on the size of the FAM with respect to the curved surfaces (Figure 4.11). In the case that the spherical surface is larger than the adhesive membrane ($r_b \geq R_0$; Figure 4.10b), the FAM achieves full contact prior to retraction, such that

$$z_0 = -r_b + \sqrt{r_b^2 - R_0^2} \text{ and } r_i = r_e. \quad (4.4)$$

It should be noted that the position z is defined with respect to the origin and can be either positive or negative depending on the initial vertical position of the adhesion system (z_0) and retraction distance (z_r). Due to manufacturing imperfection and misalignment, the FAM on the rigid system could not often make full contact even on a flat substrate

(Figure 4.10d). We estimated from the experiments that approximately 700 μm from the edge of the FAM cannot make contact in average, which provides the maximum effective contact radius (r_e) to be 7.3 mm.

In the case when the spherical surface is smaller than the maximum effective contact radius ($r_b < r_e$; Figure 4.10a), the FAM is assumed to be brought down to the center of the spherical substrate. The FAM wraps around the substrate, making conformal contact with the initial position and contact radius such that

$$z_0 = -r_b \text{ and } r_i = r_b^2/R_0. \quad (4.5)$$

In experiments, the FAM could not be fully brought down to the center of the ball, as tensile stress may break the FAM during the preloading process. Instead, the system is brought down in contact until the preload reaches the predetermined value, which is in a range from 0.5 to 1.0 N. If the radius of a spherical substrate is in between the size of FAM and the effective maximum contact radius ($r_e \leq r_b < R_0$), the initial boundary conditions are

$$z_0 = -r_b \text{ and } r_i = r_e. \quad (4.6)$$

During retraction, the FAM stretches due to adhesion, causing a volume change inside of the chamber (Figure 4.10e). A volume in the shape of truncated cone deformation (V_t) subtracted with a volume of the spherical surface covered by the FAM in contact (V_c) increases the total volume (V) enclosed by the FAM in addition to the initial volume of the rigid adhesion system (V_0) as

$$V = V_0 - V_c + V_t. \quad (4.7)$$

The initial volume (V_0) is the sum of the volume inside of the chamber, tubing, and syringe pump, which is approximately 7.2 mL. The volume inside of the truncated cone as well as the volume inside of the spherical cap covered by the FAM are

$$V_c = \frac{\pi h_c}{6}(3r^2 + h_c^2) \text{ and } V_t = \frac{\pi}{3}(z + h_c)(R_0^2 + r^2 + R_0r), \quad (4.8)$$

respectively, where $h_c = r_b - \sqrt{r_b^2 - r^2}$ is the vertical distance between the system and the top of the spherical surface. The total potential energy (Π) of the FAM in the equation 3.20

is modified as a sum of elastic energy in a reference volume of detached area, adhesion energy of the membrane in contact, and work done by pressure in order to take the influence of internal pressure into account,

$$\Pi(r, z) = \pi(R_0^2 - r^2)h_0W_o(r, z) - \pi r^2\omega_{ad} + U_p, \quad (4.9)$$

where h_0 is the natural thickness of the FAM, ω_{ad} is the effective work of adhesion, and W_o is the strain energy density function given in the equation 3.19. The work done by air pressure (U_p) is

$$U_p = P_{atm}(V - V_0) - (P_{atm} + \Delta P_o)V_0 \ln\left(\frac{V}{V_0}\right). \quad (4.10)$$

The critical contact radius (r_c) at a given value of vertical displacement of the system (z^*) can be calculated as the solution of the equation 3.20 for static equilibrium. By knowing the critical contact radius for different values of the vertical displacement which ranges from zero retraction distance (z_r) until the FAM is pulled off, the reaction force (F_r) can be calculated by taking the first partial derivative of the total potential energy (Π) with respect to the given vertical displacement (z^*) and substituting the contact radius (r) with the critical contact radius (r_c) in the equation 3.21.

Figure 4.9b shows the calculated profiles of reaction forces (F_r) between the rigid system and a flat glass substrate depending on different initial pressures with respect to retraction distance (z_r). Before the retraction (unloading) occurs, decrease in the internal pressure pulls the soft adhesion system towards the interface, which explains the initial negative reaction force in Figure 4.9b. As long as adhesion of the FAM can sustain the applied internal pressure, the decrease in the initial reaction force can be estimated by the initial pressure multiplied by the actual contact area. This adhesion, however, is not due to any suction but instead arises from the uniform distribution of the interfacial load among the fibers in contact with the surface, as simulated in Figure 4.8.

At the beginning of the retraction, the reaction force shows a significant drop until the edge of the FAM in contact reaches its critical interfacial strength and starts peeling off. According to our model, the drop becomes less steep with a smaller initial contact area,

requiring a longer retraction distance to reach the critical interfacial strength for peeling (Figure 4.11). After transitioning through the dramatic decrease, the reaction force begins increasing in accordance with the peeling mechanics of the adhesive membrane, until the FAM is completely detached.

A higher negative pressure differential can result in higher pull-off force of the rigid adhesion system by distributing the load over the entire contact area more uniformly (Figure 4.9b). Meanwhile, the negative pressure differential could accelerate detachment of the FAM by additional tensile stress and a higher peeling angle [98] caused by the deformation of the membrane as it is pulled into the inner chamber of the rigid adhesion system (Figure 4.10c of the SI Appendix). Figure 4.9c and 4.9d show calculations of the pull-off forces (F_{off}) on spherical glass substrates with diameters (d_b) ranging from 10 mm to 500 mm for various design parameters of the FAM. The results indicate that its thickness (h_0) and Young's modulus (E_m) are not effective for increasing the pull-off force for small spherical geometries (Figure 4.9c). On the other hand, both the effective work of adhesion (ω_{ad}) and negative pressure differential (ΔP_o) could increase the pull-off force for all spherical geometries (Figure 4.9d). Actively tuning the effective work of adhesion is often difficult once the membrane is fabricated. Potential methods for tuning include heating [99], electrostatic charging [100], or other forms of active stimulation. Among these methods, pressure-controlled adhesion tuning is attractive since it can be easily combined with other pneumatic elements, which already exists for actuating a soft robotic system [101]. Our analysis in Figure 4.9d-II predicts that the adhesion can be doubled with respect to a decrease in the initial pressure by 4 kPa for the entire range of examined 3D surface curvatures.

Figure 4.9f shows the pull-off force of the rigid adhesion system for different initial pressures tested on flat and spherical glass substrates with 15 mm, 30 mm, and 60 mm diameter. The experimentally measured reaction force profiles for adhesion to the flat substrate are also presented in Figure 4.9e. The effective work of adhesion of the FAM and corresponding adhesion stress were estimated to be $4.1 \text{ J} \cdot \text{m}^{-2}$ and 101 kPa, respectively (Figure 4.14b and Table 4.2). Various initial pressures were applied depending on the

spherical curvatures by means of volume changes in the syringe pump. The positive initial pressure is caused by compression of the system during preloading when no air volume is withdrawn.

The experimental reaction forces on the flat glass substrate in Figure 4.9e show reasonable qualitative agreement with the theoretical model (Figure 4.9b) for how the reduction in the initial pressure results in a higher pull-off force and shorter retraction distance for detachment. The measured pull-off forces in Figure 4.9f are close to the theoretical predictions, shown as solid lines, with an average deviation of only 11% from the experimental results. The applicable maximum negative initial pressure was only -4.1 kPa on the glass sphere with 30 mm diameter, and became even smaller for the glass sphere with 15 mm diameter. For the latter case, the maximum negative pressure reduced to -0.7 kPa and corresponded to a small contact area and lower peel resistance, as shown in Figure 4.9f. The pull-off force on the flat glass was increased by 2.2 times, while it was enhanced up to 5 times on the glass sphere with 30 mm diameter at maximum. We observed an only 1.2 times improvement in the pull-off force on the sphere with a 15 mm diameter.

4.5 Characterizations

4.5.1 Experimental Setup

The customized adhesion measurement setup was mounted on an inverted optical microscope (Axio Observer A1, Zeiss) with a video camera (Grasshopper[®]3, Point Grey Research Inc.) to visualize and record the contact interface (Figure 4.12). The reaction forces between an adhesion system and a substrate were measured by high-resolution load cells (GSO-25, GSO-500, and GSO-1K, Transducer Techniques[®]). The load cell was attached on a computer-controlled high-precision piezo motion stage (LPS-65 2, Physik Instrumente GmbH & Co. KG) in z-direction, with a resolution of 5 nm and the maximum velocity of $10 \text{ mm} \cdot \text{s}^{-1}$. A long ranged motor stage (M-605 2DD, Physik Instrumente GmbH & Co. KG) was employed for y-direction with 1 μm resolution and high maximum velocity up to 50

$\text{mm} \cdot \text{s}^{-1}$. The substrate was fixed onto a sample holder within the focal range of the microscope and moved in x-direction by the piezo stage (LPS-65 2, Physik Instrumente GmbH & Co. KG). Also, fine positions in x- and y-direction were determined by a manual xy-stage (NFP-2462CC, Positionierungstechnik Dr. Meierling). Angular misalignments were adjusted by two goniometers (M-GON65-U, Newport) according to the substrate. A syringe pump (LegatoTM 210P, KDScientific Inc.) with an accuracy of 0.35% was employed for pressure control inside of the adhesion system. The motion of the piezo stages and the data acquisition were performed by a customized code in Linux (UbuntuTM, Canonical Ltd.). The program allowed automated data acquisition and enabled the user to control velocities, preloads, displacements in x and z directions, and contacting time. The load cell was connected to the computer via a signal conditioner (BNC-2110, National Instruments) and the force signal was exported as a voltage through a data acquisition board (PCIe-6259, National Instruments). Motion control of the piezo stages was conducted through a motor controller (Nexact[®] E-861, Physik Instrumente GmbH & Co. KG).

4.5.2 Characterization of adhesion stress of a single fiber and small area of micro-fiber arrays on the FAM for the soft adhesion system

Estimation of adhesion stress of a single fiber ($\sigma_{\text{ad}}|_{\text{sf}}$) and small area of micro-fiber arrays ($\sigma_{\text{ad}}|_{3\text{f}}$) follow the experimental procedure for the FAM. Three samples (SPL) are taken from different areas of the FAM of the soft system. Each sample has three micro-fibers and is attached to a flat glass slide to measure the adhesion as shown in Figure 4.13b. The 4 mm radius glass indenter is large enough for the three micro-fibers to make full contact and detach at the same time. The pull-off force of the three micro-fibers (F_{off}) is divided by the number of fibers and estimated as the pull-off force of a single fiber ($F_{\text{off}}|_{\text{sf}}$). Each sample is measured 5 times with 1 mN of preload (F_{re}).

Real contact areas of three micro-fibers (A_{rc}) on each sample are measured using the 3D confocal laser microscope as shown in Figure 4.13a, and the real contact area of a single fiber ($A_{\text{rc}}|_{\text{sf}}$) is estimated by dividing the measured area with the number of fibers. Projected

contact areas of the three micro-fibers (A_{pc}) are estimated using the conventional image processing software (ImageJ, NIH Image), including spacing among the micro-fibers in addition to the real contact area (A_{rc}). Adhesion stresses of a single fiber and the three micro-fibers are calculated by dividing each adhesion with the estimated contact areas. Summary of the above measurements is shown in Table 4.1.

Table 4.1: $F_{\text{off}}|_{\text{sf}}$, $A_{\text{rc}}|_{\text{sf}}$, $\sigma_{\text{ad}}|_{\text{sf}}$ and $\sigma_{\text{ad}}|_{3f}$ of micro-fiber array

Sample	F_{off} [mN]	A_{rc} [μm^2]	A_{pc} [μm^2]
SPL #1	1.8	12787	20687.3
SPL #2	2.1	13451.3	20586.1
SPL #3	1.7	12552	21025.9
AVG.	1.9	12930.1	20766.4
$F_{\text{off}} _{\text{sf}}$ [mN]			0.6
$A_{\text{rc}} _{\text{sf}}$ [μm^2]			4310
$\sigma_{\text{ad}} _{\text{sf}}$ [kPa]			145.4
$\sigma_{\text{ad}} _{3f}$ [kPa]			90.5

4.5.3 Characterization of the work of adhesion and adhesion stress of the FAM

Experimental methods for estimation of effective work of adhesion (ω_{ad}) of the FAM and its adhesion stress (σ_{ad}) have been standardized in several previous works based on Johnson, Kendall and Roberts (JKR) theory [102]. Profiles of the reaction force (F_r) for a micro-fiber array on the FAM for both rigid and soft systems are shown in Figure 4.14 with respect to vertical displacement (z). In order to rule out deformation of the soft PDMS backing during the measurements, the FAM is placed on a flat glass substrate and fixed. A 4 mm radius (R) spherical glass indenter is brought down in contact with the FAM at an approach speed of $100 \mu\text{m} \cdot \text{s}^{-1}$. The origin of z is set on the surface of the FAM, and positive z causes compression while negative z causes tension. A 100 mN of preload (F_{pre}) is applied by putting the spherical indenter down to the FAM. Here, we have 30 seconds of relaxation time to minimize unpredictable viscoelastic behavior of the elastomeric micro-fibers, which

causes a slight decrease in reaction force profile. The indenter is pulled up with $50 \mu\text{m} \cdot \text{s}^{-1}$ of retraction speed, which is the same speed used for the experimental measurements. The pull-off force of the micro-fiber array is measured at five different positions on the FAM; top, center, bottom, left, and right. The work of adhesion of the micro-fiber array on the FAM can be evaluated by the following relation between the work of adhesion and pull-off force based on JKR theory,

$$\omega_{\text{ad}} = 2F_{\text{off}}/3\pi R. \quad (4.11)$$

Among the five measurements, three cases whose shape of contact is the most circular are selected in evaluating the projected contact area for the calculation in Equation 4.11. The contact areas of those measurements are estimated from the still images at the instance of the fiber array pulling off from the surface using a conventional image processing software (ImageJ, NIH Image). Summary of the measurements in the pull-off force, along with the estimated work of adhesion and adhesion stress are shown in Tables 4.2 and 4.3.

Table 4.2: Summary of F_{off} , ω_{ad} and σ_{ad} of the FAM for the rigid adhesion system

Position	F_{off} [mN]	A_{pc} [mm ²]
Top	66.3	
Center	82.1	
Bottom	80.6	0.78
Left	82.4	0.78
Right	78.8	0.76
AVG.	78.0	0.77
ω_{ad} [J · m ⁻²]		4.1
σ_{ad} [kPa]		100.8

4.5.4 Characterization of the Soft Adhesion System

The rigid system does show some benefit from a negative pressure differential in increasing interfacial bonding strength. However, a fully soft adhesion system exhibits an even more dramatic improvement by overcoming some of the limitations, when applying a

Table 4.3: Summary of F_{off} , ω_{ad} and σ_{ad} of the FAM for the soft adhesion system

Position	F_{off} [mN]	A_{pc} [mm ²]
Top	105.8	
Center	41.6	0.84
Bottom	55.1	
Left	68.0	0.87
Right	38.3	0.86
AVG.	61.8	0.86
ω_{ad} [J · m ⁻²]		3.3
σ_{ad} [kPa]		72.5

high negative pressure differential for various non-planar 3D geometries. As shown in Figure 4.2b-I, the deformation of the soft chamber eliminates the unfavorable air pocket, allowing over -50 kPa of high negative pressure differentials for all examined substrates 15 mm, 30 mm, 60 mm in diameter glass spheres, a flat glass, and a soft elastomeric film with 400 μm thickness made out of Ecoflex[®] 00-30 (Smooth-On Inc.). This is approximately 10 times greater than the highest negative initial pressure possible with the rigid system. In particular, the FAM on the soft adhesion system remains in contact and enhances the adhesion to the 15 mm diameter glass sphere with a 70 times larger negative pressure differential.

The FAM of the soft adhesion system is less adhesive than that of the rigid system, which exhibits an effective work of adhesion and adhesion stress of 3.3 J · m⁻² and 73 kPa, respectively (Figure 4.14a and Table 4.3). Figure 4.15b shows the pull-off force (F_{off}) measurements of the soft adhesion system as a function of different initial pressures (ΔP_o). In general, the pull-off force increases with ΔP_o and converges to a maximum when the pressure is between -40 kPa and -50 kPa. However, 90% of this maximum pull-off force can be achieved with a pressure differential of roughly -35 kPa. On the flat glass, the pull-off force of the soft adhesion system is increased by 5.4 times compared to the force without a high negative pressure differential. Of particular interest is the superior performance shown for highly-curved 3D geometries like the 15 mm diameter glass

sphere, for which the pull-off force could be improved by 6.7 times. Even on deformable and stretchable substrates, where the FAM and many other adhesives easily peel off, the soft system could remain in contact under the high negative pressure differential and improve the pull-off force by 7.2 times.

Figure 4.15c shows conversion ratios ($\sigma_{ad}/\Delta P_o$) of the soft adhesion system on different substrates, defined as percentages of the adhesion stress (σ_{ad}) normalized by the applied initial pressure (ΔP_o). The soft adhesion system exhibits high conversion ratios at low negative pressure differentials, as the micro-fibers on the FAM can still exert some adhesion without relying on the pressure differential. It shows even higher than 100% of the conversion ratio on 15 mm diameter spherical glass at -10 kPa. At high negative pressure differentials, on the other hand, the conversion ratios decrease significantly, when the system cannot achieve the adhesion as high as the applied negative pressure differential. Among the different diameter of spherical glasses, the smaller sphere shows higher conversion ratios. In case of the same contact areas between the 60 mm diameter sphere and flat glass, the flat surface shows superior conversion ratios to the curved substrate. In general, the soft adhesion system can achieve approximately 30–50% of the conversion ratio at -35 kPa of the initial pressure on glass. However, these values are highly dependent on the adhesiveness of the membrane. As already shown in Figure 4.15b, the soft adhesion system cannot achieve as high of an adhesion on the rubber film as it does on the glass substrates, with a conversion ratio well below 20% for all initial pressures. This leads us to the conclusion that the conversion ratios on the glass substrates would be higher if a more adhesive membrane was employed. Therefore, the maximum allowable adhesion of our adhesion systems is fundamentally limited by the maximum adhesion strength of the fiber-surface contact interface. Nonetheless, negative pressure differential will change how the interfacial load is distributed among the micro-fibers in contact with the surface and enhance adhesion performance within the limits of what the total sum of the contacts can support.

Previous micro-scale contact experiments have revealed that micro-fibers with optimized tip-shapes show greater pull-off force due to equal load sharing, characterized

by longer retraction distances for detachment accompanied with a fast crack propagation [1, 40, 42, 43, 103]. Our soft system achieves similar characteristics at the macroscale with 4 orders of magnitude larger contact area by improving the load sharing. Unlike the short retraction that accompanies the higher pull-off force of the rigid system, Figure 4.15a shows that our soft system could increase the pull-off force while delaying the detachment with a negative pressure differential. Figure 4.15d, 4.15e and 4.15f show schematics, side-view and microscopic images of the soft system on flat glass interface, respectively. In the absence of the negative pressure differential, no collapse of the soft chamber occurs and the FAM experiences high stress concentration at the contact edge (Figure 4.15d-I). This induces slow peeling from the interface (Figure 4.15e-II) during a short retraction distance of 8 mm (Figure 4.15a and Figure 4.15e-I). On the contrary, the soft chamber collapses and strongly suppresses the peeling of the FAM at a high negative pressure differential, allowing the soft system to remain in contact for a 3 times larger retraction distance (Figure 4.15f-I). At the moment when the soft system is pulled off, the extremely large stretch of the soft chamber causes a shear force higher than the critical shear stress, peeling is induced, and the FAM starts detaching from the contact edge (Figure 4.15d-II). Since the equal load-sharing interface can withstand high tensile forces, small loss in contact area can trigger an immediate detachment of the entire FAM (Figure 4.15f-II). In this case, the crack propagation is roughly 110 times faster than without a negative pressure differential, strongly indicating the significant influence of equal load sharing. Within the range of negative pressure differentials allowed by our experimental setup, the FAM for the soft system always detaches from the contact edge. As shown in Figure 4.15g, however, a similar amount of the negative pressure differential could cause a crack propagation initiated at the center when we used a less adhesive FAM (effective work of adhesion and adhesion stress of $3.1 \text{ J} \cdot \text{m}^{-2}$ and 56 kPa, respectively). The results in Figure 4.15e, 4.15f, and 4.15g show that our soft adhesion system is able to manipulate crack initiation by changing the load distribution over a large area with the controlled pressure differential, as theoretically expected in our analysis shown in Figure 4.8.

Direct comparison of the pull-off force between the soft and rigid adhesion systems cannot be made, as the FAMs on two systems have different effective works of adhesion. In order

to compare the performance of the rigid and soft systems with respect to load sharing, we employ the adhesion efficiency (ε_{ad}), which is defined as the percentage of the adhesion stress of an adhesive system normalized by that of the micro-fiber array on the FAM. If a load is equally shared over the entire interface until detachment, the adhesive system will reach the maximum adhesion stress of the micro-fiber arrays (i.e., $\varepsilon_{\text{ad}} = 100\%$). The rigid adhesion system could achieve only 6.6% of the maximum adhesion efficiency on the flat glass surface under a negative pressure differential. If no air is removed from the chamber, then the efficiency drops down to 1.8% on a 60 mm diameter glass and the interface readily fails. The soft adhesion system, on the other hand, can utilize up to 19.5% adhesion efficiency on the flat glass. The system is even more effective for small and highly curved geometries where a full contact is not established. The maximum adhesion efficiency was approximately 25.7% on a 15 mm diameter glass, which is 14 times larger than the rigid adhesion system efficiency without the pressure control on non-planar surfaces.

More detailed information on the characterization results of the rigid and soft adhesion systems are presented in Tables 4.4 and 4.5, respectively. The maximum pull-off force ($F_{\text{off}}|_{\text{max}}$) is the highest value on a given geometry on different initial pressures, while the minimum pull-off force ($F_{\text{off}}|_{\text{min}}$) is the lowest pull-off force among measurements. The contact area (A_c) of the soft system is visually evaluated from the top-side through the transparent chamber. The contact area of the rigid system on non-planar geometries could not be visualized neither from the top nor the side. Therefore, the contact area on large objects, such as 60 mm of d_b glass sphere and flat glass are assumed to have the full contact of 1.7 cm² with the effective contact radius $r_e = 7.3$ mm. Note that the adhesion efficiency (ε_{ad}) of the soft system on the rubber film is not available, since the adhesion stress (σ_{ad}) of the FAM we tested is only valid on the interface between the PDMS-made fiber and glass substrate.

In Figure 4.1, the reversible load sharing mechanism of the soft adhesion system is demonstrated as a soft adhesive pick-and-place gripper, enabling manipulation of various objects with complex 3D and deformable geometries. Our soft adhesion system could conform to a convex (Figure 4.1b) or a concave curvature (Figure 4.1c), and provide a sufficiently

high payload to support over 300 grams with 2.5 cm^2 of contact area (Figure 4.1a). In Figure 4.1d, the soft system can increase the adhesion on a highly curved geometry smaller than the FAM and lift up a weight as much as it could with the full contact in Figure 4.1b and 4.1c. Unlike geckos biological foot-hairs, synthetic micro-fibers are highly sensitive to surface roughness [65], requiring very smooth surfaces like glass for high adhesion. However, the soft system can enhance the weak adhesion of the micro-fibers on slightly rough surfaces such as cherry tomatoes (Figure 4.1e). The soft adhesion system is also successful for handling soft and deformable surfaces, which would not be possible for controllable adhesion mechanisms based on stiffness-tunable materials [73, 74]. As shown in Figure 4.1f, the soft system remains in contact even when the object is deformed and effectively preserves the adhesive attachment during manipulation.

Table 4.4: Characterization results of the rigid adhesion system

Parameters	d_b 15 mm	d_b 30 mm	d_b 60 mm	Flat Glass
A_{pc} [cm^2]	N/A	N/A	1.7	1.7
Highest ΔP_o , $\Delta P_o _h$ [kPa]	2.0	2.7	1.6	1.6
Lowest ΔP_o , $\Delta P_o _l$ [kPa]	-0.7	-4.1	-3.2	-2.9
Min. F_{off} , $F_{off} _{min}$ [N]	0.13	0.12	0.30	0.52
Max. F_{off} , $F_{off} _{max}$ [N]	0.15	0.62	0.88	1.12
$F_{off} _{max}/F_{off} _{min}$	1.2	5.0	3.0	2.2
Min. σ_{ad} , $\sigma_{ad} _{min}$ [kPa]	N/A	N/A	1.2	2.0
Max. σ_{ad} , $\sigma_{ad} _{max}$ [kPa]	N/A	N/A	3.5	4.4
Min. ε_{ad} , $\varepsilon_{ad} _{min}$ [%]	N/A	N/A	1.8	3.1
Max. ε_{ad} , $\varepsilon_{ad} _{max}$ [%]	N/A	N/A	5.2	6.6

4.6 Discussion

An ideally scaled up macroscale adhesion system would have no loss in adhesive force compared to their micro-scale counterparts. Equal load sharing plays a critical role in approaching ideal bonding conditions and maximizing load capacity over a prescribed contact area (A_c) [63]. Geckos have been used as a benchmark to judge the scaling efficiency of man-made adhesion systems [22, 72]. While shear stress (σ_{sr}) of the geckos

Table 4.5: Characterization results of the soft adhesion system

Parameters	d_b 15 mm	d_b 30 mm	d_b 60 mm	Flat Glass	Rubber Film
A_{pc} [cm ²]	0.6	1.5	2.5	2.5	2.5
Highest ΔP_o , $\Delta P_o _h$ [kPa]	1.5	0.6	3.6	1.7	0.3
Lowest ΔP_o , $\Delta P_o _l$ [kPa]	-51.0	-50.7	-52.1	-51.7	-50.9
Min. F_{off} , $F_{off} _{min}$ [N]	0.18	0.42	0.49	0.66	0.08
Max. F_{off} , $F_{off} _{max}$ [N]	1.18	2.70	2.91	3.61	0.61
$F_{off} _{max}/F_{off} _{min}$	6.7	6.4	6.0	5.4	7.2
Min. σ_{ad} , $\sigma_{ad} _{min}$ [kPa]	2.8	2.8	1.9	2.6	0.3
Max. σ_{ad} , $\sigma_{ad} _{max}$ [kPa]	18.7	18.1	11.4	14.2	2.4
Min. ε_{ad} , $\varepsilon_{ad} _{min}$ [%]	3.9	3.9	2.6	3.6	N/A
Max. ε_{ad} , $\varepsilon_{ad} _{max}$ [%]	25.7	25.0	15.8	19.5	N/A

adhesion system, from bonding of a single seta to the attachment of two feet, has been reported to follow a scaling power law $\sigma_{sr} \propto A_c^{-0.24}$ on a flat glass surface [104], no conclusive estimate is available on the scaling law for pure normal adhesion stress (σ_{ad}), as adhesion of the gecko is strongly coupled with friction. Labonte *et al.* has recently reported that the geckos scaling trend in adhesion coupled with shear forces is very similar to its scaling in shear stress for a range from the seta to the animal level [105]. Therefore, we took the scaling of the gecko in the shear direction as a standard to evaluate the scaling performance of our adhesion system in the adhesion stress, assuming the gecko would have similar scaling efficiencies in both lateral and normal directions.

The adhesion stresses of a single fiber, a micro-fiber array, and our soft adhesion system on different sizes of spherical and flat glass substrates are plotted with the shear stress of the gecko foot-hairs, as shown in Figure 4.16. Estimation of the adhesion stress of the single fiber and the micro-fiber arrays with a small contact area are detailed in Figure 4.13 and Table 4.1. The scaling relation between the single fiber and the micro-fiber array, which are fixed on a rigid backing, is estimated as a power law of $\sigma_{ad} \propto A_c^{-0.12}$ by the least squares method, indicated as the green dashed line. This scaling relation provides a theoretical upper limit of the scaling efficiency that an adhesion system with the fibrillar adhesives could achieve at maximum.

Unlike the case of single fiber and micro-fiber array on a rigid backing, the adhesion stress of the compliant FAM on our soft load sharing system deviates from the linear trend of the theoretical maximum due to a significant loss in fracture strength by introducing stress concentration. The dashed red and blue lines in Figure 4.16 show the scaling trends of our soft system from the single fiber, micro-fiber array, and overall soft system calculated by the least squares method. Without a negative pressure differential (the red line in Figure 4.16), the stress concentration results in a poor scalability of $\sigma_{\text{ad}} \propto A_c^{-0.41}$. Under a high negative pressure differential (the blue line in Figure 4.16), on the other hand, our soft load sharing system can minimize the stress concentration with the same compliant membrane and improves the scaling efficiency by recovering it up to $\sigma_{\text{ad}} \propto A_c^{-0.21}$, which is slightly higher than that of the gecko on various flat and curved 3D surfaces.

Hawkes *et al.* developed a synthetic adhesion system [22] with the scaling efficiency related to $\sigma_{\text{ad}} \propto A_c^{-0.02}$ for the shear stress on flat or slightly curved surfaces. Our soft adhesion system is the first man-made adhesion system having geometry-insensitive load sharing with an area scaling efficiency that is comparable to that of the natural geckos adhesion system. Therefore, the concept of our soft adhesion system can provide significant benefits in a broad range of adhesion applications requiring high adhesion on various sizes of 3D surfaces. This includes transfer printing systems [25, 26, 27, 28] and robotic manipulators [29] capable of handling a wide range of sizes and curvatures of rigid and deformable substrates as well as mobile robots that can climb on complex 3D surfaces, such as aircraft, space shuttle, or pipe surfaces [30, 31, 32].

4.7 Summary

We present a soft load sharing system that controls normal load distribution on 3D surfaces by exploiting the influence of internal pressure on interfacial load sharing. This soft system architecture addresses the fundamental challenge of having high surface conformability while simultaneously maintaining high fracture strength. By utilizing a soft and deformable body and controlling the negative pressure differential acting on the interface,

the proposed system pushes the upper limit on the maximum adhesion-controlled gripping strength that can be achieved on non-planar 3D geometries. Our equal load sharing method represents a new paradigm for adhesion-based systems that outperform previous micro-fibrillar adhesives in handling complex 3D and deformable objects and surfaces.

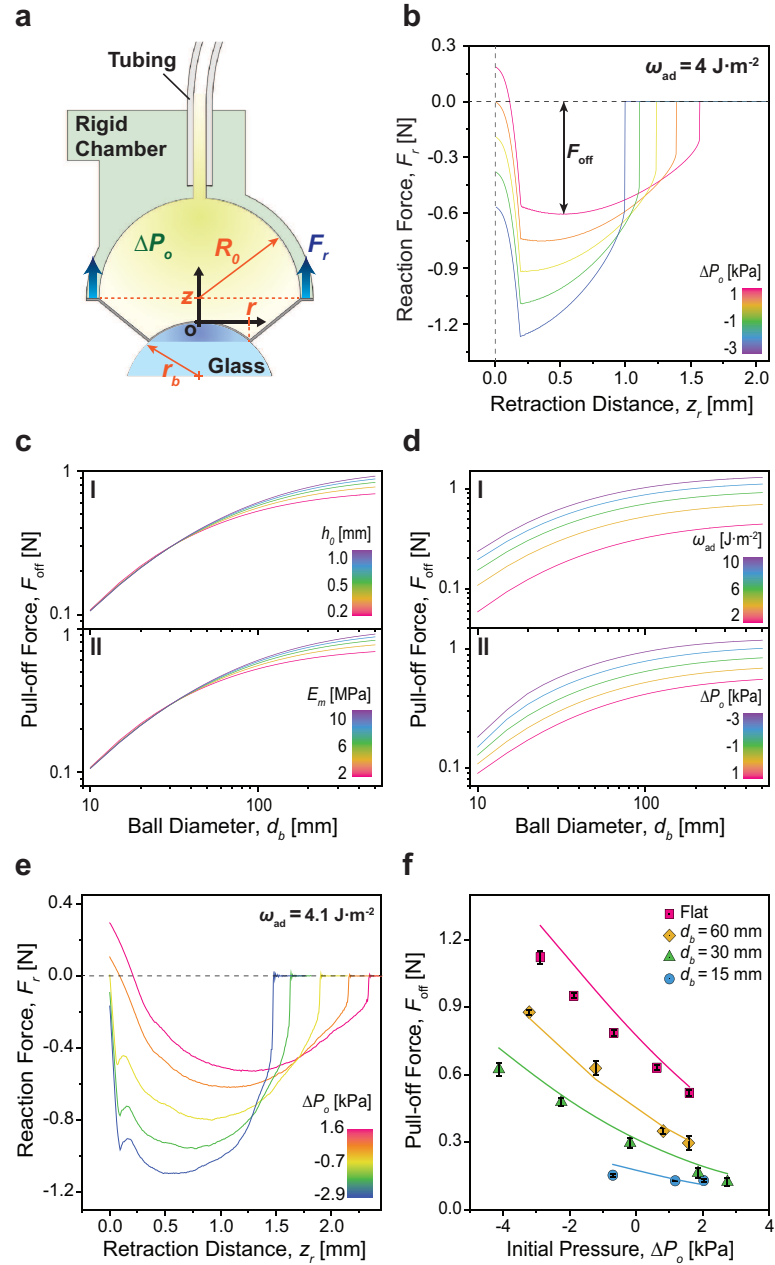


Figure 4.9: Analysis and force measurements in the rigid adhesion system for different 3D geometries. (a) A schematic of the rigid adhesion system being pulled off from a spherical substrate under a negative pressure differential (ΔP_o). Blue arrows indicate the direction of reaction force (F_r). (b) Calculated reaction force (F_r) profiles on a flat glass surface versus retraction distance (z_r) for various initial pressures (ΔP_o). (c) Calculated pull-off force (F_{off}) as a function of the diameter (d_b) of glass spheres for varying thicknesses (h_0) (I), and Young's moduli (E_m) (II). (d) Calculated pull-off force (F_{off}) as a function of diameter (d_b) of the glass sphere for varying works of adhesion (ω_{ad}) (I) and initial pressures (ΔP_o) (II). In all of these plots, the default parameter values are $h_0 = 0.2 \text{ mm}$, $E_m = 2.1 \text{ MPa}$, $\omega_{ad} = 4.0 \text{ J}\cdot\text{m}^{-2}$, and $\Delta P_o = 0 \text{ kPa}$. (e) Measured reaction force profiles on a flat glass surface with respect to retraction, depending on different initial pressures. (f) Measured pull-off forces on glass substrates with different curvatures depending on the initial pressures. Each point indicates an average of 5 measurements, and error bars are 1 SD (standard deviation).

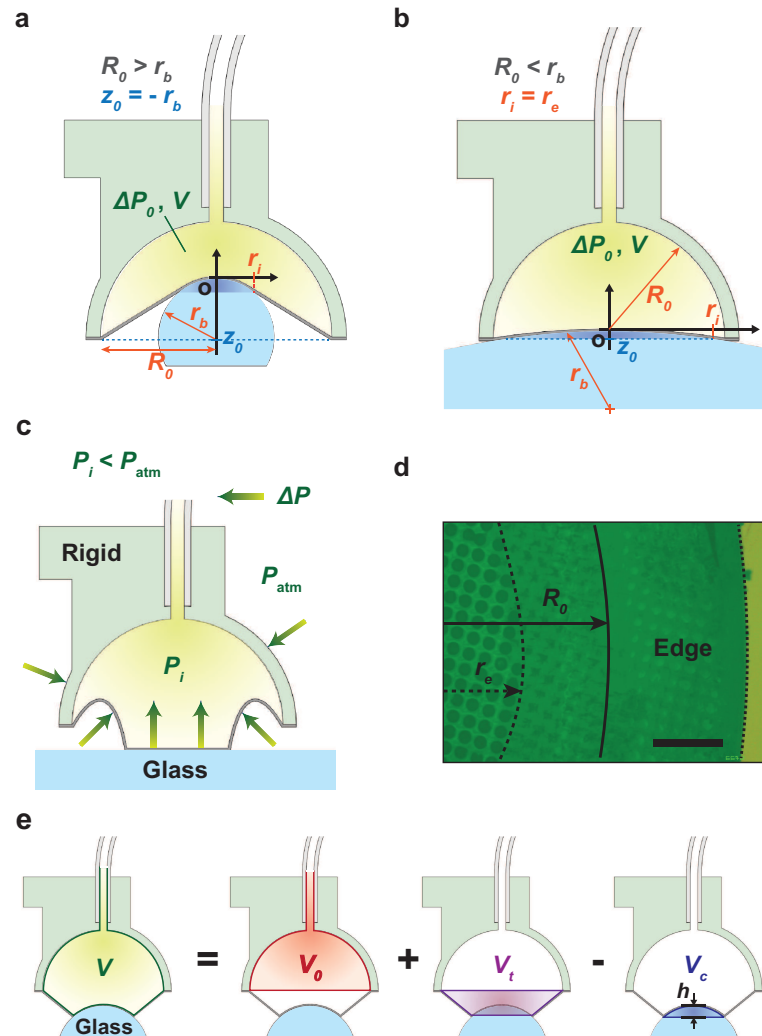


Figure 4.10: Schematics of the analytical model for the rigid adhesion system with different boundary conditions. (a) A schematic of the rigid adhesion system in contact bigger than a spherical substrate. (b) A schematic of the contacting rigid adhesion system with a diameter that is smaller than that of the spherical substrate. (c) A schematic of the rigid adhesion system being delaminated from a flat glass substrate under a negative pressure differential (ΔP). Green arrows show the forces caused by the pressure differential acting on surface of the adhesion system, which can pull the FAM into the rigid chamber and cause delamination of the membrane. (d) An inverted optical microscope image of the FAM on the rigid adhesion system in contact with a flat glass substrate, visualizing the contact interface. Dark areas indicate micro-fibers on the FAM in contact. The scale bar is 500 μm . (e) A schematic of the total volume (V) as a sum of the initial volume (V_0) and the additional volume created by the truncated-cone shaped deformation of the FAM (V_t), subtracted by the volume of the spherical substrate covered by the FAM (V_c). h_c is the height of the spherical cap (V_c).

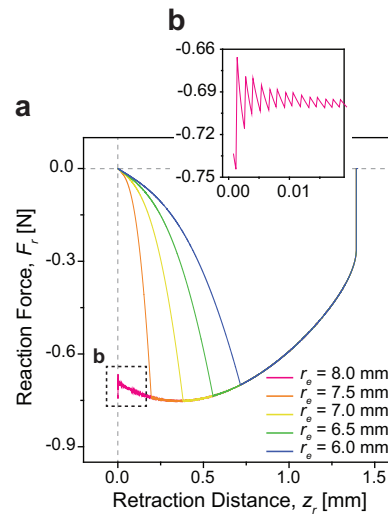


Figure 4.11: (a) Calculated reaction force (F_r) profiles on a flat glass surface with respect to retraction distance (z_r), depending on effective contact radius (r_e). Here, the difference in the effective contact radius represents the difference in the initial contact area. (b) A magnified view for the reaction force profile in the beginning of retraction when $r_e = 8.0$ mm. Small numerical instabilities can be observed in the beginning of retraction when $r_e = R_0$. The first derivatives of the total potential energy (Π) with respect to vertical displacement (z) and contact radius (r) are numerically obtained using the forward ($r_e = R_0$), centered ($0 < r_e < R_0$), and backward ($r_e = 0$) difference approximations. Here, the vertical displacement and contact radius are discretized in 20,001 and 50,001 elements, respectively.

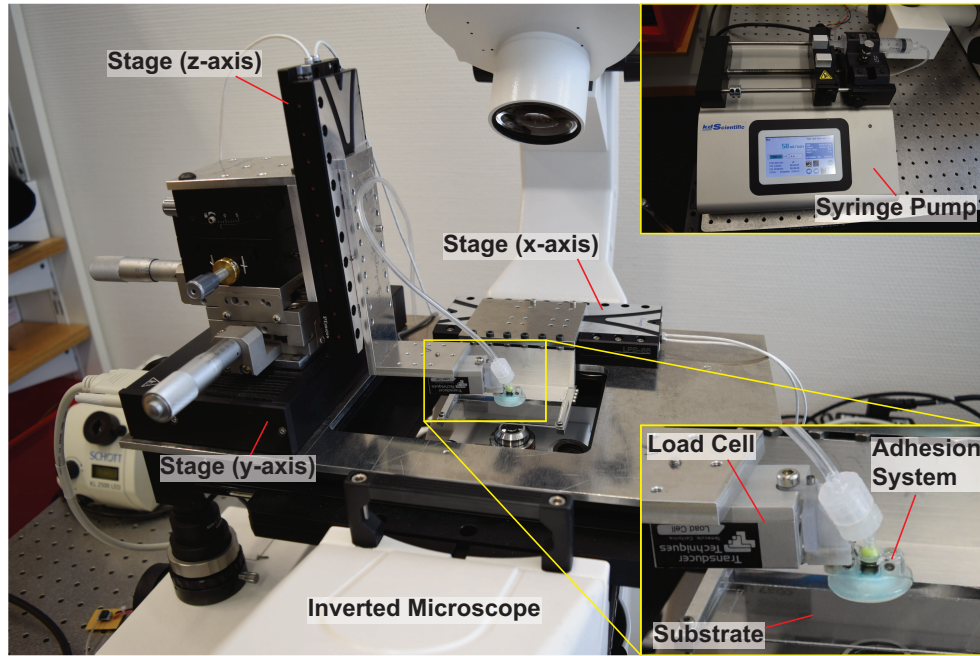


Figure 4.12: Customized experimental setup for characterization of adhesion systems.

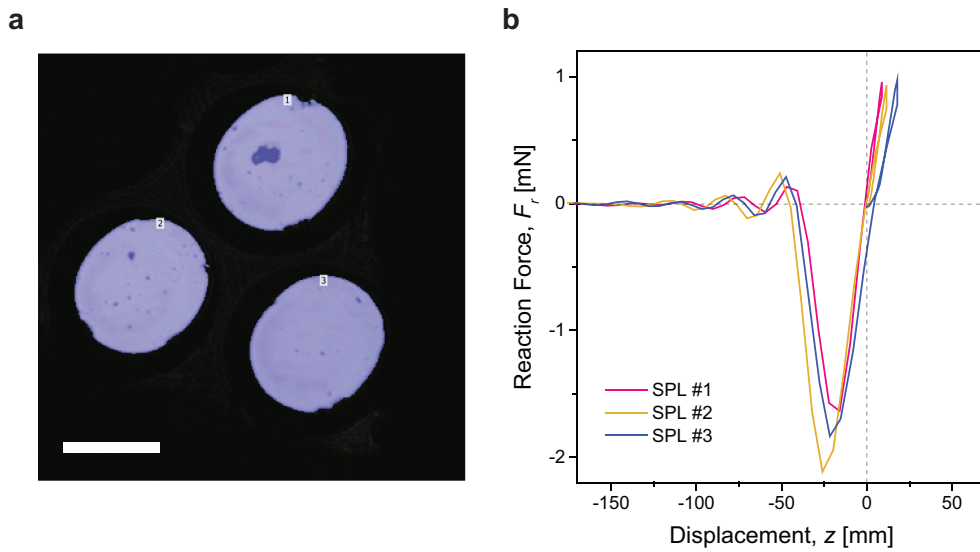


Figure 4.13: Characterization of adhesion stress (ad) of a single micro-fiber on the FAM for the soft adhesion system. (a) Visualization of the contact area of three micro-fibers for each samples using the confocal laser microscope. Scale bar = 100 μm . (b) Reaction force (F_r) profiles of three micro-fibers for each sample.

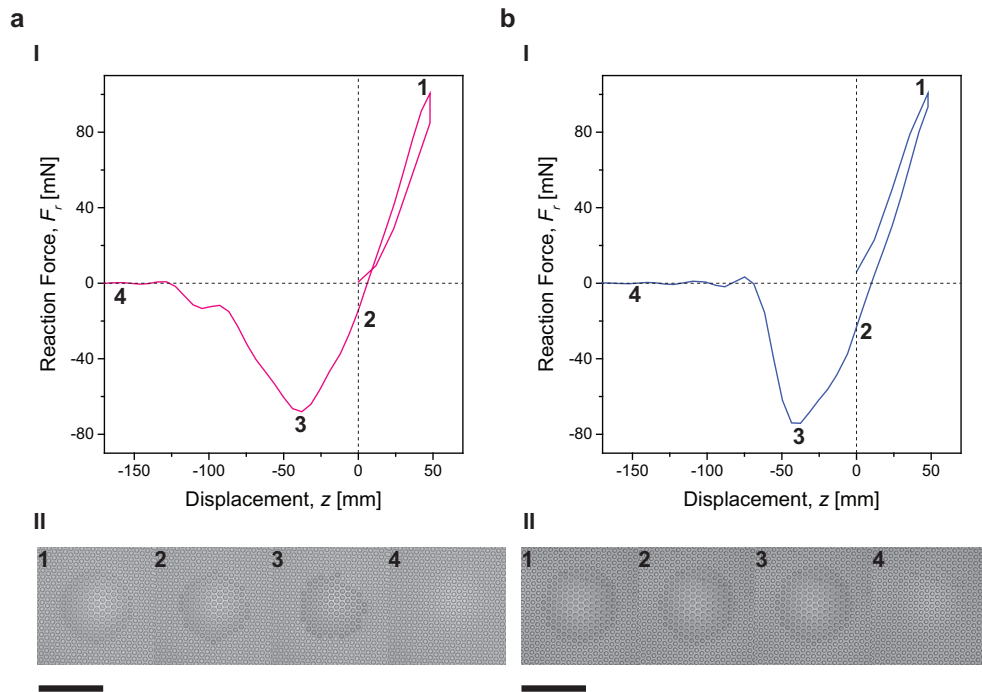


Figure 4.14: Characterization of the effective work of adhesion (ω_{ad}) and adhesion stress (σ_{ad}) of the FAM for rigid and soft adhesion systems. (a) A reaction force (F_r) profile of the FAM for the soft system (I), in accordance with microscopic images on the interface (II). (b) A reaction force (F_r) profile of the FAM for the rigid system (I), in accordance with microscopic images on the interface (II). 1: preloading, 2: retracting, 3: exerting pull-off force, 4: detached. Scale bars indicate 1 mm.

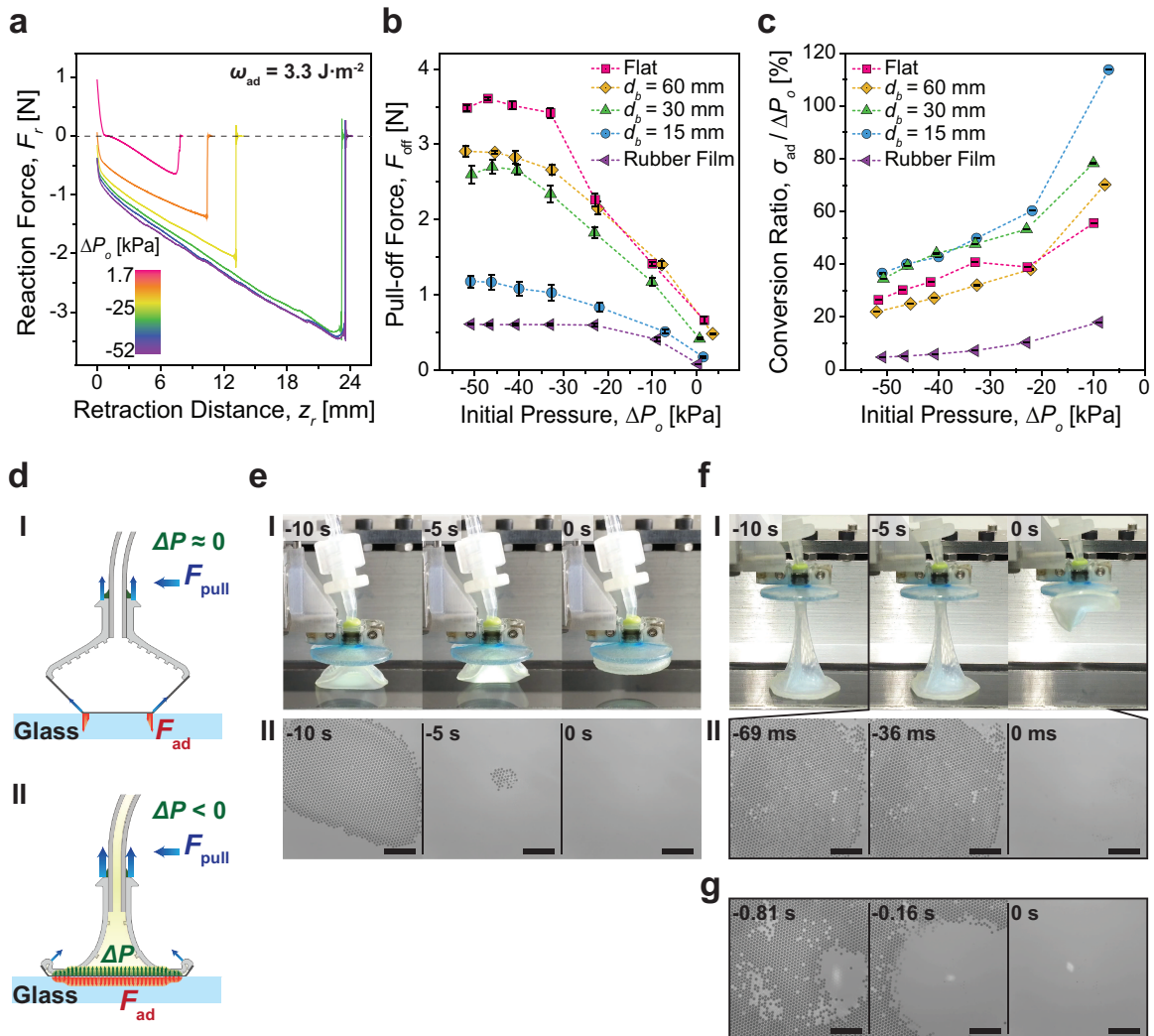


Figure 4.15: Characterization results of the soft adhesion system. (a) Measured reaction force (F_r) profiles on a flat glass surface with respect to retraction, depending on different initial pressures (ΔP_o). (b) Measured pull-off forces (F_{off}) on various substrates depending on the initial pressures. (c) Conversion ratio ($\sigma_{ad}/\Delta P_o$) on various substrates as a function of initial pressure. Each point in (b) and (c) indicates an average of 5 measurements, and error bars are 1 SD. (d) Schematics of the soft system being pulled off from the flat glass without a change in the internal pressure (P_i) (I), and under a high negative pressure differential (II). (e) Side-views of the soft system being pulled off from the flat glass at 1.7 kPa of the initial pressure (I), and corresponding microscopic images of the contact interface (II). The estimated crack propagation speed is $1.5 \text{ m} \cdot \text{s}^{-1}$. (f) Side-views of the soft system being pulled off from the flat glass at -52 kPa of the initial pressure (I), and corresponding microscopic images of the contact interface (II). The estimated crack propagation speed is $179 \text{ m} \cdot \text{s}^{-1}$. (g) Microscopic images of the contact interface of the soft system with a less adhesive FAM being pulled off from the flat glass at -46 kPa of the initial pressure. Scales in (e-II), (f-II) and (g) indicate 1 mm. The moment at which the FAM is detached is set to be zero seconds (0 s).

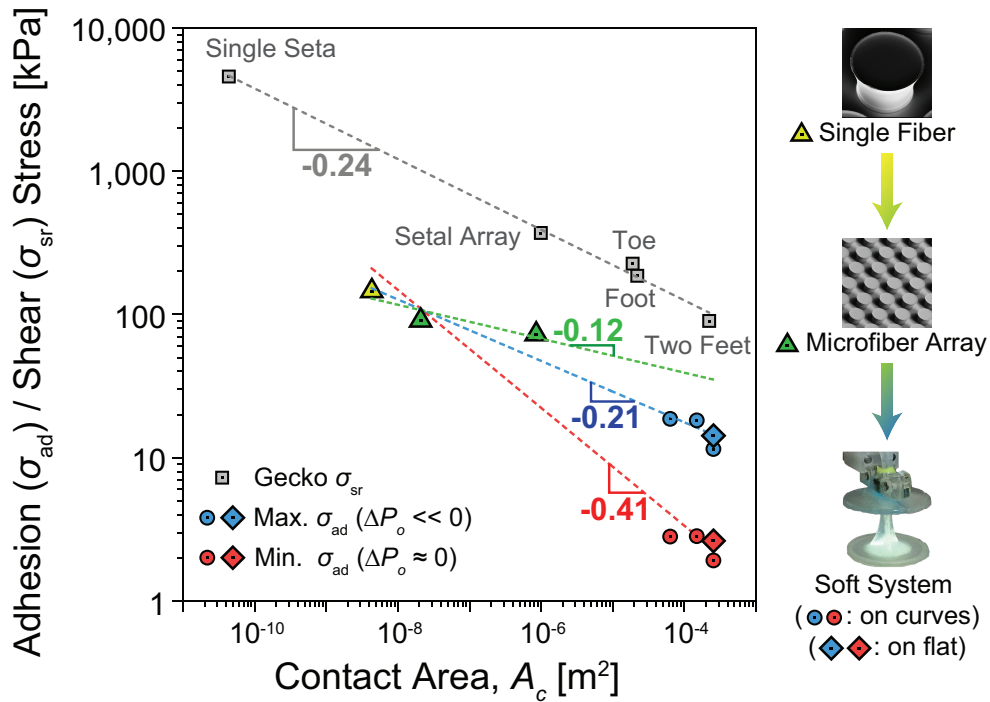


Figure 4.16: Scaling of the soft adhesion system compared to a flat micro-fiber array and biological gecko adhesives. The scaling of gecko foot-hair adhesion is for shear stress (σ_{sr}) on a flat substrate, while the other results in the soft system are for normal adhesion stress (σ_{ad}) on both 3D curved (circles) and flat surfaces (rhombuses). Dashed lines are the least-squares trends in the adhesion stress of a single fiber, the micro-fiber array, and the soft system measured on the both flat glass and spheres with 15, 30, and 60 mm diameters with (blue) and without (red) a negative initial pressure. The green line is the scaling from the single fiber to the micro-fiber array. Each data point indicates an average of 5 experimental measurements.

Chapter 5

Conclusions and Outlook

This thesis work has investigated principles and knowledge on load distribution and its control for gecko-inspired micro-fibrillar adhesive interfaces in multi-scale, and applied the findings to develop a soft robotic gripper for grasping a wide range of complex non-planar three-dimensional (3D) objects. By exploiting an emerging nano-fabrication technique, this work could perform a series of systematical experiments to verify an existing theory for the optimal tip-endings of mushroom-like fibrillar adhesives for the equal load sharing on micro-contacts. Also, the micro-fiber adhesives were manufactured together with a soft membrane backing, which improved the adhesion on various 3D surfaces by summing up high fracture strengths of the mushroom-shaped micro-fibers. However, experiments showed that softness of the membrane is at a high expense of 96% of reduction in the membrane's adhesion due to stress concentration, imposing an inherent dilemma of soft adhesive interfaces between 3D conformability and high fracture strength. This work proposed a soft robotic architecture which reversibly controls load distribution of the membrane-backed micro-fiber array with a pneumatic pressure differential, enabling enhanced and robust adhesion on various complex 3D geometries and deformable surfaces without compromising its 3D conformability.

Detailed contributions of this thesis as well as future works are listed as follows:

5.1 Contributions

- **Shape Optimization of Micro-fibers for Equal Load Sharing:** Mushroom-shaped tip-endings with different tip-to-stalk ratios (β) and wedge angles (θ) have been fabricated using two-photon nano-lithography technique, and casted by two polyurethane elastomers with different Young's modulus. Force measurements exhibited the maximal adhesion with $\beta = 1.4, \theta = 30^\circ$ for soft polyurethane fibers (ST-1060, BJB Enterprises Inc.) and $\beta = 1.2, \theta = 30^\circ$ for rigid polyurethane fibers (ST-1087, BJB Enterprises Inc.), respectively, showing approximate agreements with theoretical expectation ($\beta = 1.1-1.2, \theta = 45^\circ$) in the previous work [43].

Precisely defined micro-fibers by the two-photon nano-lithography enabled systematical investigation on the load distribution of various shapes of micro-fibers depending on different values of β and θ . For example, A higher β results in a smaller slope on force-displacement curve, requiring a longer retraction for pull-off. Moreover, experiments suggested that stiffness of the micro-fibers has significant impacts on the load distribution on the contact interface; while the soft micro-fibers showed relatively similar pull-off forces for different tip-endings, the rigid micro-fibers exhibited very narrow window in β and θ for the maximal adhesion approximately 1.9 times higher than the soft fibers.

For the soft fibers, difference in the pull-off force between the optimal and non-optimal tip-endings was 2.1 times, while the rigid fibers was over 12 times. Also, discrepancies in between the theoretical expectations and experimental results showed that a tiny deviation in the optimal tip-endings with nano-scale rounding edge can results in significant loss in the fracture strength. Combined with the findings in the previous works that nano-scale contacts shows the maximum amount of fracture strength insensitive to fiber geometries [41], this results support why the biological geckos have been evolved in the hierarchical fibrillar foot-hairs made out of rigid keratinous materials branched down to numerous number of nano-contacts.

- **Fibrillar Adhesives on a Membrane for Large-scale 3D Surface Grasping:** For the first time, the fibrillar adhesives on a membrane (FAM) has been fabricated using two different polyurethane elastomers by intergrating the micro-fibers with a soft membrane backing. The mushroom-shaped micro-fibrillar structures were made out of a polyurethane (ST-1060, BJB Enterprises Inc.) with high work of adhesion, while the soft and stretchable membrane backing was fabricated with the other polyurethane (F-25, , BJB Enterprises Inc.), allowing a high stretch up to 230% in area. With force measurements on flat glass, the FAM showed 10 times greater adhesion than an unstructured membrane due to the high fracture strength of the mushroom-like micro-fibers enhanced by the equal load sharing. Benefiting from high conformability of the soft membrane, the FAM also exhibited the biggest payload for non-planar 3D surfaces among the tested specimens, capable of supporting up to 35 grams of spherical objects, while the micro-fibers with a rigid backing and the unstructured membrane could carry only up to 5 grams and 0.13 grams of spherical objects, respectively.

Experimental results in releasing force measurements showed that the FAM can not only enhance the interfacial bond strength on non-planar surfaces, but also can achieve high controllability in adhesion by exploiting membrane stretch during inflation. Through transitioning of membrane configuration from planar to spherical shape, the FAM could utilize stretch of the membrane to detach the micro-fibers in contact, effectively reducing the pull-off force down to 2mN of single fiber-tip adhesion. Peeling behavior through inflation allowed the FAM another degree of freedom in controlling the adhesion for 3D surfaces, exhibiting a high switching ratio up to 204, which is superior to previous works based on the peeling angle control of the fibrillar structures (e.g., 39 [28], 10 [60], and 14.8 [61]).

Simple analytic models were developed to provide the design rules for estimating picking and releasing performances of the FAM depending on various design variables. For analyzing the picking performance, the FAM was assumed to be an

unstructured Neo-Hookean solid with truncated-cone shape deformation. Reaction force profiles during pull-off were calculated based on principle of the minimum potential energy. The developed model exhibited qualitatively good agreements with the experimental measurements, and showed a trade-off between high adhesion and 3D conformability depending on the membrane's thickness/stiffness. For the releasing performance, the analysis showed that the pitch distance between micro-fibers increases when a transition of the FAM configuration from a plane to a spherical shape occurs via inflation, which can cause peeling of the micro-fibers in contact reducing the contact area down to single fiber-tip. The model could provide a rough estimation of stretch requirements to achieve the minimum single fiber adhesion for the given adhesion strength of micro-fibers and pitch-size.

- **Load Distribution Control of a Soft-backed Microfiber Array on 3D Surfaces:** This work proposed a soft load sharing system which addresses a challenge of having high surface conformability while simultaneously maintaining high fracture strength by exploiting the influence of internal pressure on interfacial load sharing. Composed of a gecko-inspired elastomeric fibrillar adhesive on a membrane (FAM) supported by a pressure-controlled deformable gripper body, the soft adhesion system could utilize up to 26% of the maximum adhesion of the FAM under a high negative pressure differential inside of the gripper body with respect to the atmospheric pressure, which is 14 times higher than the adhering membrane without load sharing on 3D surfaces.

The load distribution among micro-fibers was studied by modeling the axi-symmetric array on the FAM with 2D plane-strain linear elasticity. Vertical stress within the FAM when pulling it up from a flat substrate under various pressure conditions was numerically calculated by simplifying the FAM as an incompressible Hookean solid subjected to a vertical displacement corresponding to 5% of the membrane thickness. Results showed that decreasing the pressure leads to a more uniform stress distribution among the fibers, with the vertical stress at the center fiber approaching

or even exceeding the stress at the edge, giving qualitative insights on how negative pressure can be used to control the load distribution within the axisymmetric system.

Influence of internal air pressure on membrane adhesion to non-planar 3D geometries was investigated by adapting our previous analysis based on the principle of minimum potential energy for spherical substrates, which also enabled estimation of the influence of various design parameters to identify conditions that lead to more uniform load sharing control. Findings indicated that, unlike other design variables (e.g., thickness or Young's modulus), negative pressure differential could increase the pull-off force for all spherical geometries, revealing that the pressure differential can be an attractive controllable variable for adhesion tuning which can be easily combined with other pre-existing pneumatic elements for actuating a soft robotic system.

Equal load sharing plays a critical role in approaching an ideal adhesion system with no adhesion loss in macro-scale compared to its micro-scale counterparts. Geckos have been used as a benchmark to judge the scaling efficiency of man-made adhesion systems with an area scalability in adhesion from bonding of a single seta to the attachment of two feet of a power law $\sigma_{sr} \propto A_c^{-0.24}$ on flat glass surface. Despite the FAM is subjected to a poor scalability due to stress concentration, our soft load sharing system could strongly suppress the stress concentration under a high negative pressure differential, and exhibited a geometry-insensitive area scalability up to $\sigma_{ad} \propto A_c^{-0.21}$ in normal adhesion, which is comparable to that of the natural geckos' adhesion system, providing significant benefits in a broad range of robotic applications including transfer printing systems, robotic manipulators, and mobile robots.

5.2 Future Works

- **Shape Optimization of Micro-fibers for Equal Load Sharing:** shape of tip-endings on the load distribution at micro-contact interface showed a great influence on the pull-off forces of the micro-fiber adhesives. Also, the effect became much significant when the micro-fibers has made out of a stiffer elastomer. In combinations with exploiting various smart materials, such as shape memory polymers (SMPs) and liquid crystalline elastomers (LCEs) which can change their shapes by external stimuli (e.g., light or heat), the above findings can be used for micro-manipulations with controllable adhesion based on the shape change of the micro-fiber tip-ending.

All theories [43, 106, 107] and experiments [19, 40] related to the optimal shape of micro-fibers for the maximal adhesion including this thesis work are based on the static condition with extremely slow pull-off velocities down to $1 \mu\text{m} \cdot \text{s}^{-1}$, although significant influences of viscoelastic effects of the elastomeric micro-fibers on pull-off forces have been reported [85] and applied for various pick-and-place manipulations [27, 108]. Development of a new theoretical model being able to take the pull-off velocity into account for the tip optimization as well as experimental validation under dynamic conditions would lead to a chance of new adhesion control mechanisms suitable for the micro-manipulations.

- **Fibrillar Adhesives on a Membrane for Large-scale 3D Surface Grasping:** for systematic evaluations of the FAM's adhesion performance on various 3D surfaces, non-planar geometries have been limited to concave spheres with different radius of curvatures. As a future work, adhesion of the FAM can also be measured on various 3D surface geometries, such as convex curves or saddle-shaped surfaces, and be quantitatively compared to that of the unstructured membrane or micro-fibers on a rigid backing.

The FAM of which an inherently non-sticky elastomer is structured into fibrillar

adhesives provides a clear advantage of being able to be cleaned and re-used repetitively for a long period of time. Various cleaning methods can be implemented with the proposed gripper depending on different robotic applications for a long-term use, ranging from a mobile robot for which the dry cleaning is suitable [90], to a manipulator in factories where the wet cleaning can be found more useful [89].

Not only the cleaning methods, but also the influence of various environmental parameters (e.g., humidity, temperature, and chemical exposure such as organic solvents) on adhesion of the FAM has to be investigated quantitatively in order to expand practical applications of the proposed gripping system under a wide range of different circumstances.

- **Load Distribution Control of a Soft-backed Microfiber Array on 3D Surfaces:** as this thesis work has mainly focused on a propose of soft load sharing system which achieves both high interfacial fracture strength and 3D surface adaptability simultaneously, optimization of structure and material of the system were not attempted. For example, the soft and highly stretchable chamber made out of Ecoflex[®] 00-50 ensured the system's 3D conformability, while a large amount of stretch under a high load caused shear peeling at the edge of contact. A composite made out of a soft elastomer in combination with non-stretchable materials such as fabric or paper would reduce the tensile stress acting on the body of soft chamber during pull-off, which can lead to further improvements.

Also, there has not been an attempt to optimize the performance of our adhesion system for releasing lightweight objects. In our previous work, we leveraged the stretch of a membrane to peel the microfibers in contact, reducing the bonding strength of the FAM down to the adhesion of a single fiber [29]. Combining the proposed soft load-sharing mechanism with the stretchable FAM can provide high load capacity and controllability in adhesion with a controlled pressure differential. Although stiffness of PDMS with high Young's modulus of 2 MPa helps fibers to

avoid of lateral collapse [8], its brittle nature causes mechanical instability when combined with a membrane made out of stretchable materials such as the Ecoflex[®]. A suitable combination of elastomers for micro-fibers and a membrane has to be selected or engineered as a future work.

Although not suitable for deformable substrates, combination of stiffness tuning with micro-fiber adhesives is still interesting and worthwhile to be investigated for alternatives of the proposed soft load sharing system. Various stiffness tunable materials (e.g., liquid metals, SMPs, and LCEs) can be used for a backing substrate of an array of micro-fiber adhesives enabling the control of interfacial load distribution for vacuum environments, such as micro-fabrication tools and space applications. In the atmospheric circumstances, granular jamming could also be an effective way of changing backing stiffness with a fast response. As discussed in the section 1.4, Brown *et al.* have reported that the jamming gripper is based on the mechanisms of suction and mechanical interlocking, providing a high picking force for objects smaller than 90% of the gripper size [54]. Even if the use of micro-fibers may sacrifice a portion of picking force contributed by the suction, the jamming-based adhesive gripping exploiting the combination of the mechanical interlocking and fibrillar adhesion in exerting the picking force would allow the gripper to overcome the aforementioned geometrical restrictions on the object's shape and size.

Facing a long-lasting challenge of synthetic fibrillar adhesives for rough surfaces, the proposed soft load sharing system has been found to be useful in effectively utilizing the micro-fiber adhesives on slightly rough surfaces such as cherry tomatoes. Pull-off force measurements on various roughnesses under a negative pressure differential can be followed as a future work to quantitatively characterize the influence of surface roughness on the performance of the soft load sharing system in improving the adhesion, which can lead to a better design of the system suitable for rough and irregular surfaces.

In our analytic model for the FAM, the structured fibrillar surface has been approximated as a flat surface and the shape of deformation has been simplified as a truncated-cone, even under a reduced internal chamber pressure. Taking the fibrillar structures into account along with more realistic kinematics of the membrane deformation would allow for a more quantitatively accurate predictive model. Such a model represents a potential opportunity for future work. In particular, it could lead to further insights into the contact mechanics of a soft and structured interface and be used in optimized soft system designs for specific applications.

Bibliography

- [1] Hamidreza Marvi, Sukho Song, and Metin Sitti. Experimental Investigation of Optimal Adhesion of Mushroomlike Elastomer Microfibrillar Adhesives. *Langmuir*, 31(37):10119–10124, 2015. 1.7, 2.1, 4.5.4
- [2] Eduard Arzt, Stanislav Gorb, and Ralph Spolenak. From micro to nano contacts in biological attachment devices. *Proceedings of the National Academy of Sciences*, 100(19):10603 – 10606, 2003. 1.1
- [3] N Gravish, M Wilkinson, and K Autumn. Frictional and elastic energy in gecko adhesive detachment. *Journal of The Royal Society Interface*, 5(20):339–348, 2008. 1.1
- [4] Huajian Gao, Xiang Wang, Haimin Yao, Stanislav Gorb, and Eduard Arzt. Mechanics of hierarchical adhesion structures of geckos. *Mechanics of Materials*, 37(23):275 – 285, 2005. 1.1, 1.2
- [5] N.W Rizzo, K.H Gardner, D.J Walls, N.M Keiper-Hrynko, T.S Ganzke, and D.L Hallahan. Characterization of the structure and composition of gecko adhesive setae. *Journal of The Royal Society Interface*, 3(8):441–451, 2006. 1.1
- [6] Metin Sitti and Ronald S. Fearing. Synthetic gecko foot-hair micro/nanostructures as dry adhesives. *Journal of Adhesion Science and Technology*, 17(8):1055 – 1074, 2003. 1.1
- [7] Seok Kim and Metin Sitti. Biologically inspired polymer microfibers with spatulate tips as repeatable fibrillar adhesives. *Applied Physics Letters*, 89(26):261911(1) – 261911(3), 2006. 1.1, 3.4.1
- [8] Burak Aksak, Michael P. Murphy, and Metin Sitti. Adhesion of biologically inspired vertical and angled polymer microfiber arrays. *Langmuir*, 23(6):3322 – 3332, 2007. 1.1, 5.2
- [9] Michael P. Murphy, Burak Aksak, and Metin Sitti. Adhesion and anisotropic friction enhancements of angled heterogeneous micro-fiber arrays with spherical and spatula

- tips. *Journal of Adhesion Science and Technology*, 21(12-13):1281 – 1296, 2007. 1.1, 3.2.1
- [10] Jongho Lee, Ronald S. Fearing, and Kyriakos Komvopoulos. Directional adhesion of gecko-inspired angled microfiber arrays. *Applied Physics Letters*, 93(19):191910(1) – 191910(3), 2008. 1.1
- [11] Seok Kim, Metin Sitti, Tao Xie, and Xingcheng Xiao. Reversible dry micro-fibrillar adhesives with thermally controllable adhesion. *Soft Matter*, 5:3689 – 3693, 2009. 1.1
- [12] Michael P. Murphy, Burak Aksak, and Metin Sitti. Gecko-inspired directional and controllable adhesion. *Small*, 5(2):170 – 175, 2009. 1.1
- [13] Tae-il Kim, Hoon Eui Jeong, Kahp Y. Suh, and Hong H. Lee. Stoooped nanohairs: Geometry-controllable, unidirectional, reversible, and robust gecko-like dry adhesive. *Advanced Materials*, 21(22):2276 – 2281, 2009. 1.1, 4.2
- [14] Boaz Pokroy, Alexander K. Epstein, Maria C. M. Persson-Gulda, and Joanna Aizenberg. Fabrication of bioinspired actuated nanostructures with arbitrary geometry and stiffness. *Advanced Materials*, 21(4):463 – 469, 2009. 1.1
- [15] A. Grinthal, S.H. Kang, A.K Epstein, M. Aizenberg, M. Khan, and J. Aizenberg. Steering nanofibers: An integrative approach to bio-inspired fiber fabrication and assembly. *Nano Today*, 7(1):35 – 52, 2012. 1.1
- [16] Dirk-Michael Drotlef, Peter Blmler, and Arnzazu del Campo. Magnetically actuated patterns for bioinspired reversible adhesion (dry and wet). *Advanced Materials*, 2013. 1.1, 1.4
- [17] Seok Kim, Burak Aksak, and Metin Sitti. Enhanced friction of elastomer microfiber adhesives with spatulate tips. *Applied Physics Letters*, 91(22):221913, 2007. 1.1, 3.4.1
- [18] A. K. Geim, S. V. Dubonos, I. V. Grigorieva, K. S. Novoselov, A. A. Zhukov, and S. Yu. Shapoval. Microfabricated adhesive mimicking gecko foot-hair. *Nat Mater*, 2(7):461 – 463, 2003. 1.1
- [19] S Gorb, M Varenberg, A Peressadko, and J Tuma. Biomimetic mushroom-shaped fibrillar adhesive microstructure. *Journal of The Royal Society Interface*, 4(13):271–275, 2007. 1.1, 5.2

- [20] Hoon Eui Jeong, Jin-Kwan Lee, Hong Nam Kim, Sang Heup Moon, and Kahp Y. Suh. A nontransferring dry adhesive with hierarchical polymer nanohairs. *Proceedings of the National Academy of Sciences*, 106(14):5639 – 5644, 2009. 1.1, 1.3, 1.4, 3.1
- [21] John Seo, Jeffrey Eisenhaure, and Seok Kim. Micro-wedge array surface of a shape memory polymer as a reversible dry adhesive. *Extreme Mechanics Letters*, 9:207–214, 2016. 1.1
- [22] E W Hawkes, E V Eason, D L Christensen, and M R Cutkosky. Human climbing with efficiently scaled gecko-inspired dry adhesives. *Journal of The Royal Society Interface*, 12(102):20140675, 2014. 1.1, 1.4, 4.6, 4.6
- [23] Yu Tian, Noshir Pesika, Hongbo Zeng, Kenny Rosenberg, Boxin Zhao, Patricia McGuiggan, Kellar Autumn, and Jacob Israelachvili. Adhesion and friction in gecko toe attachment and detachment. *Proceedings of the National Academy of Sciences*, 103(51):19320 – 19325, 2006. 1.1
- [24] K. Autumn, A. Dittmore, D. Santos, M. Spenko, and M. Cutkosky. Frictional adhesion: a new angle on gecko attachment. *Journal of Experimental Biology*, 209(18):3569 – 3579, 2006. 1.1
- [25] Sang Yoon Yang, Andrew Carlson, Huanyu Cheng, Qingmin Yu, Numair Ahmed, Jian Wu, Seok Kim, Metin Sitti, Placid M. Ferreira, Yonggang Huang, and John A. Rogers. Elastomer surfaces with directionally dependent adhesion strength and their use in transfer printing with continuous roll-to-roll applications. *Advanced Materials*, 24(16):2117 – 2122, 2012. 1.1, 1.3, 1.4, 4.6
- [26] Seok Kim, Jian Wu, Andrew Carlson, Sung Hun Jin, Anton Kovalsky, Paul Glass, Zhuangjian Liu, Numair Ahmed, Steven L. Elgan, Weiqiu Chen, Placid M. Ferreira, Metin Sitti, Yonggang Huang, and John A. Rogers. Microstructured elastomeric surfaces with reversible adhesion and examples of their use in deterministic assembly by transfer printing. *Proceedings of the National Academy of Sciences*, 2010. 1.1, 1.3, 4.6
- [27] Matthew A Meitl, Zheng-Tao Zhu, Vipin Kumar, Keon Jae Lee, Xue Feng, Yonggang Y Huang, Ilesanmi Adesida, Ralph G Nuzzo, and John A Rogers. Transfer printing by kinetic control of adhesion to an elastomeric stamp. *Nature Materials*, 5(1):33–38, 2005. 1.1, 4.6, 5.2
- [28] Yiit Meng, Sang Yoon Yang, Seok Kim, John A. Rogers, and Metin Sitti. Gecko-inspired controllable adhesive structures applied to micromanipulation. *Advanced*

- Functional Materials*, 22(6):1246 – 1254, 2012. 1.1, 1.3, 3.1, 3.2.2, 3.4.1, 3.7, 4.6, 5.1
- [29] Sukho Song and Metin Sitti. Soft Grippers Using Micro-fibrillar Adhesives for Transfer Printing. *Advanced Materials*, 26(28):4901–4906, 2014. 1.1, 1.4, 1.7, 3.1, 4.6, 5.2
- [30] Michael P Murphy, Casey Kute, Yiğit Mengüç, and Metin Sitti. Waalbot II: Adhesion Recovery and Improved Performance of a Climbing Robot using Fibrillar Adhesives. *The International Journal of Robotics Research*, 30(1):118–133, 2011. 1.1, 1.4, 4.6
- [31] O Unver and M Sitti. Tankbot: A palm-size, tank-like climbing robot using soft elastomer adhesive treads. *The International Journal of Robotics Research*, 29(14):1761–1777, December 2010. 1.1, 4.6
- [32] M P Murphy and M Sitti. Waalbot: An agile small-scale wall-climbing robot utilizing dry elastomer adhesives. *IEEE/ASME Transactions on Mechatronics*, 12(3):330–338, 2007. 1.1, 4.6
- [33] Kellar Autumn, Metin Sitti, Yiching A. Liang, Anne M. Peattie, Wendy R. Hansen, Simon Sponberg, Thomas W. Kenny, Ronald Fearing, Jacob N. Israelachvili, and Robert J. Full. Evidence for van der waals adhesion in gecko setae. *Proceedings of the National Academy of Sciences*, 99(19):12252 – 12256, 2002. 1.2, 1.4
- [34] Gerrit Huber, Hubert Mantz, Ralph Spolenak, Klaus Mecke, Karin Jacobs, Stanislav N. Gorb, and Eduard Arzt. Evidence for capillarity contributions to gecko adhesion from single spatula nanomechanical measurements. *Proceedings of the National Academy of Sciences of the United States of America*, 102(45):16293 – 16296, 2005. 1.2
- [35] K. Autumn, C. Majidi, R. E. Groff, A. Dittmore, and R. Fearing. Effective elastic modulus of isolated gecko setal arrays. *Journal of Experimental Biology*, 209(18):3558 – 3568, 2006. 1.2
- [36] B. N. J. Persson. On the mechanism of adhesion in biological systems. *The Journal of Chemical Physics*, 118(16):7614 – 7621, 2003. 1.2
- [37] Nicholas J. Glassmaker, Anand Jagota, Chung-Yuen Hui, William L. Noderer, and Manoj K. Chaudhury. Biologically inspired crack trapping for enhanced adhesion. *Proceedings of the National Academy of Sciences*, 104(26):10786 – 10791, 2007. 1.2, 1.4

- [38] Anand Jagota and Stephen J. Bennison. Mechanics of adhesion through a fibrillar microstructure. *Integrative and Comparative Biology*, 42(6):1140 – 1145, 2002. 1.2
- [39] Burak Aksak, Chung-Yuen Hui, and Metin Sitti. The effect of aspect ratio on adhesion and stiffness for soft elastic fibres. *Journal of The Royal Society Interface*, 8(61):1166–1175, 2011. 1.2, 2.3, 2.4
- [40] A V Spuskanyuk, R M McMeeking, V S Deshpande, and E Arzt. The effect of shape on the adhesion of fibrillar surfaces. *Acta Biomaterialia*, 4(6):1669–1676, 2008. 1.2, 4.5.4, 5.2
- [41] Huajian Gao and Haimin Yao. Shape insensitive optimal adhesion of nanoscale fibrillar structures. *Proceedings of the National Academy of Sciences*, 101(21):7851–7856, 2004. 1.2, 1.4, 5.1
- [42] Aránzazu del Campo, Christian Greiner, and Eduard Arzt. Contact Shape Controls Adhesion of Bioinspired Fibrillar Surfaces. *Langmuir*, 23(20):10235–10243, 2007. 1.2, 4.5.4
- [43] Burak Aksak, Korhan Sahin, and Metin Sitti. The optimal shape of elastomer mushroom-like fibers for high and robust adhesion. *Beilstein Journal of Nanotechnology*, 5:630–638, 2014. 1.2, 2.3, 2.3, 2.4, 4.5.4, 5.1, 5.2
- [44] Robert F. Shepherd, Filip Ilievski, Wonjae Choi, Stephen A. Morin, Adam A. Stokes, Aaron D. Mazzeo, Xin Chen, Michael Wang, and George M. Whitesides. Multigait soft robot. *Proceedings of the National Academy of Sciences*, 108(51):20400–20403, 2011. 1.3, 4.1
- [45] Sehyuk Yim and M. Sitti. Design and rolling locomotion of a magnetically actuated soft capsule endoscope. *Robotics, IEEE Transactions on*, 28(1):183 – 194, 2012. 1.3
- [46] Dae-Hyeong Kim, Nanshu Lu, Roozbeh Ghaffari, Yun-Soung Kim, Stephen P. Lee, Lizhi Xu, Jian Wu, Rak-Hwan Kim, Jizhou Song, Zhuangjian Liu, Jonathan Viveri, Bassel de Graff, Brian Elolampi, Moussa Mansour, Marvin J. Slepian, Sukwon Hwang, Joshua D. Moss, Sang-Min Won, Younggang Huang, Brian Litt, and John A. Rogers. Materials for multifunctional balloon catheters with capabilities in cardiac electrophysiological mapping and ablation therapy. *Nat Mater*, 10(4):316 – 323, 2011. 1.3
- [47] Sangok Seok, C.D. Onal, Kyu jin Cho, R.J. Wood, D. Rus, and Sangbae Kim. Meshworm: A peristaltic soft robot with antagonistic nickel titanium coil actuators. *Mechatronics, IEEE/ASME Transactions on*, 18(5):1485 – 1497, 2013. 1.3

- [48] E. Steltz, A Mozeika, N. Rodenberg, E. Brown, and H.M. Jaeger. Jsel: Jamming skin enabled locomotion. In *Intelligent Robots and Systems, 2009. IROS 2009. IEEE/RSJ International Conference on*, pages 5672 – 5677, 2009. 1.3
- [49] Huai-Ti Lin, Gary G Leisk, and Barry Trimmer. Goqbot: a caterpillar-inspired soft-bodied rolling robot. *Bioinspiration and Biomimetics*, 6(2):026007(1) – 026007(14), 2011. 1.3
- [50] Cecilia Laschi, Matteo Cianchetti, Barbara Mazzolai, Laura Margheri, Maurizio Follador, and Paolo Dario. Soft robot arm inspired by the octopus. *Advanced Robotics*, 26(7):709 – 727, 2012. 1.3
- [51] Sangbae Kim, M. Spenko, S. Trujillo, B. Heyneman, D. Santos, and M.R. Cutkosky. Smooth vertical surface climbing with directional adhesion. *Robotics, IEEE Transactions on*, 24(1):65 – 74, 2008. 1.3, 1.3, 1.4
- [52] Sangbae Kim, Cecilia Laschi, and Barry Trimmer. Soft robotics: a bioinspired evolution in robotics. *Trends in Biotechnology*, 31(5):287 – 294, 2013. 1.3
- [53] Filip Ilievski, Aaron D. Mazzeo, Robert F. Shepherd, Xin Chen, and George M. Whitesides. Soft robotics for chemists. *Angewandte Chemie International Edition*, 50(8):1890 – 1895, 2011. 1.3, 3.6
- [54] Eric Brown, Nicholas Rodenberg, John Amend, Annan Mozeika, Erik Steltz, Mitchell R. Zakin, Hod Lipson, and Heinrich M. Jaeger. Universal robotic gripper based on the jamming of granular material. *Proceedings of the National Academy of Sciences*, 107(44):18809 – 18814, 2010. 1.3, 1.3, 3.6, 5.2
- [55] J.R. Amend, E.M. Brown, N. Rodenberg, H.M. Jaeger, and H. Lipson. A positive pressure universal gripper based on the jamming of granular material. *Robotics, IEEE Transactions on*, 28(2):341 – 350, 2012. 1.3, 1.3
- [56] N.G. Cheng, M.B. Lobovsky, S.J. Keating, AM. Setapen, K.I Gero, AE. Hosoi, and K.D. Iagnemma. Design and analysis of a robust, low-cost, highly articulated manipulator enabled by jamming of granular media. In *Robotics and Automation (ICRA), 2012 IEEE International Conference on*, pages 4328 – 4333, 2012. 1.3
- [57] A. Pettersson, S. Davis, J.O. Gray, T.J. Dodd, and T. Ohlsson. Design of a magnetorheological robot gripper for handling of delicate food products with varying shapes. *Journal of Food Engineering*, 98(3):332 – 338, 2010. 1.3, 3.6
- [58] Yong-Jae Kim, Shanbao Cheng, Sangbae Kim, and K. Iagnemma. A stiffness-adjustable hyperredundant manipulator using a variable neutral-line mechanism for

- minimally invasive surgery. *Robotics, IEEE Transactions on*, 30(2):382 – 395, 2014. 1.3
- [59] T. Takahashi, K. Nagato, M. Suzuki, and S. Aoyagi. Flexible vacuum gripper with autonomous switchable valves. In *Robotics and Automation (ICRA), 2013 IEEE International Conference on*, pages 364 – 369, 2013. 1.3
- [60] Andrew G. Gillies, Jonghun Kwak, and Ronald S. Fearing. Controllable particle adhesion with a magnetically actuated synthetic gecko adhesive. *Advanced Functional Materials*, 23(26):3256 – 3261, 2013. 1.3, 3.4.1, 3.7, 5.1
- [61] Won-Gyu Bae, Doogon Kim, and Kahp-Yang Suh. Instantly switchable adhesion of bridged fibrillar adhesive via gecko-inspired detachment mechanism and its application to a transportation system. *Nanoscale*, 5(23):11876 – 11884, 2013. 1.3, 3.1, 3.4.1, 3.7, 5.1
- [62] Ming Zhou, Yu Tian, Dan Sameoto, Xiangjun Zhang, Yonggang Meng, and Shizhu Wen. Controllable interfacial adhesion applied to transfer light and fragile objects by using gecko inspired mushroom-shaped pillar surface. *ACS Applied Materials and Interfaces*, 5(20):10137 – 10144, 2013. 1.3, 1.4
- [63] Rong Long, Chung-Yuen Hui, Seok Kim, and Metin Sitti. Modeling the soft backing layer thickness effect on adhesion of elastic microfiber arrays. *Journal of Applied Physics*, 104(4):044301–1 – 044301–9, 2008. 1.3, 3.1, 4.6
- [64] Yu Tian, Jin Wan, Noshir Pesika, and Ming Zhou. Bridging nanocontacts to macroscale gecko adhesion by sliding soft lamellar skin supported setal array. *Sci. Rep.*, 3:1382–1 – 1382–6, 2013. 1.3, 3.1
- [65] Jongho Lee, Brian Bush, Roya Maboudian, and Ronald S. Fearing. Gecko-inspired combined lamellar and nanofibrillar array for adhesion on nonplanar surface. *Langmuir*, 25(21):12449 – 12453, 2009. 1.3, 4.5.4
- [66] Yang Zhao, Yang Zhao, Tao Tong, Tao Tong, Lance Delzeit, Lance Delzeit, Ali Kashani, Ali Kashani, M Meyyappan, M Meyyappan, Arun Majumdar, and Arun Majumdar. Interfacial energy and strength of multiwalled-carbon-nanotube-based dry adhesive. *Journal of Vacuum Science & Technology B*, 24(1):331–335, 2006. 1.4
- [67] Kellar Autumn, Yiching A. Liang, S. Tonia Hsieh, Wolfgang Zesch, Wai Pang Chan, Thomas W. Kenny, Ronald Fearing, and Robert J. Full. Adhesive force of a single gecko foot-hair. *Nature*, 405(6787):681 – 685, 2000. 1.4

- [68] Hoon Eui Jeong, Moon Kyu Kwak, and Kahp Y Suh. Stretchable, Adhesion-Tunable Dry Adhesive by Surface Wrinkling. *Langmuir*, 26(4):2223–2226, 2010. 1.4
- [69] Burak Aksak, M.P. Murphy, and M. Sitti. Gecko inspired micro-fibrillar adhesives for wall climbing robots on micro/nanoscale rough surfaces. In *Robotics and Automation, 2008. ICRA 2008. IEEE International Conference on*, pages 3058 – 3063, 2008. 1.4, 3.3.1
- [70] Matthew A Estrada, Elliot W Hawkes, David L Christensen, and Mark R Cutkosky. Perching and vertical climbing: Design of a multimodal robot. *2014 IEEE International Conference on Robotics and Automation (ICRA)*, pages 4215–4221, 2014. 1.4
- [71] Elliot W Hawkes, David L Christensen, Amy Kyungwon Han, Hao Jiang, and Mark R Cutkosky. Grasping without squeezing: Shear adhesion gripper with fibrillar thin film. *2015 IEEE International Conference on Robotics and Automation (ICRA)*, pages 2305–2312, 2015. 1.4
- [72] Michael D Bartlett, Andrew B Croll, Daniel R King, Beth M Paret, Duncan J Irschick, and Alfred J Crosby. Looking Beyond Fibrillar Features to Scale Gecko-Like Adhesion. *Advanced Materials*, 24(8):1078–1083, 2012. 1.4, 4.6
- [73] Z Ye, G Z Lum, S Song, S Rich, and M Sitti. Phase Change of Gallium Enables Highly Reversible and Switchable Adhesion. *Advanced Materials*, 28(25):5087–5092, 2016. 1.4, 4.5.4
- [74] J Krahn, D Sameoto, and C Menon. Controllable biomimetic adhesion using embedded phase change material. *Smart Materials and Structures*, 20(1):015014, 2010. 1.4, 4.5.4
- [75] Wanliang Shan, Stuart Diller, Abbas Tutcuoglu, and Carmel Majidi. Rigidity-tuning conductive elastomer. *Smart Materials and Structures*, 24(6):065001, 2015. 1.4
- [76] Lindsey Hines, Metin Sitti, Veaceslav Arabagi, Lindsey Hines, Veaceslav Arabagi, and Metin Sitti. Shape Memory Polymer-Based Flexure Stiffness Control in a Miniature Flapping-Wing Robot. *IEEE Transactions on Robotics*, 28(4):987–990, 2012. 1.4
- [77] Wanliang Shan, Tong Lu, and Carmel Majidi. Soft-matter composites with electrically tunable elastic rigidity. *Smart Materials and Structures*, 22(8):085005, 2013. 1.4
- [78] K Kendall. An Adhesion Paradox. *The Journal of Adhesion*, 5(1):77–79, 1973. 1.4

- [79] Sukho Song, Carmel Majidi, and Metin Sitti. GeckoGripper: A soft, inflatable robotic gripper using gecko-inspired elastomer micro-fiber adhesives. *2014 IEEE/RSJ International Conference on Intelligent Robots and Systems (IROS)*, pages 4624–4629, 2014. 1.7, 3.1, 4.4.2
- [80] Sukho Song, Dirk-Michael Drotlef, Carmel Majidi, and Metin Sitti. Controllable Load Sharing for Soft Adhesive Interfaces on Three-Dimensional Surfaces (accepted). *Proceedings of the National Academy of Sciences*, 114(22):E4344–E4353, 2017. 1.7, 4.1
- [81] H Marvi, Y Han, and M Sitti. Actively controlled fibrillar friction surfaces. *Applied Physics Letters*, 106(5):051602, 2015. 2.2, 2.2
- [82] D Maugis. *Contact, Adhesion and Rupture of Elastic Solids*, volume 130. Springer-Verlag Berlin Heidelberg, 2000. 2.3, 2.3
- [83] Tian Tang, Chung-Yuen Hui, and Nicholas J Glassmaker. Can a fibrillar interface be stronger and tougher than a non-fibrillar one? *Journal of The Royal Society Interface*, 2(5):505–516, 2005. 2.3
- [84] Noshir S. Pesika, Yu Tian, Boxin Zhao, Kenny Rosenberg, Hongbo Zeng, Patricia McGuiggan, Kellar Autumn, and Jacob N. Israelchvili. Peel-zone model of tape peeling based on the gecko adhesive system. *The Journal of Adhesion*, 83(4):383 – 401, 2007. 3.4.1
- [85] Uyiosa Abusomwan and Metin Sitti. Effect of retraction speed on adhesion of elastomer fibrillar structures. *Applied Physics Letters*, 101(21):211907, 2012. 3.4.1, 5.2
- [86] Shilpi Vajpayee, Rong Long, Lulin Shen, Anand Jagota, and Chung-Yuen Hui. Effect of rate on adhesion and static friction of a film-terminated fibrillar interface. *Langmuir*, 25(5):2765 – 2771, 2009. 3.4.1
- [87] Anny L. Flory, David A. Brass, and Kenneth R. Shull. Deformation and adhesive contact of elastomeric membranes. *Journal of Polymer Science Part B: Polymer Physics*, 45(24):3361 – 3374, 2007. 3.4.1
- [88] Lindsey Hines, Kirstin Petersen, Guo Zhan Lum, and Metin Sitti. Soft Actuators for Small-Scale Robotics. *Advanced Materials*, page 1603483, December 2016. 4.1
- [89] Seok Kim, Seok Kim, Eugene Cheung, Eugene Cheung, Metin Sitti, and Metin Sitti. Wet Self-Cleaning of Biologically Inspired Elastomer Mushroom Shaped Microfibrillar Adhesives. *Langmuir*, 25(13):7196–7199, 2009. 4.2, 5.2

- [90] Yiğit Mengüç, Michael Röhrig, Uyiosa Abusomwan, Hendrik Hölscher, and Metin Sitti. Staying sticky: contact self-cleaning of gecko-inspired adhesives. *Journal of The Royal Society Interface*, 11(94):20131205, 2014. 4.2, 5.2
- [91] Dirk-Michael Drotlef, Lukas Stepien, Michael Kappl, W Jon P Barnes, Hans-Jürgen Butt, and Aránzazu del Campo. Insights into the Adhesive Mechanisms of Tree Frogs using Artificial Mimics. *Advanced Functional Materials*, 23(9):1137–1146., 2012. 4.3.1
- [92] Dirk-Michael Drotlef, Peter Blümmler, Periklis Papadopoulos, and Aránzazu del Campo. Magnetically Actuated Micropatterns for Switchable Wettability. *ACS Applied Materials & Interfaces*, 6(11):8702–8707, 2014. 4.3.1
- [93] Martin H Sadd. *Elasticity: Theory, Applications, and Numerics*. Academic Press, 2014. 4.4.1
- [94] I D Johnston, D K McCluskey, C K L Tan, and M C Tracey. Mechanical characterization of bulk Sylgard 184 for microfluidics and microengineering. *Journal of Micromechanics and Microengineering*, 24(3):035017, 2014. 4.4.1
- [95] Carmel Majidi, Richard E. Groff, and Ron S. Fearing. Analysis of shaft-loaded membrane delamination using stationary principles. *Mathematics and Mechanics of Solids*, 13(1):3–22, 2008. 4.4.2
- [96] K T Wan. Adherence of an Axisymmetric Flat Punch Onto a Clamped Circular Plate: Transition From a Rigid Plate to a Flexible Membrane. *Journal of Applied Mechanics*, 69(2):110–116, October 2001. 4.4.2
- [97] J B Haddow, L Favre, and R W Ogden. Application of variational principles to the axial extension of a circular cylindrical nonlinearly elastic membrane. *Journal of engineering mathematics*, 37(1):65–84, 2000. 4.4.2
- [98] K Kendall. Thin-film peeling-the elastic term. *Journal of Physics D: Applied Physics*, 8(13):1449, 1975. 4.4.2
- [99] Hohan Lee, Doo-Seung Um, Youngsu Lee, Seongdong Lim, Hyung-jun Kim, and Hyunhyub Ko. Octopus-Inspired Smart Adhesive Pads for Transfer Printing of Semiconducting Nanomembranes. *Advanced Materials*, 28(34):7457–7465, 2016. 4.4.2
- [100] Jun Shintake, Samuel Rosset, Bryan Schubert, Dario Floreano, and Herbert Shea. Versatile Soft Grippers with Intrinsic Electroadhesion Based on Multifunctional Polymer Actuators. *Advanced Materials*, 28(2):231–238, 2015. 4.4.2

- [101] Benjamin C Mac Murray, Xintong An, Sanlin S Robinson, Ilse M van Meerbeek, Kevin W O'Brien, Huichan Zhao, and Robert F Shepherd. Poroelastic Foams for Simple Fabrication of Complex Soft Robots. *Advanced Materials*, 27(41):6334–6340, 2015. 4.4.2
- [102] K L Johnson, K Kendall, and A D Roberts. Surface Energy and the Contact of Elastic Solids. *Proceedings of the Royal Society A: Mathematical, Physical and Engineering Sciences*, 324(1558):301–313, 1971. 4.5.3
- [103] Lars Heepe and Stanislav N Gorb. Biologically Inspired Mushroom-Shaped Adhesive Microstructures. *Annual Review of Materials Research*, 44(1):173–203, 2014. 4.5.4
- [104] Kellar Autumn. *Biological Adhesives*, chapter Properties, Principles, and Parameters of the Gecko Adhesive System in Biological Adhesives, pages 225–256. Springer Berlin Heidelberg, 2006. 4.6
- [105] D Labonte and W Federle. Scaling and biomechanics of surface attachment in climbing animals. *Philosophical Transactions of the Royal Society B: Biological Sciences*, 370(1661):20140027, 2014. 4.6
- [106] Giuseppe Carbone, Elena Pierro, and Stanislav N Gorb. Origin of the superior adhesive performance of mushroom-shaped microstructured surfaces. *Soft Matter*, 7:5545–5552, 2011. 5.2
- [107] G Carbone and E Pierro. Sticky Bioinspired Micropillars: Finding the Best Shape. *Small*, pages 1449–1454, 2012. 5.2
- [108] Quan Xu, Yiyang Wan, Travis Shihao Hu, Tony X Liu, Dashuai Tao, Peter H Niewiarowski, Yu Tian, Yue Liu, Liming Dai, Yanqing Yang, and Zhenhai Xia. Robust self-cleaning and micromanipulation capabilities of gecko spatulae and their bio-mimics. *Nature Communications*, 6:8949, 2015. 5.2